TU

TECHNISCHE UNIVERSITÄT WIEN

DISSERTATION

INVESTIGATIONS OF BEARING FAILURES DUE TO ELECTRIC CURRENT PASSAGE

ausgeführt zum Zwecke der Erlangung des akademischen Grades

eines Doktors der technischen Wissenschaften

unter der Leitung von

ao. Univ.Prof. DI Dr. Martin GRÖSCHL

und

Univ. Lektor i. R. DI Dr. Frank BUSCHBECK

E134

Institut für Allgemeine Physik

eingereicht an der Technischen Universität Wien

Fakultät für Physik

von

DI Andreas JAGENBREIN

E8926101

Unt. Hauptstr. 2

A-2443 Leithaprodersdorf

Burgenland

Wien, am 08.09.2005   _____

Zusammenfassung

Seit Frequenzumrichter für die Steuerung von Drehsrommotoren verwendet werden, kommen es vermehrt zu Lagerschäden, die als Folge von Stromdurchgang durch die Lager entstehen. Parasitäre Ströme, vor allen jene, die in frequenzumrichter-betriebenen Motoren und Maschinen auftreten, und ihre Ursachen wurden anhand jüngster Literatur und eigener Forschungsergebnisse gegenübergestellt, da diese in der Literatur oft nicht klar genug unterschieden wurden.

Um das elektrische System eines frequenzumrichter-betriebenen Drehsrommotors untersuchen zu können, wurden Messmethoden entwickelt und Messvorrichtungen aufgebaut. Das System konnte mit Hilfe der erhaltenen Messergebnisse analysiert und in der Folge eine statische Testapparatur geplant und errichtet werden.

Diese Testapparatur ermöglichte es, so genannte „electric discharge machining" (EDM)-Prozesse mit festgelegter Energie und an einer bestimmten Stelle zwischen zwei Testkörpern (Standardlagerkugeln und -zylinderrollen) auszulösen, ähnlich den EDM-Prozessen, die in frequenzumrichter-betriebenen Motoren auftreten. Der Zwischenraum zwischen den Testkörpern wurde mit verschiedenen Ölen bzw. mit Luft gefüllt, um den Einfluss dieser Materialen auf die verursachten Schäden auf den Oberflächen der Testkörper zu untersuchen.

Chemische und physikalische Eigenschaften der verwendeten Öle, wie deren Dichte, kinematische Viskosität und relative Dielektrizitätszahl, wurden zu Untersuchung des Einflusses auf die mit der statischen Testapparatur erzeugten Schädigungen an den Testkörpern gemessen. Diese Schädigungen auf den Oberflächen der Testkörper wurden mit einem kontaktlosen optischen Profilometer analysiert. Weiters wurde untersucht, ob sich Veränderungen in den Ölen, die in der statischen Testapparatur Serien von EDM-Prozessen ausgesetzt waren, auch in den Infrarot-Transmissions-spektren zeigen.

Mit Hilfe einer digitalen schwarz-weiß Hochgeschwindigkeitskamera wurden in der statischen Testapparatur ausgelöste EDM-Prozesse zur Dokumentation gefilmt.

Im Rahmen dieser Arbeit wurde ein Prototyp einer Schaltungsanordnung basierend auf einer neuartigen Methode (EP 1 445 850 A1) zur Kompensation der Spannung an der Motorwelle frequenzumrichter-betriebener Motoren entworfen und aufgebaut. Nach Erweiterung und Optimierung dieses Aufbaus konnte dessen verbesserte Wirkung durch

Messungen nachgewiesen werden. Während dieser Arbeit wurde auch das Konzept eines erdsymmetrischen frequenzumrichter-gesteuerten Antriebs entwickelt, der keine Spannung an der Motorwelle verursacht.

Schließlich wurden Vorschläge zum Analyse und Optimierung elektrischer Systeme von frequenzumrichter-gesteuerten Antrieben auf der Grundlage von Erkenntnissen aus der Literatur und eigener wissenschaftlicher Arbeit zusammengefasst.

Abstract

Bearing damages due to electrical current passage through bearings have increased since frequency converters have been used for the control of three-phase induction motors. In this work, an overview is given of parasitic currents and their sources, especially those generated in frequency converter driven motors and machines, according to recent literature and own research work, because they have not been distinguished clearly in the past.

Within this thesis, measuring methods have been developed and measuring set-ups were constructed for the investigation of the electrical regime of a three-phase induction motor driven by a frequency converter. Based on the obtained results, such a drive system could be analysed and, hence, a static test rig was designed and constructed.

This test rig allowed to initiate electric discharge machining (EDM)-processes of defined energies at finite regions between two test specimens (standard bearing balls and cylindrical rolling elements), thereby simulating real EDM-processes that occur in the bearings of a frequency converter driven motor. The gap between the test specimens was filled either with different oil samples or with air, to investigate the influence of these materials on the damages generated at the surfaces of the test specimens.

Chemical and physical properties, such as the mass density, the kinematic viscosity and the relative permittivity, of the investigated oils were measured, to study their influences on the damages generated at the test specimens in the static test rig. These enforced damages at the surfaces of the test specimens were analysed with a contactless optical profile meter. Further, the sensitivity of infrared transmission spectra on the deterioration of oils, subjected to series of EDM-processes in the static test rig, was studied.

Photographs of EDM-processes initiated in the static test rig were made with a monochrome high speed digital camera for documentation.

In this work, the prototype of circuit arrangement based on a novel method (EP 1 445 850 A1) for the compensation of the voltage at the motor shaft of frequency converter driven motors was designed and constructed. Further, this set-up was upgraded and improved, and its increased effectiveness could be verified by further measurements. Additionally, the concept of an earth balanced power supply for

frequency converter driven motors was developed in the present work, which does not cause the generation of a voltage at the motor shaft.

Finally, recommendations for the analysis and optimisation of the electrical regime of frequency converter driven systems were summarized based on literature and own research work.

Contents

1   Introduction

Precise control of the rotational speed of machines and consequently of the coupled electrical drives has always been required for dedicated industrial applications. Over the past decades, the demand for the control of the rotational speed has been grown. Many industrial applications need for correct operation a constant rotational speed, whereas other driving systems must be able to adjust the rotational speed according to actual requirements or given procedures. To be able to control the rotational speed of electrical drives, several sophisticated systems have been developed. During the last few decades, various types of frequency converters have been designed for different types of induction motors. Many types of frequency converters are designed to control the rotational speed of three-phase induction motors, which are often used in industrial applications.

Bearing damages due to electric current passage through rolling bearings are known for a long time, but they have led to an increase of bearing failures since frequency converters have been used for the control of the rotational speed of induction motors. Electric current passage through rolling bearings happens in the contact areas between the rolling elements (e.g., bearing balls or cylindrical rolling elements) and the inner rings and outer rings, respectively, where it may damage the surfaces of the metallic components of the bearings as well as the lubricants.

Not only bearings in induction motors but also bearings in driven machines may be damaged by electric current passage. To avoid machinery breakdown due to bearing failure, several counter measures against electric current passage through bearings have been developed, primary by operators using frequency converter controlled drives, and in the meantime also by producers of motors and frequency converters. But most of these counter measures often allow to suppress, avoid or interrupt only a part of the existing processes, which may cause electric current passage through bearings.

Bearing damages caused by circulating currents, which may occur nearly in all electric motors, and by electrostatic discharges have been investigated for a long time. Depending on the electrical set-up of a system comprising a frequency converter and a driven induction motor, additional effects, such as high-frequency *dv/dt*-currents, currents in the protective earth (PE) wire and electric discharge machining (EDM) may also be responsible for bearing damages. Although the study of these phenomena is of great interest, they have not always been distinguished clearly in the literature.

One aim within the scope of this thesis was to give a clear description of the different phenomena, which may cause electric current passage through bearings and hence bearing damage. Further, the electrical regime of a test motor driven by a frequency converter was investigated for the characterisation of such a drive system. Therefore, special measuring methods were developed in this work. By means of the obtained results a test rig for static tests (static test rig) was designed, to study the influence of different base oils on EDM-processes. In the static test rig, series of EDM-processes with defined energies were initiated at finite regions on the surfaces of standard bearing elements using different base oils. The damages generated at the test specimens and the deterioration of the oils due to the initiated EDM-processes were investigated. Additionally, a prototype set-up for the compensation of the motor shaft-to-frame voltage in an induction motor driven by a frequency converter could be designed and constructed. Furthermore, a new electrical control system for induction motors driven by frequency converters was proposed, which avoids EDM-currents, high-frequency *dv/dt*-currents and currents in the PE-wire.

2   State of the art

2.1   Basic operating principles of frequency converters

P. F. Brosch [1] noted that, nowadays, frequency converters are used in many industrial areas, such as food production, plant construction, paper industry, plastics industry, power industry, metal industry, and so on, because they have many beneficial features, e.g., suitable energy supply, little installation and wiring effort, easy manipulation, high efficiency, controllability of rotational speed and drive torque, wide range of rotational speed, availability of zero rotational speed, low noise and vibration, and energy regeneration at breaking operation. In this book the author describes the basic principles of several types of frequency converters in the power range of up to 100 kW. The most common types are voltage source DC-link converters, current source DC-link converters, matrix converters, electronic AC power controllers, three-phase AC power controllers, and chopper converters. Frequency converters are used to control the rotational speed of DC, AC or three-phase induction motors. Depending on the working frequency and the power range, different thyristors (Gate-Turn-Off (GTO), Insulated Gate Controlled (IGC) or reverse conducting) or, nowadays, mainly transistors (bipolar, unipolar or Insulated Gate Bipolar Transistors (IGBT)) are used as electronic power switches in frequency converters comprising a computerised converter circuit for rotational speed control [1].

Representatively, a voltage source DC-link frequency converter is described here, which controls the rotational speed of a three-phase induction motor by pulse width modulation (PWM) [1-4]. An equivalent electric circuit of such a drive is shown in Fig. 2-1. The frequency converter is fed by a three-phase power supply. A DC voltage balanced to ground, but also a remaining ripple voltage with a frequency of 150 Hz, is generated by a three-phase diode rectifier and two smoothing capacitors, each connected via the mid-point M to ground G. The two voltage rails supply referred to ground a positive $V_{(+)}$ and a negative $V_{(-)} = -V_{(+)}$ voltage, respectively. By means of a transistorised converter, including IGBTs as electronic power switches, either the positive or the negative voltage is switched to the three frequency converter output phases U_1, U_2 and U_3. That means each phase voltage between one frequency converter output phase U_1, U_2 and U_3, respectively, and ground is independently switched over positive and negative voltage levels according to a computerised control procedure using PWM in that case. The wye-connected three-phase induction motor, comprising a star point Y, is controlled by means of these three-phase voltages, which are transferred through a power cable to the motor terminals and hence to one end of the corresponding

stator windings (W_1, W_2 and W_3). The other ends of the stator windings are interconnected to the motor star point Y. The common symptom of all frequency converters are the switched phase voltages supplied to the driven motors.
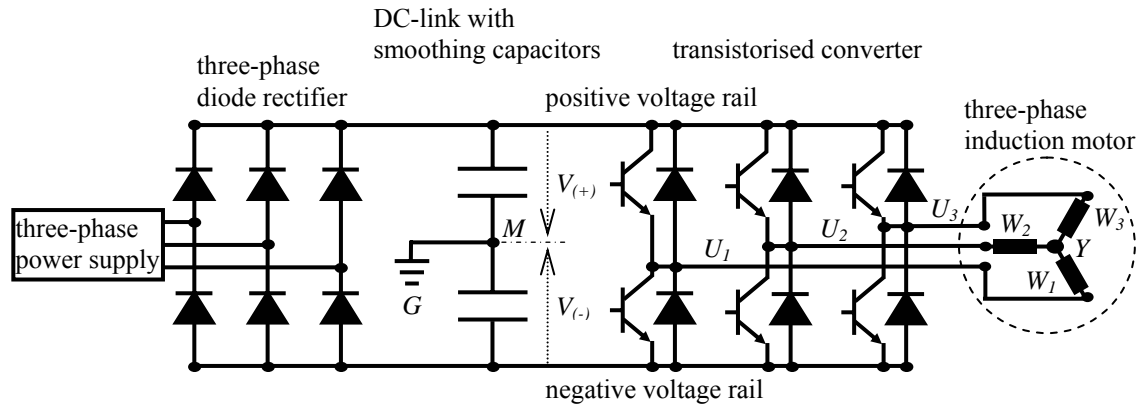
Fig. 2-1:   Schematic diagram of a voltage source DC-link frequency converter. $V_{(+)}$ and $V_{(-)}$, respectively, are the voltages at the positive and the negative voltage rail referred to ground G. The mid-point of the DC-link is labelled M. U_1, U_2 and U_3 are the frequency converter output phases, which are transferred to the corresponding stator windings W_1, W_2 and W_3 of the three-phase induction motor.

2.2   Bearing damages due to electrical current passage

Bearing damages due to electrical current passage are known since a few decades. So O. Schenk [5] distinguished three cases of current passage through bearings: desired current passage of the working current, e.g., in bearings of electric engines, and not intended current passage due to circulating currents because of asymmetries in the electromagnetic field of a motor or due to fault currents because of damages of insulation. Today engines are mostly equipped with separate sliding contacts for the working current to protect their bearings against damages. Typical damages caused by current passage at the raceways of inner rings, outer rings or rolling elements are electric pitting and, hence, the so-called fluting or washboard pattern can be formed. Craters with a size from 0.1 mm to 0.5 mm in diameter are typically generated by electrical pitting occurring in applications with high-power and high DC voltage [2] (Fig. 2-2).

By means of experiments A. Kohaut [6] could prove, that washboard patterns can be generated by DC or AC currents. From practical operations and experiments O. Schenk [5] found out that the appearance of washboard patterns at the raceways of bearings depends not only on the current density but also on the duration, during which current passages happened (Tab. 2-1). G. Preisinger [2] and A. Mütze [7] summarised different limits of current densities from literature. Bearing life in DC and

low-frequency AC applications should not be influenced by a current density smaller than 0.1 A_{pk}/mm^2, whereas bearing life may significantly be decreased by current densities greater than 0.7 A_{pk}/mm^2.
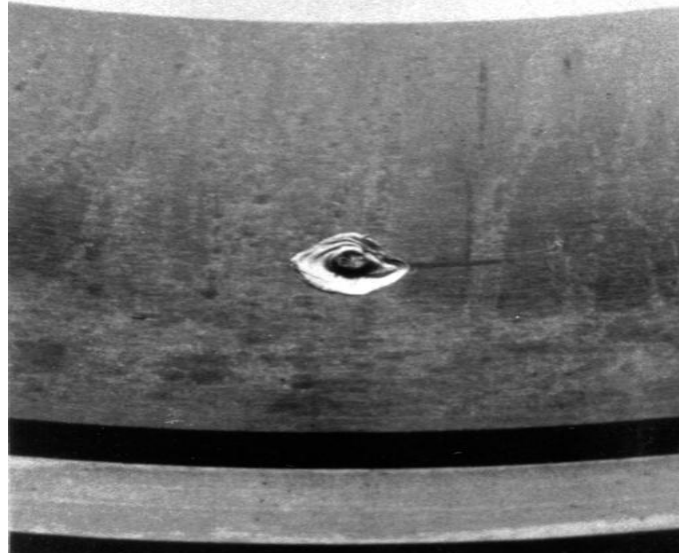
Fig. 2-2:   Typical crater generated by electrical pitting [2].

current density [A/mm^2]	2	1.8	1.7	1.4
duration [h]	5	25	50	500

Tab. 2-1:   Appearance of washboard pattern at the raceways of bearings depending on current density and duration of current passage [5].

The mechanisms leading to low-frequency circulating currents in mains operated induction motors were described by R. F. Schiferl et al. [8] and D. Macdonald et al. [9]. Mains operated induction motors are supplied by low-frequency sine waves, therefore the circulating currents in such motors are low-frequency currents. In each induction motor the magnetic field contains small and inherent asymmetries, which are caused by eccentricity of the rotor, slots and cooling holes in the stator and the rotor, laminations, shaft keyways, directional properties of magnetic materials, unbalances in the power supply or transient conditions. These asymmetries generate magnetic flux variations and hence a resulting potential difference along the motor shaft. Whenever electrically possible, an equalising current (here a low-frequency circulating current) is initiated. Due to circulating currents small craters are generated at the surfaces of the raceways of rolling elements, inner rings and outer rings. When rolling elements roll over these craters, vibrations of the rolling elements are produced, which increase surface damage as well as current passage and hence the generation of craters at the surface of raceways and deterioration of lubricants. Finally, a washboard pattern is formed. A typical

washboard pattern on the raceway of the inner ring from a rolling bearing is shown in Fig. 2-3 [8].
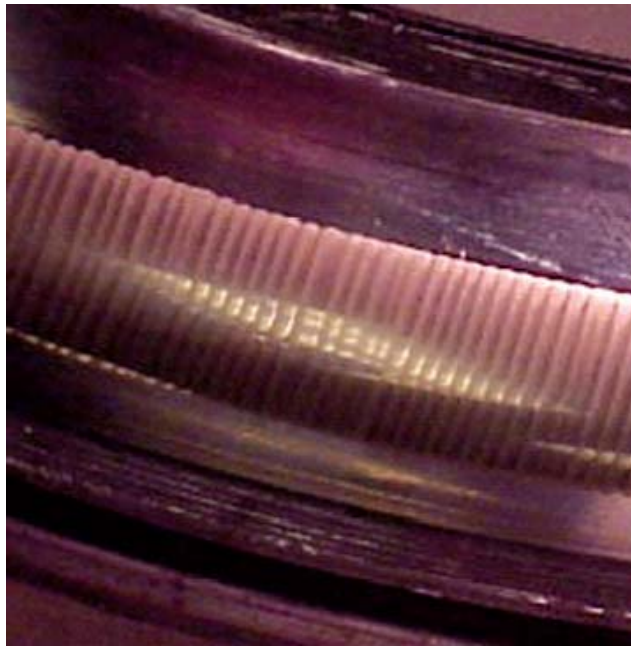
Fig. 2-3:   Washboard pattern at the surface of a raceway caused by electric current passage [8].

Using a procedure according to the IEEE Standard No. 112 [10] the shaft end-to-end voltage (V_{SE}) at motors in operation can be measured, if at least one bearing is electrically insulated or if in all bearings the lubricant films have insulating properties. Therefore the shaft must electrically be connected to the frame, e.g. with a brush, in a section near one bearing. Subsequently a high-impedance voltmeter or an oscilloscope connected in a section near the other bearing between the motor shaft and the motor frame can be used to measure the shaft end-to-end voltage. Alternatively, the voltmeter or the oscilloscope can be connected between both ends of the motor shaft. Under the same conditions also the shaft end-to-end *current* flowing through the motor shaft can be measured by forming an electrical circuit with a low-impedance amperemeter in the same ways as described above.

Electric current passage through bearings can also be caused by electrostatic discharges in bearings [2, 11]. A potential difference between the motor shaft and the motor frame (motor shaft-to-frame voltage V_{MSF}) can be produced in ionized air, at applications with belt-driven rotors or at fans, where a propeller is directly mounted at the motor shaft, if the motor shaft is not electrically connected to ground. Different charges at the inner rings and the outer rings of bearings due to the potential difference between them may lead to discharges and hence to discharge currents. Thereby, in general, lower energies are transferred to finite regions in the lubricants and at the surfaces of the raceways by

electrostatic discharging in contrast to circulating currents due to asymmetries in the magnetic flux.

2.3   Influence of frequency converters on bearing damages

The possibility of bearing damages in frequency converter driven induction motors is increased due to additional parasitic currents, such as high-frequency circulating currents, high-frequency dv/dt-currents, EDM-currents and currents in the PE-system [2-4, 7-9, 11-17]. By means of modern switching devices, e.g. IGBTs, in frequency converters, on the one side, switching frequencies approach the range of several kilohertz and, on the other side, voltage rise times as short as several kV/µs can be realised. These features improve the controllability of motors, e.g., of the drive torque and the rotational speed, and they reduce the energy losses occurring during the switching operations. But unfortunately the high slew rates in the phase voltages of frequency converters are responsible for many harmonics, especially at square wave like voltage shapes. The relevance of capacitive coupling between the motor frame, the rotor and the stator windings in induction motors increases with rising frequencies. That means, due to this capacitive coupling additional paths for high-frequency currents originate in the motor. This capacitive coupling is irregularly distributed along the stator windings, the rotor and the motor frame. Further, between the motor star point and the frame of a frequency converter driven motor a residual voltage, the star point-to-frame voltage (V_{YF}), is present, because the sum of the phase voltages (V_1, V_2 and V_3) of a frequency converter is not zero, in contrast to mains operated induction motors, where under normal operating conditions the sum of the three supply voltages vanishes. The star point-to-frame voltage changes with the switching frequency of the frequency converter, because during each switching operation at least one phase voltage is switched over. Further, at the star point-to-frame voltage a frequency component (150 Hz), which is three times the supply frequency, can be identified. This ripple voltage (referred to ground) originates from the three-phase rectifier that is part of the frequency converter. In the full-film lubrication regime, the motor shaft-to-frame voltage (V_{MSF}) is generated between the shaft and the frame of a frequency converter driven induction motor by the star point-to-frame voltage and the stray capacitances C_{SR}, between the stator windings and the rotor, C_{RF}, between the rotor and the frame, and C_{B1} and C_{B2}, the bearing capacitances between the inner ring and the outer ring of the bearings, due to the lubricant within the rolling contacts. The motor shaft-to-frame voltage exists also across the lubricant film in the bearings, as the bearings are electrically connected to the motor frame as well as to the motor shaft. The bearing

voltage ratio (BVR), the ratio between the motor shaft-to-frame voltage (V_{MSF}) and the star point-to-frame voltage (V_{YF}) can be calculated as:

$$\text{BVR} = \frac{V_{MSF}}{V_{YF}} = \frac{C_{SR}}{C_{SR} + C_{RF} + C_{B1} + C_{B2}} \tag{2.1}$$

The inherent stray capacitances of a usual three-phase induction motor are illustrated in a schematic diagram (Fig. 2-4) according to V. Hausberg et al. [14]. In all figures, real capacitors are depicted as solid units to distinguish them from the stray capacitances, which are depicted as dashed elements. Based on results obtained from literature [7, 11], current densities of EDM-currents and high-frequency *dv/dt*-currents in bearings smaller than $0.4\ \text{A}_{pk}/\text{mm}^2$ should not degrade bearing life, while bearing life may be affected by current densities greater than $0.8\ \text{A}_{pk}/\text{mm}^2$.
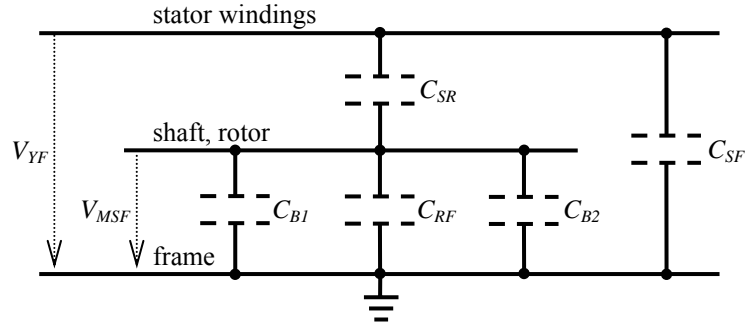
Fig. 2-4:   Equivalent electric circuit of the inherent stray capacitances in a usual three-phase induction motor, whereby C_{SR} is the capacitance between the stator windings and the rotor, C_{RF} is the capacitance between the rotor and the motor frame, C_{SF} is the capacitance between the stator and the motor frame, C_{B1} and C_{B2} are the capacitances of the bearings, V_{YF} is the star point-to-frame voltage and V_{MSF} is the motor shaft-to-frame voltage. To distinguish between stray capacitances and real capacitors, they are depicted in all figures dashed and solid, respectively.

In contrast to mains operated induction motors, which are fed with low-frequency sine waves (50 Hz or 60 Hz), the phase voltages applied by frequency converters to induction motors are high-frequency voltages (typically of a few kilohertz), e.g. high-frequency square wave voltages with variable pulse control factors supplied by voltage source DC-link frequency converters using PWM [8, 18]. Further, high-frequency capacitive currents emerge that are distributed along the stator windings, in particular along first few turns of the windings within the slots. These various capacitive current components distributed over the stator windings cause a resulting current, which generates high-frequency magnetic flux variations surrounding the rotor and the motor shaft. Hence, these flux variations are responsible for a high-frequency shaft end-to-end voltage, which initiates an equalising current (here a high-frequency

circulating current), whenever electrically possible. These high-frequency circulating currents are still subject of investigations.

During each switching operation of a frequency converter at least one phase voltage is switched over and hence also the stator-to-frame voltage and the motor shaft-to-frame voltage are changed. These transient phenomena in the stator-to-frame voltage (in the order of several kV/µs) and the motor shaft-to-frame voltage (in the order of several hundred V/µs) during the switching operations produce high-frequency dv/dt-currents, which charge or discharge the stray capacitances in the motor according to these voltage transients. These dv/dt-currents, created by steep slew rates of the phase voltages supplied by the frequency converter, partially flow back to the frequency converter across the bearings and the motor frame and along the PE-network. Current densities in the range from 0.15 A/mm^2 to 0.8 A/mm^2 have been calculated for typical high-frequency dv/dt-currents in bearings [11]. Therefore, the authors assumed that high-frequency dv/dt-currents will probably not cause bearing damages.

The properties of the PE-network also influence a drive system consisting of a frequency converter, an induction motor and a driven machine. High frequency currents, such as dv/dt-currents, flow along those paths in a drive system, which offer the lowest impedances in the high frequency regime. That means, these high-frequency currents may flow across a bearing in the motor and either along the shield of the power cable or through the motor frame and further back along the PE-network, but they may also flow through the motor shaft to the driven machine, there across a bearing to ground and back to the frequency converter. According to V. Hausberg et al. [14] the most dangerous situation for bearings will exist, if the motor frame has no or only an insufficient high-frequency grounding, while the motor shaft has good high-frequency grounding (Fig. 2-5), because then the ratio between the voltage across the bearings (V_{MSF}) and the star point-to-ground voltage (V_{YG}) is much greater than the BVR (equation (2.1)) under usual grounding conditions:

$$\frac{V_{MSF}}{V_{YG}} = \frac{C_{SF}}{C_{SF} + C_{RF} + C_{B1} + C_{B2}} \xrightarrow[C_{SF} \gg C_{RF} \, ; \, C_{SF} \gg C_{B1} \, ; \, C_{SF} \gg C_{B2}]{\lim} 1 \qquad (2.2)$$

The voltage across the bearings (V_{MSF}) is mainly determined by the stray capacitance C_{SF}, between the stator windings and the motor frame, because the capacitances C_{RF}, C_{B1} and C_{B2} can normally be neglected in relation to C_{SF}. At worst case, the voltage across the bearings can nearly reach to the value of the star point-to-ground voltage (equation (2.2)), unless breakdowns in the lubricant due to EDM-events will occur before [14]. High-frequency currents may cause high-frequency potential differences in

the PE-wire due to their high inductances with respect to high frequencies. Hence, a voltage between the motor frame and the ground, the motor frame-to-ground voltage (V_{FG}), is produced.
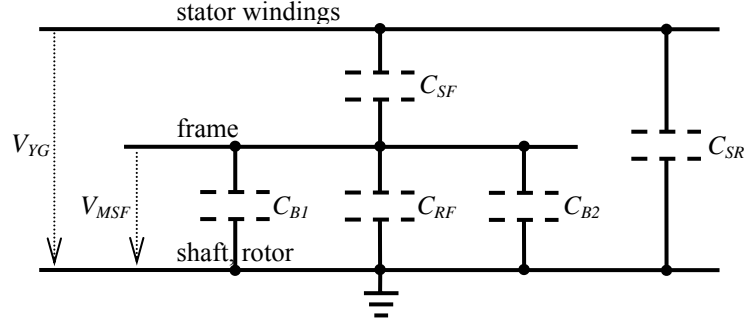
Fig. 2-5:   Equivalent electric circuit of a motor in the most dangerous situation [14], when the rotor has good high-frequency grounding and the motor frame has no or only insufficient high-frequency grounding. Here, C_{SR} is the capacitance between the stator windings and the rotor, C_{RF} is the capacitance between the rotor and the motor frame, C_{SF} is the capacitance between the stator windings and the motor frame, C_{B1} and C_{B2} are the capacitances of the bearings, V_{YG} is the star point-to-ground voltage and V_{MSF} is the motor shaft-to-frame voltage.

As long as the bearings of an induction motor are in the full-film lubrication regime, i.e. there are continuous lubricant films between the outer rings and the inner rings, respectively, and the rolling elements, the motor shaft is electrically insulated from the motor frame. From the electrical point of view, under these conditions a lubricant can be regarded as a dielectric and hence each bearing can be treated as a capacitor with the capacitance C_{B1} and C_{B2}, respectively. Due to the motor shaft-to-frame voltage (V_{MSF}) the bearing capacitances C_{B1} and C_{B2} and the capacitance between the rotor and the motor frame C_{RF} are charged and therefore EDM-currents through the bearing are possible. EDM-processes will occur as soon as the electrical field strength in a finite region across the bearing reaches the breakdown threshold of the lubricant. That can be caused either by a sufficiently high voltage across the bearing (V_{MSF}) or by a sufficiently small film thickness of the lubricant in the bearing. The lubricant film thickness in a bearing depends on the operating conditions, such as viscosity, temperature, rotational speed and load. Additionally, asperities at the surfaces of the raceways not only decrease the film thickness of the lubricant, but they also lead to a higher electrical field strength in their vicinity due to the well known needle effect. During EDM-processes high currents flow in very short times through the lubricant film and cause localised temperature rises, which are able to damage the lubricants as well as to generate craters at the surfaces of the raceways by melting. According to literature [11], EDM-current densities are in the range from 1.7 A/mm^2 to 5 A/mm^2, so they are accused to reduce bearing life. The EDM-energy E_{EDM}, available for discharges in bearings, is determined by the voltage $V_{MSF}(t_0)$ across the bearings at the time t_0 when the discharge starts, by

the bearing capacitances C_{B1} and C_{B2} and by the capacitance C_{RF} between the rotor and the frame [4]:

$$E_{EDM} = \tfrac{1}{2} \cdot (C_{RF} + C_{B1} + C_{B2}) \cdot V_{MSF}^2(t_0)$$ (2.3)

Due to these energies, which typically are in the order of a few hundred μJ, mirco-craters with diameters of a few μm are generated at the raceways of bearings [14]. The dependence of EDM-currents (I_{EDM}) on the lubricant breakdown voltage (V_{BD}) was investigated by V. Hausberg et al. [14] at drive systems, comprising different frequency converters and driven induction motors (Fig. 2-6). Nearly the same relation between the V_{BD} and I_{EDM} was found for different drive systems, as all results lay nearly at a straight line. Thus, by means of the slope of the straight line in Fig. 2-6 a common resistance can be determined as: $\Delta V_{BD} / \Delta I_{EDM} = 25.5 \text{ V} / 2.55 \text{ A} = 10 \ \Omega$.
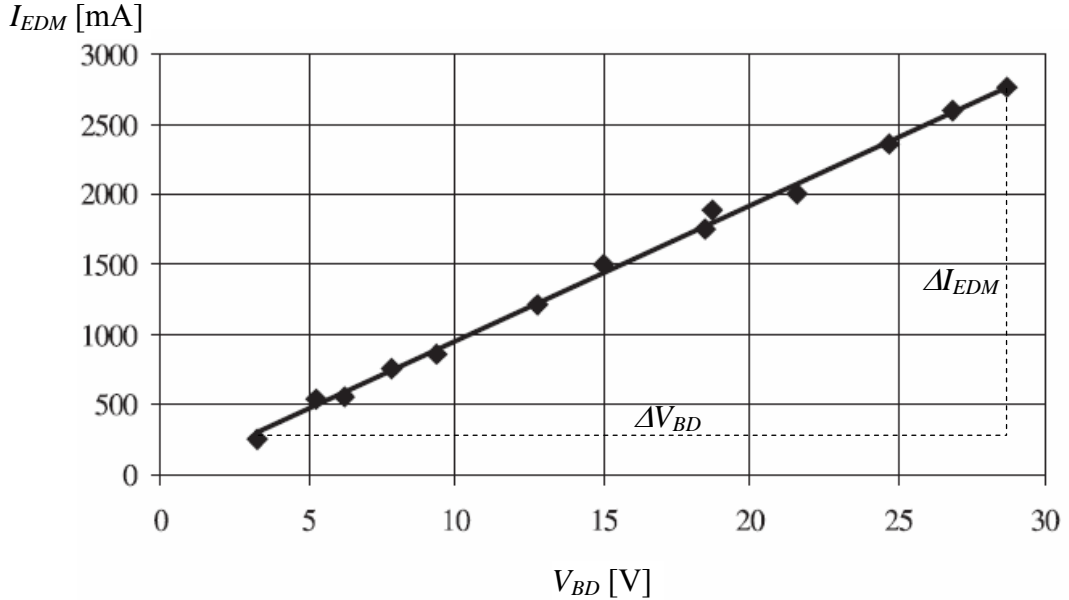
Fig. 2-6: Dependence of the EDM-current I_{EDM} on the lubricant breakdown voltage V_{BD} [14].

2.4 Counter measures against electrical current passage

Depending on the operating conditions, additional parasitic currents, such as high-frequency circulating currents, high-frequency dv/dt-currents, EDM-currents and currents in the PE-system, may be present in drive systems consisting of a frequency converter, an induction motor and a driven machine. Due to these currents in the bearings of induction motors as well as of driven machines not only the lubricants but also the surfaces of the raceways may be deteriorated or partly destroyed. These bearing damages may result in bearing malfunction and hence in motor failure or machine

failure. Therefore, various counter measures for the reduction or elimination of currents leading to bearing damages have been developed and investigated.

To reduce or and eliminate the motor shaft-to-frame voltage, caused by electrostatic charging or by the star point-to-frame voltage at frequency converter driven motors, grounding brushes have been used in numerous applications as electrical connections from the motor shaft to the motor frame. Such a system has to provide a low-resistance ohmic contact between the brush and the rotor as demanded by S. Bell et al. [13], D. Busse et al. [16] and V. Hausberg et al. [18]. Further, the wear and the build-up of an oxide layer at the surface of brushes must be taken into account [13, 16]. Therefore, maintenance and replacement of brushes are necessary in certain periods and also the motor frame integrity has to be verified for proper operation [18, 19].

Instead of grounding brushes also conductive greases are used, but test data obtained with a four ball wear tester by D. Busse et al. [16] showed an increase of wear by approximately 60 % for conductive greases containing metallic particles. A much better conductive additive for greases is graphite, but conducting lubricants comprising graphite loose their effectiveness with time [13].

Grounding brushes particularly reduce the motor shaft-to-frame voltage, but due to the short-circuiting of one bearing with a grounding brush low-frequency circulating currents may still flow through the other bearing and may cause bearing damage [8, 9, 13, 18]. To suppress low-frequency circulating currents, the non-drive-end bearing must be insulated, because circulating currents will flow through the non-drive-end bearing and a bearing in the driven machine, if the drive-end bearing is insulated instead of the non-drive-end bearing.

High-frequency dv/dt-currents, which flow via ground back to the frequency converter, can only be reduced by using two insulating bearings in the motor [8, 9, 13]. To avoid the flow of high-frequency dv/dt-currents from the motor along the shaft to the driven machine and subsequent bearing failure, an electrically insulating coupling in the shaft or a grounding brush at the shaft must be installed. If grounding brushes are used in such applications in combination with insulated bearings or sometimes exclusively, they should provide sufficient high-frequency grounding conditions [9].

Two types of insulated bearings must be distinguished, coated bearings and hybrid bearings (ceramic rolling element bearings) [2, 13, 16, 18, 19]. While coated bearings, comprising an insulating layer, are able to prevent low-frequency circulating currents,

they represent an additional capacitance with regard to high-frequency currents, *dv/dt*-currents and high-frequency circulating currents. That means, high-frequency currents are not eliminated by coated bearings, but they can obviously be reduced. To be effective, the capacitance of theses insulating layers should be much smaller than the bearing capacitance (C_{B1}, C_{B2}) [16]. But up to the present insulating layers for bearings, that have such extremely small capacitances, have not been found. Further must be taken into account, that the lost heat generated in a motor is transferred partially through the bearings to the motor frame. Hence, in addition, a good heat conductance of insulating layers is necessary. In contrast, by means of hybrid bearings the paths for EDM-currents, high-frequency *dv/dt*-currents and circulating currents can be interrupted due to the ceramic balls, but it should be pointed out that the motor shaft-to-frame voltage still exists and parasitic electric currents may find other paths, e.g., through the bearings of a tachometer or a driven machine, and there they may cause damages in the bearings [2, 19]. To prevent bearings of the driven machine from damage, there must be installed either hybrid bearings also in the driven machine or an insulating coupling in the motor shaft. The electrical insulation of inner rings and outer rings in hybrid bearings by the ceramic balls avoids bearing currents, but one disadvantage is that the build-up of an electrical potential difference between the inner ring and the outer ring is possible [20]. Therefore, e.g. in hard disk drives, ferro-fluid seals are used to avoid damages due to voltages across the hard-disk interfaces. K. B. Klaassen et at. [20] describe the generation of such a voltage by the build-up of a Helmholtz electrical double layer at the solid-liquid phase boundary in the bearing and charge separation due to the motion of the ceramic balls through the grease. By using ferro-fluid seals in a spindle motor, the motor shaft-to-frame voltage could be short-circuited and damage of the hard disk was prevented [20].

The installation of an electrostatic shield between the stator windings and the rotor in induction motors effects a great reduction of the capacitive coupling between the stator windings and the rotor, because the shield acts as a Faraday cage [8, 13, 16]. Without such capacitive coupling, no motor shaft-to-frame voltage is generated by the star point-to-frame voltage. If no motor shaft-to-frame voltage is present in the motor, EDM-currents will not be possible. However, an electrostatic shield does not prevent circulating currents and high-frequency *dv/dt*-currents. Further, the shield must be installed in such a way that the stator laminations are not short-circuited to avoid circulating eddy currents. The electrostatic shield has to cover the whole stator windings including their ends and has to be well grounded at the motor frame for proper function. The air gap between the stator windings and the rotor in inductions motors usually is

very small, therefore the installation of an electrostatic shield in an induction motor generally is difficult and expensive.

Different cablings, filters, common-mode chokes and common-mode transformers have been installed between frequency converters and driven motors to reduce over-voltages, *dv/dt*-currents and electromagnetic interference (EMI). Various applications using filters, common-mode chokes or common-mode transformers have been studied by A. von Jouanne et al. [19]. Due to mismatch of the characteristic impedances of power cables and motors, over-voltages at the motor terminals may be generated by reflected voltage waves. The magnitudes of the voltages at the motor terminals may reach two or three times the magnitudes of the incident voltage waves [19, 21]. In general, the longer the power cables and the higher the slew rates (*dv/dt*) of the phase voltages are, the higher are the generated over-voltages. Motor insulations as well as cable insulations are stressed by over-voltages. Motor terminal filters and inverter output filters, usually consisting of capacitances and resistances, can reduce over-voltages, but they must be adjusted to each application [19]. Common-mode cokes and common-mode transformers are interacting inductances and are able to attenuate *dv/dt*-currents and EMI, whereby common-mode transformers generally have a better effectiveness than chokes. The high switching speeds of frequency converters cause oscillatory currents with a frequency range from 100 kHz to several MHz [19]. Therefore, magnetic fields and wide-band EMI are generated. If the phase conductors and the PE-wire of the motor cable were separated and hence a loop was formed, substantially more EMI could be measured in contrast to a set-up, where the phase conductors and the PE-wire were bundled [19]. Different cabling systems between a frequency converter and a driven motor were investigated by E. J. Bulington et al. [21] to reduce EMI and *dv/dt*-currents in the grounding. The authors recommended the use of shielded power cables comprising PE-wires, which are connected to the shields at both ends of the cables. These power cables should be installed not only between the frequency converter and the driven motor but also between the frequency converter and the supply transformer. EMI is minimised by this cabling, as the phase conductors and the PE-wires and shields are very close to each other. Due to the shield, *dv/dt*-currents in the grounding will be mitigated, because they flow through the shield, which provides a good high-frequency connection from the motor back the frequency converter and the supply transformer. A similar cabling concept for the mitigation of *dv/dt*-currents and EMI was described by P. J. Link [17]. A good grounding of the motor frame with respect to low- and high-frequency currents prevents the build-up of electric potentials between motor frame and ground, but current passage through the motor and hence also through bearings is not totally eliminated.

The sum of the phase voltages transferred from a frequency converter to a driven motor is not zero and is often denoted as common-mode voltage. This common-mode voltage results in the star point-to-ground voltage, between the motor star point and ground. To avoid the passage of currents through bearings caused by these voltages, common-mode mitigation techniques have been developed. The installation of an isolating transformer between the frequency converter and the driven motor can reduce the common-mode voltage at the motor, because measurements showed that, the common-mode voltage is nearly not transferred to the secondary side of the transformer [18]. But usually such transformers are available only for low-power applications. M. M. Swamy et al. [22] has developed a circuit for installation between a frequency converter and a driven motor to attenuate the common-mode voltage. This circuit consists of a three-phase iron core transformer to create the common-mode voltage and a common-mode transformer to couple the inverted common-mode voltage to the frequency converter output phases. For this purpose, one end of each winding of the three-phase iron core transformer is connected to one of the output phases of the frequency converter, whereas the other ends of the windings are all interconnected with one end of the fourth winding of the common-mode transformer. The other end of the fourth winding is connected to the mid-point M of the DC-link (Fig. 2-1). The three other windings of the common-mode transformer are installed each at one phase conductor between the frequency converter and the driven motor. In this way, the common-mode voltage can be attenuated but not totally eliminated. The transformers used have to work at high powers and high frequencies, and must not saturate due to low-frequency signal components. Alternatively, by disconnecting the supply transformer from ground, D. Hyppio [4] could reduce the common-mode voltage. Further mitigation of the common-mode voltage was reached by installing external capacitors via series resistors between each frequency output phase and ground and by providing common-mode chokes in the output phases between the frequency converter and the driven motor. Disadvantages of an ungrounded supply transformer are the possible increase of transient voltage stress and high-frequency current pulses at the line-to-ground MOV (metal oxide varistor) network.

In addition, different active systems for common-mode voltage elimination have been designed. S. Ogasawara et al. [23] constructed an active circuit consisting of three wye-connected capacitors, a push-pull emitter follower and a common-mode transformer. The common-mode voltage is picked up by the three wye-connected capacitors, which are connected each at one end to one of the output phases of the frequency converter, whereas their other ends are all interconnected with the push-pull emitter follower. The push-pull emitter follower is supplied by the DC-link and applies

a voltage equal to the common-mode voltage to the fourth winding of the common-mode transformer. The three other windings are installed in such a way between the frequency converter and the driven motor that a voltage reverse to the common-mode voltage is coupled to the output phases. This circuit must be designed to work at high frequencies as well as at high voltage and power levels.

In contrast, a new converter type, a so-called a four-leg converter, was proposed by A. L. Julian et al. [24]. This special converter provides a fourth output phase, which is coupled to the other three output phases via an LC-filter, installed between the frequency converter and the driven motor, to eliminate the common-mode voltage. The modulation strategy of the converter must be modified to be able to control also the voltage of the fourth output phase.

Another concept of common-mode mitigation was pursued by A. von Jouanne et al. [25]. They designed a dual-bridge inverter, which consists of two separate inverter bridges, to be able to supply a three-phase dual-voltage induction motor comprising two triples of windings. The switching pattern of the two inverter bridges has to be anti-symmetric. That means, if one output phase of the first inverter is switched to the positive voltage level, the corresponding output phase of the second inverter must be switched to the negative voltage and vice versa. Proper connection of all six windings is necessary to produce the same magnetic flux direction, although the corresponding windings are supplied by voltages of different polarity. So the electric fields produced in the corresponding windings cancel each other, while the generated magnetic fluxes are added. This dual-bridge inverter needs a special motor and is applicable only for low and medium voltage levels. H. Zhang et al. [26] redesigned that inverter and developed a reduced-switch dual-bridge inverter, which needs only eight power switches instead of the first described inverter, which has twelve power switches.

An overview of the effectiveness of different counter measures against bearing currents was given by the IEC [12] and is listed in Tab. 2-2.

| Counter measure | Current type | | | Additional comments |
	Circulating currents	Shaft grounding currents	Capacitive discharge currents	
1) NDE insulated, or ceramic rolling elements	Effective	Not effective: Only protects one bearing.	Not effective: Only protects one bearing.	NDE insulated to avoid need for an insulated coupling.

Counter measure	Current type			Additional comments
	Circulating currents	Shaft grounding currents	Capacitive discharge currents	
2) NDE and DE insulated, or ceramic rolling elements	Effective: One insulated bearing is adequate for this current type.	Effective	Effective: May require additional brush contact.	Most effective for small frame sizes. Less practical for large frame sizes.
3) NDE and DE insulated, or ceramic rolling elements + additional insulated coupling and shaft grounding brush	Effective	Effective	Effective	Most effective (especially for larger machines). Helps to prevent possible damage to driven load. Servicing necessary.
4) NDE insulated One DE brush contact	Effective: Brush unnecessary for this current type. NDE tachometer bearing, if fitted, needs protection.	Effective: Does not protect bearings in driven load.	Effective: Care needed to ensure low brush contact impedance.	Servicing necessary. Most practical for large frame sizes. DE brush used to avoid need for an insulated coupling.
5) One brush contact No bearing insulation	Not effective: Only protects one bearing.	Effective: Does not protect bearings in driven load.	Effective: Care needed to ensure low brush contact impedance.	Servicing necessary
6) Two brush contacts, DE and NDE No bearing insulation	Effective: Care needed to ensure low brush contact impedance.	Effective: Does not protect bearings in driven load.	Effective: Care needed to ensure low brush contact impedance.	Servicing necessary.
7) Low resistance lubrication and/or carbon-filled bearing seals	Poor	Poor	Effective: Depends on condition of materials.	No long term experience. Lubrication effectiveness reduced.
8) Rotor in Faraday cage	Not effective	Not effective	Very effective	Problems from converter generated circulating currents that normally only occur in larger motors.
9) Common mode voltage filter	Effective: Reduced HF voltage also decreases LF currents.	Effective	Effective	Greatest reduction of common-mode voltage if filter is fitted at converter output.

Counter measure	Current type			Additional comments
	Circulating currents	Shaft grounding currents	Capacitive discharge currents	
10) Insulated coupling	Not effective	Very effective	Not effective	Also prevents possible damage to driven load.
11) Frame to driven load connection	Not effective	Effective	Not effective	Also prevents possible damage to driven load.

Tab. 2-2:   Effectiveness of counter measures against bearing currents [12]. DE and NDE denote the drive-end bearing and the non-drive-end bearing, respectively, of a motor.

The insulation of the non-drive-end bearing instead of the drive-end bearing (Tab. 2-2) avoids the need of an insulated coupling in the motor shaft between the motor and the driven machine only for the break of circulating currents. If the drive-end bearing is insulated, such an insulated coupling will be necessary, otherwise circulating currents will flow along the motor shaft, the driven machine, the bearings in the driven machine, the ground, the drive-end bearing of the motor and back to the motor shaft.

Circulating currents, EDM-currents (capacitive discharge currents) and *dv/dt* high-frequency currents (shaft grounding currents) (Tab. 2-2) in the bearings of frequency converter driven motors can be avoided by means of ceramic rolling element bearings (hybrid bearings), but due to the capacitances of the insulating layers coated bearings can only break circulating currents [2, 13, 16, 19]. If hybrid bearings are used in motors, it must be considered that the motor shaft-to-frame voltage will still exist and parasitic currents may damage the bearings of the driven machines. Therefore the driven machines must be provided either with hybrid bearings or an insulating coupling in the motor shaft. In the meantime, hybrid bearings are available in more and more dimensions and they also have got less expensive.

Low resistance lubricants (Tab. 2-2) usually have too low conductivity for effective conducting of circulating currents. Due to the capacitance and the remaining resistance a low resistance lubricant can not avoid capacitive discharge currents and shaft grounding currents. Conductive lubricants often contain metallic particle and therefore their use increases the wear in the bearings [16] and greases including graphite loose their effectiveness with time [13].

The installation of a Faraday cage in induction motors normally is very difficult and expensive [8, 13, 16]. This counter measure greatly reduces capacitive discharge

currents, but it does not prevent from circulating currents and shaft grounding currents. Some of the techniques described in this chapter, such as brushes, do not work reliably and need consistent service, others, such as several filters and circuits installed between the frequency converter and the driven motor, may only more or less reduce parasitic currents and some special designed circuits and converters may be more effective, but they are normally very expensive.

2.5   Deterioration of lubricants due to electrical current passage

The application of lubricants, greases and oils is limited to different temperature ranges. R. A. Guyer Jr. [27] specifies various classifications of greases with respect to their temperature range: general-purpose (-40 °C to 120 °C), high-temperature (-19 °C to 149 °C), medium-temperature (0 °C to 93 °C), low-temperature (-55 °C to 107 °C) and extremely-high-temperature (up to 232 °C). Lubricants should not be heated up to temperatures above their specified temperature limit, because the life time of lubricants is primarily affected by temperature. Deterioration, sludge formation, burned carbon deposits, lubricant caking and varnished raceways will occur due to accelerated oxidation, catalytic decomposition, evaporation and melting, if a lubricant is exposed to temperatures above its temperature limit. Useful temperature ranges for some types of greases are given by R. A. Guyer Jr. [27]: petroleum (-30 °C to 85 °C), diester-polyester (-45 °C to 85 °C), silicone (-35 °C to 142 °C), silicone-diester (-73 °C to 85 °C), polyglycol (-27 °C to 85 °C).

Fig. 2-7:   Deterioration of a lubricant due to electric current passage [2]. Wide regions of the lubricant appear black discoloured by burned carbon deposits and lubricant caking.

Bearing damages due to electric current passage may generate craters, and fluting or pitting at the raceways of rolling elements, inner rings or outer rings. During these processes, finite regions of the surfaces are exposed to temperatures above the melting point of the metallic components, usually made of bearing-qrade steel (typically 100Cr6 with a melting point of approximately 1530 °C). These high temperatures are definitely above the temperature limits of all types of lubricants and may therefore partially deteriorate or destroy the lubricants. Hence, these deteriorated lubricants will loose their lubricity and subsequently cause bearing failure. A lubricant deteriorated due to electric current passage is shown in Fig. 2-7 [2]. Wide regions of the lubricant appear black discoloured by burned carbon deposits and lubricant caking due to electric current passage aside from the metal deposits coming from breaking loose material of craters.

3   Stray capacitances and current loops in a drive system comprising a frequency converter, a controlled motor and a driven machine

Several parasitic currents may flow through induction motors and may cause bearing damage, if they pass through a bearing of a motor or a driven machine. The understanding of the generation of these parasitic currents and the knowledge of their loops within a drive system, comprising a frequency converter, a controlled motor and a driven machine, is necessary for the development of effective counter measures. It is common knowledge, that inherent stray capacitances exist in each induction motor. Due to the high switching frequencies and the high slew rates in the phase voltages (*dv/dt*) supplied by modern frequency converters, the influence of the stray capacitances on parasitic currents in motors is intensified. The different parasitic currents, which may appear in frequency converter driven motors and machines, have not always been clearly distinguished. G. Preisinger [2] has acquired a good survey of the parasitic currents, which are described ensuing to the specification of the stray capacitances of usual induction motors.

3.1   Inherent stray capacitances in induction motors

Before parasitic currents and their loops in induction motors can be investigated, the inherent stray capacitances that are present in typical motors must be known, because they are of great impact for the generation of parasitic currents as well as for the current loops in induction motors. Inherent stray capacitances and their influence on parasitic currents in motors have been studied by many authors [2-4, 7, 9, 11, 14, 17, 28-30]. A schematic diagram of a drive system comprising a frequency converter, a controlled induction motor and a driven machine is illustrated in Fig. 3-1. The stray capacitances, which are shown in this diagram, represent the capacitive couplings between several different components of an induction motor. Although these capacitive couplings are locally distributed along certain areas of the components involved, they may generally be treated as single capacitances. Therefore, in all figures the stray capacitances are depicted as dashed elements, to clearly distinguish them from real capacitors, which are depicted as solid units. The stray capacitances within an induction motor are the capacitance C_{SF} between the stator windings and the motor frame, the capacitance C_{SR} between the stator windings and the rotor, the capacitance C_{RF} between the rotor and the motor frame and the capacitances C_{B1} and C_{B2} of the bearings (Fig. 3-1).
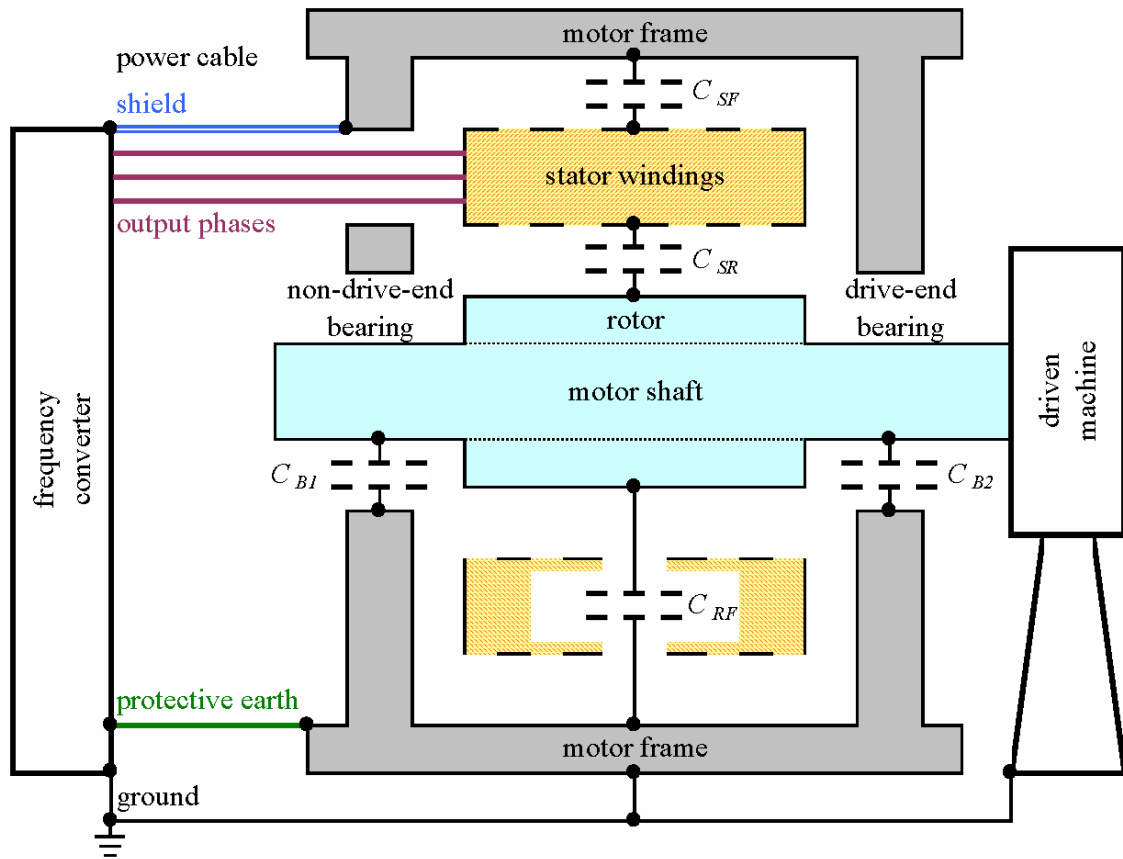
Fig. 3-1:   Schematic diagram of a drive system comprising a frequency converter, a controlled induction motor and a driven machine. The power cable from the frequency converter to the motor consists of a shield (blue), three wires (violet) for the output phases of the frequency converter and a protective earth wire (green). The cross-sectional view of a motor along the motor shaft is illustrated. The inherent stray capacitances of a motor are shown, whereby C_{SF} is the capacitance between the stator windings (yellow) and the motor frame (grey), C_{SR} is the capacitance between the stator windings and the rotor (light-blue), C_{RF} is the capacitance between the rotor and the motor frame and C_{B1} and C_{B2} are the capacitances of the drive-end bearing and the non-drive-end bearing, respectively. All these capacitances represent the capacitive couplings between the corresponding motor components, which are distributed along certain areas of these components.

From the electrical point of view, bearings may be regarded as capacitances, if they are operated in the full-film lubrication regime. As long as bearings are in the full-film lubrication regime, continuous insulating lubricant films exist between the inner rings and the outer rings, respectively, and the rolling elements. Four states of electrical conductivity, available in rolling element bearings, are described by G. Preisinger [2]. These four states, the metallic conductivity state, the resistive state, the capacitive state and the state of occurring EDM-events, depend on the lubrication regime of the bearing. The metallic conductivity state exists, when the bearing has no or very low rotational speed. That means, the bearing is in boundary lubrication regime and no uniformly lubricant film separates the surfaces of rolling elements and raceways. Metallic contact in the bearing leads to very low ohmic resistance. Thus, currents applied across the bearing flow immediately. The mixed lubrication regime of a bearing is reached at

increased rotational speed, depending on the bearing load and the surface roughness. The mating surfaces in the contact area are partially separated by a thin lubricant film resulting in increased and unstable ohmic resistance. In this state, fritting may occur in the bearing. If the rotational speed is high enough, the bearing will reach the full-film lubrication regime, i.e., a continuous lubricant film completely separates the metal surfaces in contact area. Under these conditions, the bearing can be treated as capacitor from the electrical point of view. That means, only capacitive currents may flow through the bearing during charging or discharging. The occurrence of EDM-events requires two preconditions. First, the bearing must be in the full-film lubrication regime, so that a continuous insulting lubricant film exists in the bearing. Secondly, across the bearing must be present a potential difference, which exceeds the breakdown threshold of the lubricant in a finite region. As soon as the breakdown threshold is reached, an EDM-process is initiated, which is assumed to occur in the form of a spark [2]. During this process the voltage across the bearing breaks down and a current flow across the bearing starts. However, the motion of the bearing causes destruction of the spark, but as soon as the voltage across the bearing reaches again the breakdown threshold in any finite region of the contact area another EDM-process starts. Repeating occurrence of EDM-events and caused electric currents passage through the bearing generate crates at rolling elements and raceways due to very high local temperatures and damages bearing elements [2].

Based on design data for four pole 460 V AC induction motors and associated bearing dimensions, stray capacitances of motors in the power range from 5 HP to 900 HP have been calculated [11, 31-33]. The ranges of the values for the stray capacitances are listed in Tab. 3-1. With rising motor power the capacitances C_{SF}, C_{SR} and C_{RF} increase, whereas the bearing capacitances C_{B1} and C_{B2} decrease. The values of the stray capacitances for a test motor (15 HP, 460 V) were calculated by Erdman et al. [34] (Tab. 3-1).

stray capacitance	C_{SF}	C_{SR}	C_{RF}	C_{B1}, C_{B2}
capacitance range [nF]	4 – 100	0.1 – 1	1 – 6	0.3 – 0.1
typical set of capacitances [nF]	11	0.1	1.1	0.1

Tab. 3-1:   Range of the values for stray capacitances of induction motors in the power range from 5 HP to 900 HP, calculated based on design data for four pole 460 V AC motors and associated bearing dimensions [11, 31-33]. Whereby, C_{SF} is the capacitance between the stator windings and the motor frame, C_{SR} is the capacitance between the stator windings and the rotor, C_{RF} is the capacitance between the rotor and the motor frame and C_{B1} and C_{B2} are the capacitance of each bearing. A typical set of stray capacitances, calculated by Erdman et al. [34] for a test motor (15 HP, 460 V), is given in the lowest row.

3.2 Electrical potential at the motor star point of induction motors driven by frequency converters

Mains operated induction motors are supplied by three sinusoidal phase voltages, with phase shifts against each other of $2\pi/3$. Therefore, under usual operating conditions, the sum of the three-phase voltages and hence the star point-to-ground voltage in mains operated induction motors are at all times zero. In contrast, the sum of the three-phase voltages (V_1, V_2 and V_3) generated by a frequency converter generally does not vanish and a star point-to-ground voltage V_{YG} between the motor star point Y and the ground G exists. Possible shapes of the phase voltages generated by a voltage source DC-link frequency converter using PWM are depicted in Fig. 3-2.
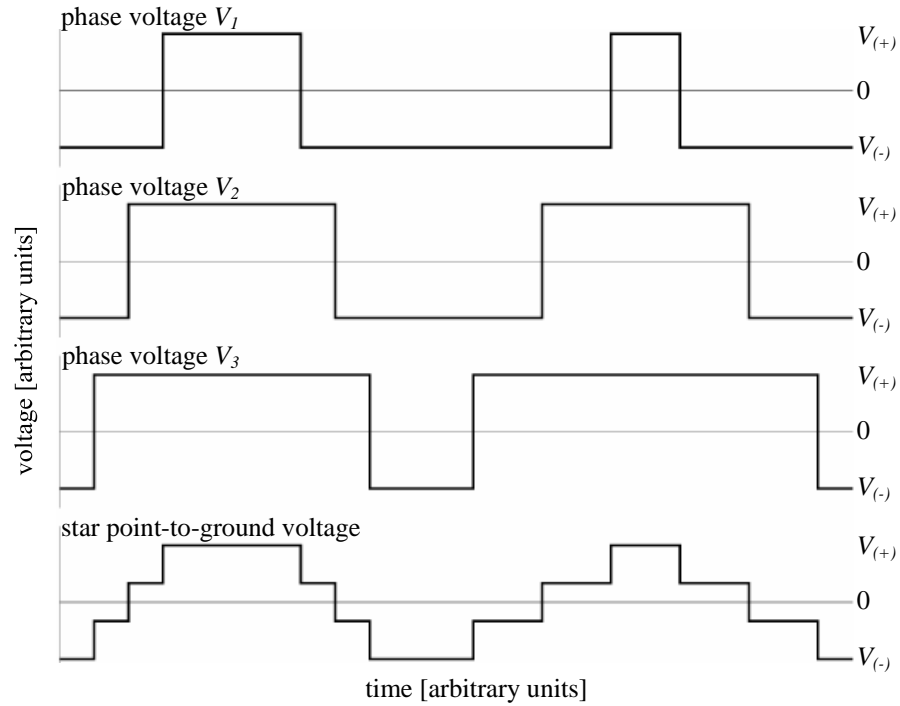
Fig. 3-2: Possible shapes of the phase voltages V_1, V_2 and V_3 generated by a voltage source DC-link frequency converter using PWM and the resulting star point-to-ground voltage V_{YG}. $V_{(+)}$ and $V_{(-)}$, respectively, are the voltages at the positive and the negative voltage rail of the frequency converter referred to ground.

In this figure also the resulting star point-to-ground voltage V_{YG} is shown, which can be calculated from the phase voltages [2, 3, 4, 7]:

$$V_{YG} = \tfrac{1}{3}(V_1 + V_2 + V_3) = \begin{cases} V_{(+)} \\ \tfrac{1}{3}V_{(+)} \\ \tfrac{1}{3}V_{(-)} \\ V_{(-)} \end{cases} \qquad (3.1)$$

The two discrete voltage levels $V_{(+)}$ and $V_{(-)}$ (Fig. 2-1) referred to ground, which are supplied by the frequency converter and available for each of the phase voltages, yield to four discrete voltage levels of the star point-to-ground voltage (Fig. 3-2). If one phase voltage is switched over, i.e. it is changed to the other voltage level ($V_{(+)}$ or $V_{(-)}$), then also the star point-to-ground voltage is transferred to another voltage level. The star point-to-ground voltage V_{YG} and the star point-to-frame voltage V_{YF}, between the motor star point and the motor frame, will be equal, if there is no potential difference between the grounding of the frequency converter and the grounding of the driven induction motor.

3.3   Currents due to electrostatic discharges

The mechanisms causing a potential difference between the rotor and the motor frame have been described in chapter 2.2. As long as the bearings of a motor are in the full-film lubrication regime, i.e. a continuous lubricant film exists between the inner rings and the outer rings, respectively, and the rolling elements, the bearings act as capacitors with the capacitances C_{B1} and C_{B2}. A potential difference across the bearings may lead to electrostatic discharges and hence to discharge currents in the bearings. The repeated initiation of EDM-processes due to the motor shaft-to-frame voltage generated in frequency converter driven motors is described in chapter 3.7.

3.4   Circulating currents

Asymmetries and variations of the magnetic flux in induction motors may induce a potential difference along the motor shaft (shaft end-to-end voltage) and hence may cause low-frequency and high-frequency circulating currents as described in chapters 2.2 and 2.3. Low-frequency circulating currents only can flow, if the bearings are in the metallic conductivity or the resistive state. Bearings may be damaged, when these currents are broken, because the voltage across the bearings may rise extremely high due to the inductance of the circuit being interrupted. High-frequency circulating currents [8, 18] and their effects on bearing damages are not completely clarified. Circulating currents flow from the motor shaft through one bearing, along the motor frame and through the other bearing back to the motor shaft (Fig. 3-3). Another possible way for circulating currents extends along the motor shaft to a bearing of the driven machine, through this bearing to ground, from the ground to the motor frame and from the motor frame through the non-drive-end bearing of the motor back to the motor shaft (Fig. 3-3). To break both current loops, the non-drive-end bearing should be insulated (chapter 2.4).

Fig. 3-3: Possible circulating current loops within a motor (red solid line) or via a driven machine (red dot and dash line) are drawn in the schematic diagram of a drive system as described in Fig. 3-1.

3.5   High-frequency *dv/dt*-currents

High-frequency *dv/dt*-currents are generated in each instant, when any of the phase voltages is switched over, i.e. they occur during each switching operation of the frequency converter, as described in chapter 2.3. High-frequency *dv/dt*-currents flow in the power cable along the wires for the output phases from the frequency converter to the stator windings, where they are split up (Fig. 3-4). One branch (*a*) runs to the motor frame across the capacitance C_{SF}, between the stator windings and the motor frame, while another branch (*b*) extends from the stator windings across the capacitance C_{SR} to the rotor and across the parallel capacitances C_{RF}, C_{B1} and C_{B2} to the motor frame (sub-branches *b1*, *b2* and *b3*). All these branches (*a*, *b1*, *b2* and *b3*) reunite at the motor frame (F_R) and the circuit is closed via the shield of the motor cable, the PE-wire or ground (*e*) (Fig. 3-4). Usually, the shield of a motor cable is a good high-frequency grounding and provides the lowest impedance for high-frequency currents. Thus *dv/dt*-currents normally flow along the shield. If there is only an insufficient or no high-frequency grounding, *dv/dt*-currents can also flow along the PE-wire or ground,

depending on their high-frequency impedances. In addition, a *dv/dt*-current can also flow via the motor shaft, a bearing of the driven machine (*f*) and ground. Both bearings in a motor have to be insulated to reduce or break the high-frequency current in the motor, but to inhibit current flow along the motor shaft to the driven machine, either a grounding brush or an electrically insulating coupling must be installed at the motor shaft (chapter 2.4).
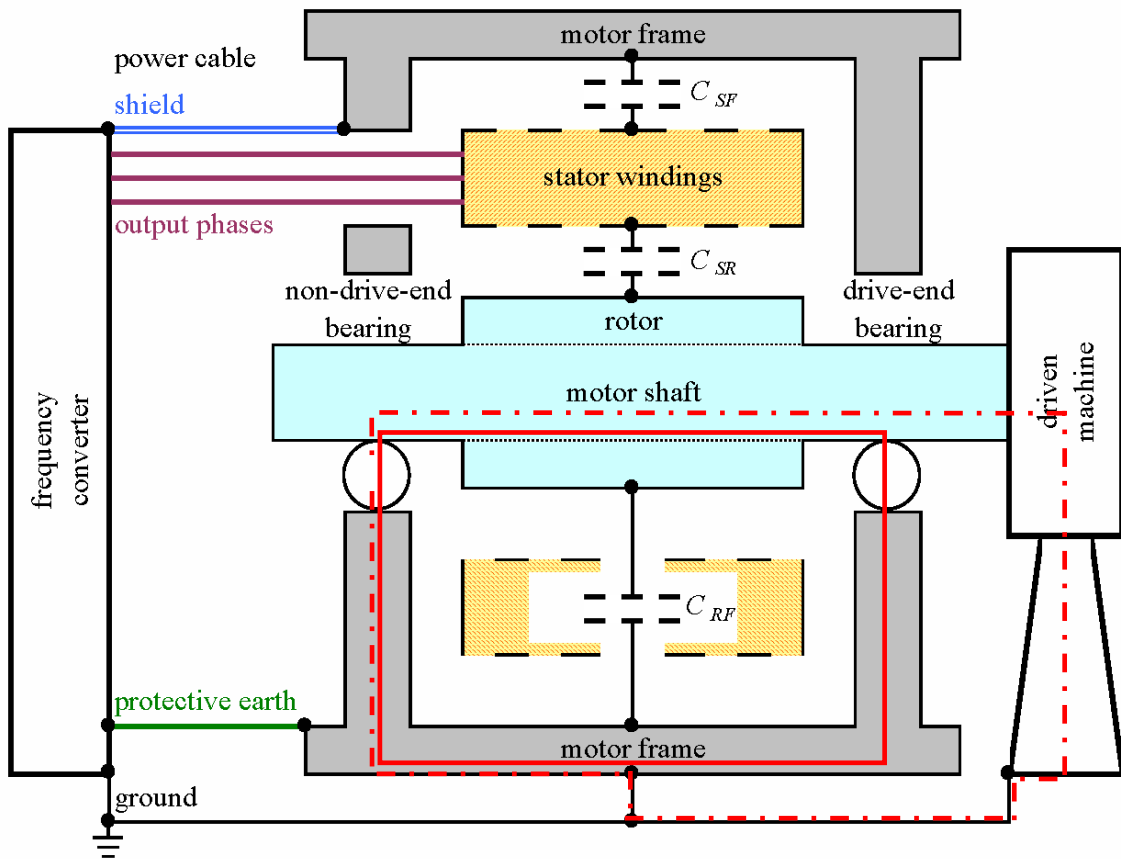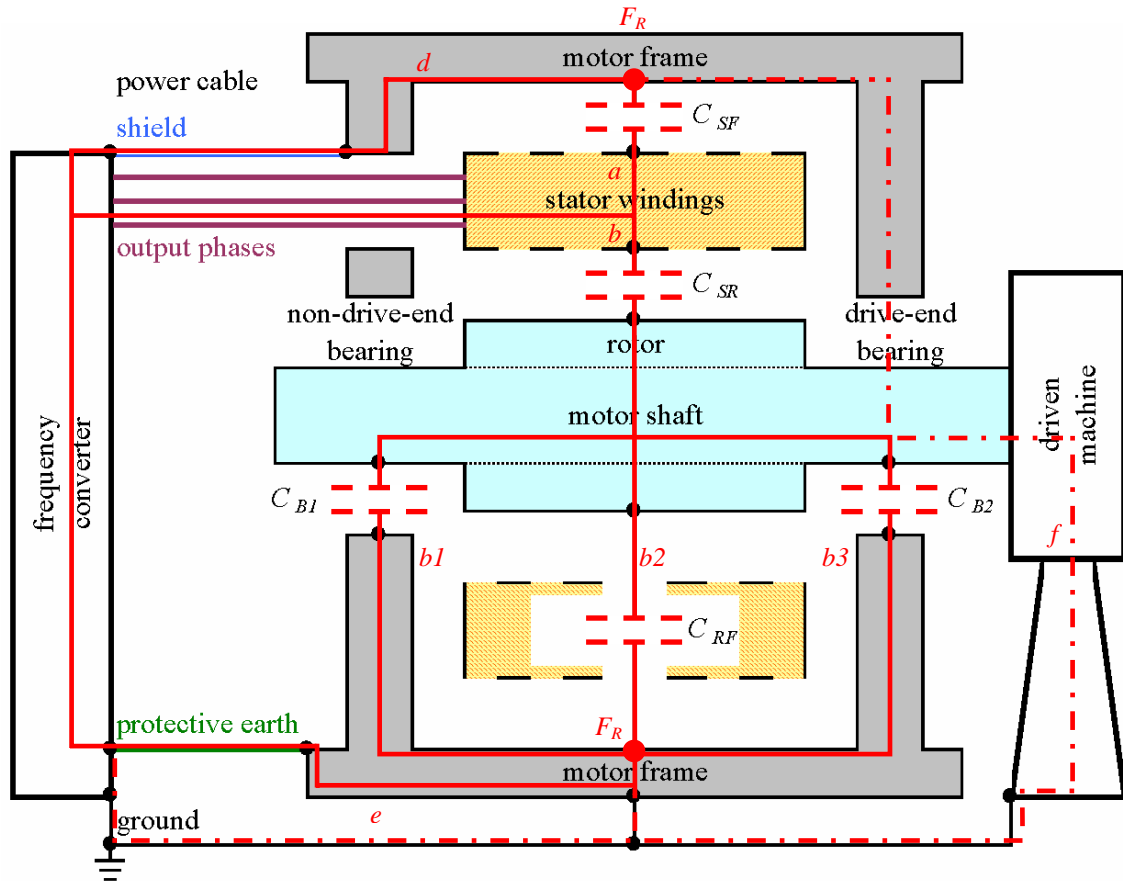

Fig. 3-4:   Possible high-frequency *dv/dt*-current loops within a motor (red solid line) or via a driven machine (red dot and dash line) are drawn in the schematic diagram of a drive system as described in Fig. 3-1. Between the stator windings and the motor frame the high-frequency *dv/dt*-current loop is spilt up into the branches *a* and *b*, whereby branch *b* is divided into the sub-branches *b1*, *b2* and *b3*. All these branches reunite at F_R . Usually, the shield (blue) of a motor cable provides the lowest impedance for high-frequency currents. Thus, high-frequency *dv/dt*-currents normally flow along the shield (*d*). If there is only an insufficient or no high-frequency grounding, high-frequency *dv/dt*-currents can also flow along path *e*, the protective earth wire (green) or ground, depending on their high-frequency impedances. In addition, high-frequency *dv/dt*-current can also flow via the motor shaft, a bearing of the driven machine (*f*) and ground.

3.6   Currents in the protective earth (PE) system

The frames of a driven motor and a frequency converter may be electrically interconnected by the ground (earth), the PE-wire or a shield in the power cable. Well-defined electrical properties of the ground usually can not be guaranteed, therefore

PE-wires are used to ensure adequate electrical grounding connections. However, this connection is often not sufficient for high-frequency currents, such as *dv/dt*-currents, because of its high inductance with respect to high-frequency currents (chapter 2.3, 2.4 and 3.5). Therefore, additional high-frequency groundings must be installed, otherwise high-frequency currents flow along the PE-wires. High-frequency groundings have to provide high-frequency inductances, which are as small as possible. If only an insufficient or no high-frequency grounding exists at a motor, the resulting high inductance leads to an electrical potential difference between the motor frame and the frame of the frequency converter and ground, respectively. In this case, a frame-to-ground voltage (V_{FG}) between the motor frame and ground is generated. Depending on the magnitude of the *dv/dt*-currents and the inductance of the PE-wires, voltage peaks of up to 100 V may occur at V_{FG} [17]. To minimise the inductance of the PE-wires, they should be thick and they must not have any loops. Further, the usage of shielded power cables can obviously reduce the inductance of the grounding as well as EMI, because shields can be designed as high-frequency groundings and because they enclose between the frequency converter and the driven motor all wires, the wires for the output phases as well as the PE-wires, which may generate EMI. It should be pointed out, that it is necessary that there does not exist any other electrical connection between the frames of the frequency converter and the controlled motor, except of the PE-wire and the shield in the power cable.

3.7   Electric discharge machining (EDM)-currents

Due to the stray capacitances in motors and the star point-to-frame voltage V_{YF} between the motor star point and the frame of motors driven by frequency converters, the motor shaft-to-frame voltage V_{MSF} is generated (chapter 2.3) and depends on the magnitudes of the stray capacitances and the star point-to-frame voltage (equation (2.1)). The shape of the motor shaft-to-frame voltage is similar to the shape of the star point-to-frame voltage, i.e. both have four different voltage levels. If both bearings of a motor are in the full-film lubrication regime and there are no brushes or other means for electrical grounding the motor shaft, the motor shaft will be electrically insulated from the motor frame and the motor shaft-to-frame voltage will develop. The bearing capacitances C_{B1} and C_{B2}, and the capacitance between the rotor and the motor frame C_{RF} are charged during the switching operations of the frequency converter by means of *dv/dt*-currents. The motor shaft-to-frame voltage across these stray capacitances is determined by the voltage V_{YF} and the capacitances C_{SR} , C_{RF}, C_{B2}, and C_{B1}, according to equation (2.1). Using typical values for the stray capacitances of motors (15 HP, 460 V, Tab. 3-1, [34]), equation (2.1) yields for the BVR:

$$\text{BVR} = \frac{V_{MSF}}{V_{YF}} = \frac{C_{SR}}{C_{SR} + C_{RF} + C_{B1} + C_{B2}} = \frac{0.1\,\text{nF}}{0.1\,\text{nF} + 1.1\,\text{nF} + 2 \cdot 0.1\,\text{nF}} = \frac{1}{14} \qquad (3.2)$$
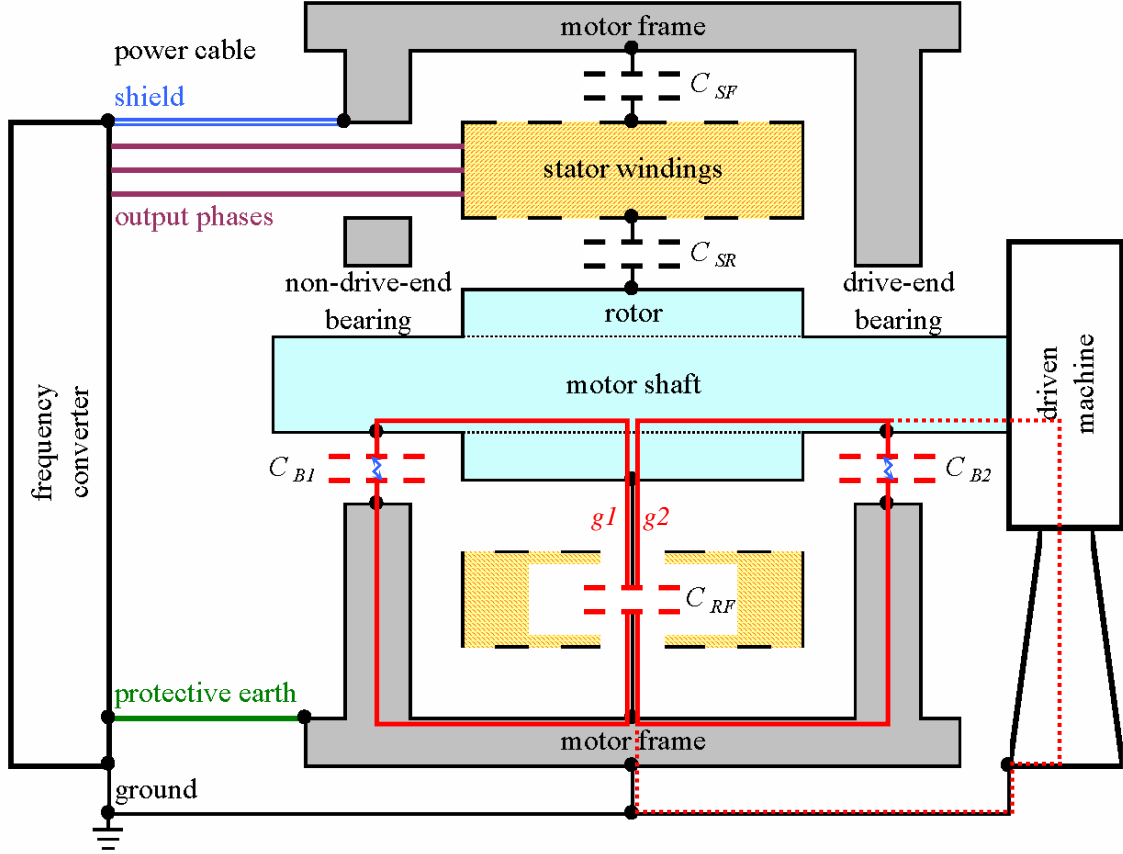

Fig. 3-5: Possible EDM-current loops (red solid lines) within a motor are drawn in the schematic diagram of a drive system as described in Fig. 3-1. Depending on the location of the EDM-process (blue spark), either in the non-drive-end bearing or the drive-end bearing, the main part of the EDM-energy is transferred along the path $g1$ or $g2$, respectively. The energy stored in C_{B1} and C_{B2} is much smaller than the energy available in C_{RF}, because the capacitances C_{B1} and C_{B2} are normally about ten times smaller than C_{RF} (Tab. 3-1). Therefore, a proportional smaller amount of energy is transferred (not shown) by the not affected bearing to that bearing, where the EDM-process happens. The red dotted line illustrates possible current passage through the bearings of the driven machine caused by V_{MSF}, if the loops $g1$ and $g2$ are broken due to the usage of hybrid bearings.

EDM-currents occur during EDM-processes, which start as soon as the electrical field strength at a finite region in one bearing of the motor reaches the breakdown threshold (chapter 2.3). During the EDM-process, the capacitances C_{RF}, C_{B1} and C_{B2} are discharged and the energy E_{EDM} (equation (2.3)) stored in these capacitances is transferred to the bearing, where it may cause damages. The larger portion of this energy is stored in the bigger capacitance C_{RF} (Tab. 3-1). An EDM-process happens in that bearing, in which the breakdown threshold of the electrical field strength is

attainted and, hence, through this bearing an EDM-current flows, which is mainly supplied by the capacitance C_{RF} (Fig. 3-5). In contrast to dv/dt-currents, which arise only during the switching operations of frequency converters, EDM-processes and, hence, EDM-currents can occur independently from the switching operation of frequency converters at any instant, when the breakdown threshold of the electrical field strength is reached. The insulation of both bearings in a motor, e.g., by using hybrid bearings, can reduce or eliminate EDM-currents in bearings, but the motor shaft-to-frame voltage will still exist, and may cause current passage (Fig. 3-5, dotted line) through the bearings in the driven machine, and, hence bearing damage. Therefore it is beneficial to attenuate or eliminate the motor shaft-to-frame voltage.

4   Test specimens and oil samples

Standard bearing balls and cylindrical rolling elements made of bearing-quality steel were used as test specimens for the test series in this work to ensure the same materials and surface conditions, as they are present in real bearings. Lubricants usually contain several additives to improve their tribological properties. To be able to investigate and compare the properties of different base oils, only pure base oils without additives and two special reference oils have been used.

4.1   Bearing balls and cylindrical rolling elements

Standard bearing balls and cylindrical rolling elements (Fig. 4-1) were provided by SKF Österreich AG, Development Centre Steyr [35]. The used bearing balls had a diameter of 10.319 mm and belonged to the precision class G10 with a tolerance of ±1 µm. The dimensions of the cylindrical rolling elements were 10 mm in length as well as in diameter.

Fig. 4-1:   Standard cylindrical rolling element and bearing ball provided by SKF Österreich AG, Development Centre Steyr.

4.2   Base oils and reference oils

Different base oils and two reference oils for the test series were provided by Klüber Lubrication München KG. Some chemical and physical properties, such as the kinematic viscosity, the permittivity and the mass density, of the base oils could be obtained from producer specifications (Tab. 4-1). The permittivity values of the reference oils were taken from literature [36].

number of oil sample	type of oil	kinematic viscosity		relative permittivity ε_r	density ρ at a temperature of	
		at 40 °C v_{40}	at 80 °C v_{80}			
base oils		[mm^2/s]	[mm^2/s]	[1]	[kg/m^3]	[°C]
214	polyglycol	120	32		996	25
215	polyglycol	70	22		1038	20
216	silicone	70	34	2.79	990	25
217	silicone	76	40	2.76	960	25
218	perfluor-polyether	100	21		1880	20
219	mineral, naphthenic	105	16	2.235	907	15
220	ester, polar	55	14			
221	ester	80	16		970	20
222	polyalfa-olefin	65	16		840	20
223	mineral, paraffinic	68	15	2.196	877	15
345	perfluor-polyether	28	7.6		1880	20
reference oils						
001	squalan C$_{30}$H$_{62}$			*1.9106 * at 100 °C*		
002	di-2-ethylhexyl-sebacat C$_{26}$H$_{50}$O$_4$		4.7	*4.01 * at 26 °C*	920	20

Tab. 4-1:   Chemical and physical properties of oil samples according to producer specifications. The permittivity values marked with (*) were taken from literature [36].

4.3   Selected physical properties of air

Some test series were undertaken with air instead of an oil sample, therefore, selected physical properties of air were necessary for the comparison of the results obtained from test series with air and different oil samples, respectively (Tab. 4-2) [36].

density ρ	at 100 kPa and 300 K	1.161 kg/m^3
dynamic viscosity η	at 100 kPa and 300 K	18.6 μPa·s
relative permittivity ε_r	for dry and CO$_2$ free air at 101.235 kPa and 20°C	1.0005364
kinematic viscosity ν $\nu = \eta / \rho$	at 100 kPa and 300 K	16.0207 mm^2/s

Tab. 4-2:   Selected physical properties of air [36]. The kinematic viscosity ν was calculated from the dynamic viscosity η and the density ρ.

5 Experimental equipment, measuring instruments and test procedures

5.1 Set-up for measurement of relative permittivity of oil samples

The permittivities of the oil samples were measured at the Austrian Center of Competence for Tribology (AC^2T), Wr. Neustadt [37]. Using a network analyser from Hewlett Packard (HP8753), the electrical admittance Y_{OS} of a special measuring cell formed by two coaxial hollow cylinders and filled with different oil samples was determined for the measuring frequency f_M in the range from 1 MHz to 10 MHz. If two coaxial hollow cylinders are filled with an electrically insulating medium, e.g. oil or air, the conductance (real part of the admittance) of this system will usually be very small in relation to the susceptance (imaginary part of the admittance) and, hence, can be neglected. Therefore the admittance Y_{OS} of the coaxial hollow cylinders filled with an oil sample can be calculated as:

$$Y_{OS} = G_{OS} + j\omega\varepsilon_{r,OS}C_C$$
$$Y_{OS} \simeq j\omega\varepsilon_{r,OS}C_C = j \cdot \text{Im}(Y_{OS}) \quad \text{if} \quad G_{OS} \ll \omega\varepsilon_{r,OS}C_C$$

(5.1)

Here G_{OS} is the conductance of the coaxial hollow cylinders filled with an oil sample, $\varepsilon_{r,OS}$ the permittivity of the insulating medium, C_C the capacitance of the measuring cell when filled with air, ω the angular frequency ($\omega = 2\pi f_M$) and j the imaginary unit. In any real measuring system, parasitic capacitances additionally exist, which are represented by the capacitance C_P:

$$\text{Im}(Y_{OS}) = \omega C_P + \omega\varepsilon_{r,OS}C_C$$

(5.2)

To calculate the parasitic capacitance C_P and the capacitance of the measuring cell C_C, and to calibrate the measuring system, two measurements with reference materials of known permittivity, e.g. air and cyclohexane, are necessary. From the measured admittances Y_A and Y_{CH} with air and cyclohexane, respectively, and with the corresponding permittivities $\varepsilon_{r,A} \simeq 1$ and $\varepsilon_{r,CH}$, the capacitances C_C and C_P can be derived according to A. Agoston et al. [37] as:

$$\omega C_C = \frac{\text{Im}(Y_{CH}) - \text{Im}(Y_A)}{\varepsilon_{r,CH} - \varepsilon_{r,A}}$$
$$\omega C_P = \text{Im}(Y_A) - \omega C_C$$

(5.3)

With equations (5.2) and (5.3) the relative permittivity of an oil sample $\varepsilon_{r,OS}(\omega)$ can be calculated from the measured admittance Y_{OS}:

$$\varepsilon_{r,OS}(\omega) = \frac{\text{Im}(Y_{OS}) - \omega\,C_P}{\omega\,C_C} = \frac{\text{Im}(Y_{OS}) - \text{Im}(Y_A)}{\text{Im}(Y_{CH}) - \text{Im}(Y_A)}\left(\varepsilon_{r,CH} - \varepsilon_{r,A}\right) + 1 \qquad (5.4)$$

5.2 Measurement of kinematic viscosity and mass density of oil samples

Using the viscosity meter SVM 3000 from Anton Paar GmbH, the kinematic viscosities and densities of the oil samples were measured at AC²T [38]. In contrast to usual viscosity meters, which normally determine the kinematic viscosity ν, the SVM 3000 uses a patented measuring principle (EP0926481A2) and measures the dynamic viscosity η and the density ρ of a liquid sample according to the standard ASTM D7042 [39]. Calculation of the kinematic viscosity $\nu = \eta / \rho$ from the dynamic viscosity η requires knowledge of the density ρ of the fluid. In the SVM 3000 the density of the sample is measured by use of the well-known oscillating U-pipe principle.

To measure the viscosity, the SVM 3000 comprises a pipe, which contains a rotor and the liquid sample. The pipe is rotated at constant rotational speed and, therefore, the fluid and the rotor in the liquid are also rotated due to the shear forces in the sample. The rotor contains a magnet, which generates eddy currents a copper shell around the pipe when rotated. The magnetic fields of the eddy currents retard the rotation of the rotor in the fluid. That means, the rotational speed of the rotor is determined by the shear forces of the liquid sample and the magnetic retardation. The dynamic viscosity is calculated from the rotational speed of the rotor, which is measured by means of a Hall-sensor.

5.3 Infrared transmission spectroscopy of oil samples

Infrared transmission spectra (IRTS) of the investigated oil samples were measured at AC²T with the FTIR (Fourier transformed infrared) spectrometer "Tensor 27" from Bruker Optik GmbH by means of a diamond ATR (attenuated total reflection) accessory from SensIR Technologies, whereby in this unit the IR beam is reflected once. In contrast to a cuvette system, the diamond ATR accessory allows to analyse very small amounts of oil samples, like those available from the EDM-test series performed in this work. However, due to the smaller amount of material available for analysis, this system is less sensitive than a cuvette system. Possible deteriorations of the oil samples due to EDM-processes should be investigated. Therefore, IRTS of new oil samples and

of oil samples, which had been affected by EDM-processes, were measured and compared.

5.4 Set-ups for determination of inherent stray capacitances in three-phase induction motors

The inherent stray capacitances C_{RF}, C_{SR}, C_{SF}, C_{B1} and C_{B2} (Fig. 3-1) existing in any three-phase induction motor have been described in chapter 3.1. The dominant stray capacitances for the generation of the motor shaft-to-frame voltage V_{MSF} are the capacitances C_{RF} and C_{SR}, which mainly determine the magnitude of V_{MSF} (equation (2.1) and Tab. 3.1). Measurements of these stray capacitances require the motor shaft to be electrically insulated from the motor frame either by insulating sleeves or by an insulating lubricant film in the bearings, which is formed when the bearings are operated in the full-film lubrication regime. In the second case, the rotational speed of the motor shaft must be high enough, so that electrically insulating continuous lubricant films will be developed in both bearings. In order not to interfere with the capacitance measurement, an electric drive of the motor has to be avoided for the determination of the stray capacitances. Therefore, the motor shaft can be rotated via a belt by another motor, to create the insulating lubricant films in the bearings of the investigated motor. Further, the shaft of the investigated motor must not be electrically connected to a driven machine, to prevent grounding of the motor shaft via the driven machine or additional capacitive coupling between the motor shaft and the frame of the driven machine.
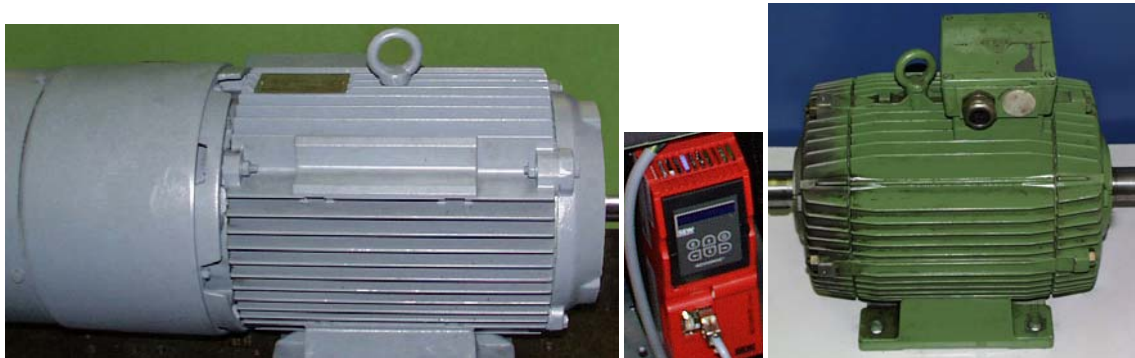

Fig. 5-1: Two test motors, available at SKF Österreich AG, Development Centre Steyr, were used: a grey coloured motor (left) from SEW-Eurodrive (DU160M2/TF/EV1S, 11 kW), controlled by a frequency converter (Movidrive MCV40A0110-5A3-4-00; middle), and a green coloured motor (right) from Elin (ÖVE-M10/80, 7.5 kW).

In this work, the stray capacitances of two three-phase induction motors have been measured (Fig. 5-1). Both motors were available at SKF Österreich AG, Development Centre Steyr, a green coloured motor from Elin (ÖVE-M10/80, 7.5 kW), in the

following named "green motor", and a grey coloured motor from SEW-Eurodrive (DU160M2/TF/EV1S, 11 kW), in the following named "grey motor". While the green motor was supplied with insulating sleeves, the shaft of the grey motor was rotated via a belt by another motor to create an insulating lubricant film in both bearings.

5.4.1 Measuring of the stray capacitance between the rotor and the motor frame

The capacitance C_{RF} of the green motor was measured by means of a standard hand-held LCR-meter (Voltcraft, 9063) connected between the (standing) motor shaft and the motor frame. The respective measurement at the grey motor had to be undertaken during the rotation of the motor shaft by another motor via a belt. Therefore, the LCR-meter was connected to the motor shaft via a rotating mercury contact MC. It should be pointed out that the capacitances C_{B1} and C_{B2} of the bearings are in parallel to C_{RF}, therefore the measurement results $C_{RF} + C_{B1} + C_{B2}$. The bearing capacitances can be neglected, because the capacitances fulfil the relations $C_{RF} \gg C_{B1}$ and $C_{RF} \gg C_{B2}$ (Tab. 3.1). Also in the following sections the bearing capacitances C_{B1} and C_{B2} are neglected.
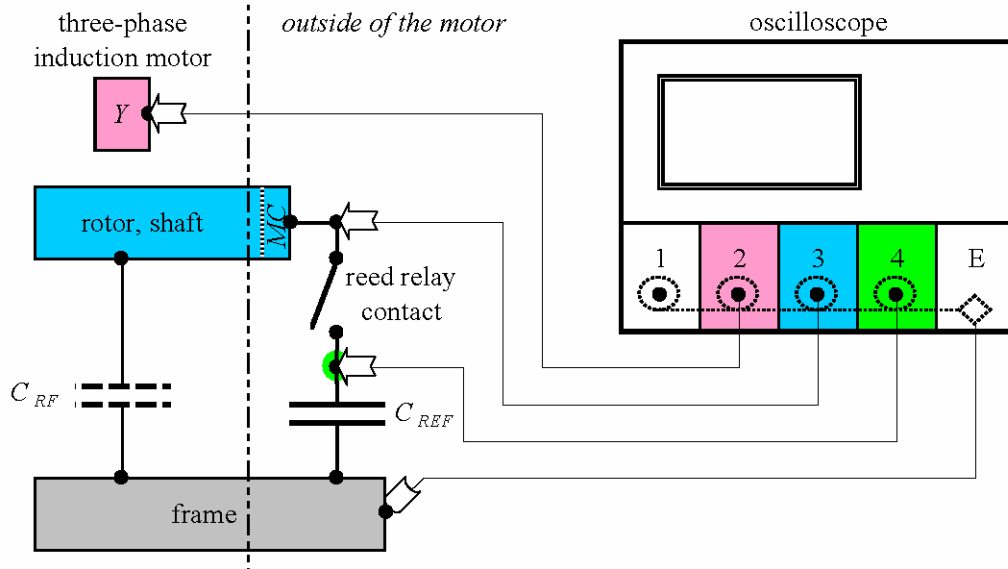

Fig. 5-2: Schematic diagram of the measuring set-up, to determine the stray capacitance C_{RF} by means of a reference capacitance C_{REF} connected to the motor frame and the motor shaft via a reed relay contact and a rotating mercury contact MC. The motor star point is labelled Y and the earth connection of the oscilloscope E. The voltage probes connected to the channels 2, 3 and 4 of the oscilloscope are represented by hollow arrows.

Another method, which allows to measure the stray capacitance C_{RF} during the operation of the motor, was applied at the grey motor by connecting a reference capacitance C_{REF} in parallel to the inherent capacitance C_{RF} between the motor shaft and

the motor frame via a reed relay contact in combination with the mercury contact (Fig. 5-2). If both bearings are in the full-film lubrication regime and no EDM-process occurs, the motor shaft-to-frame voltage keeps constant between two successive switching operations of the frequency converter. To detect these switching operations, a high-frequency multi-channel digital storage oscilloscope from LeCroy (WavePro 940) was used to monitor the star point-to-frame voltage as well as to measure the motor shaft-to-frame voltage measured for the determination of the capacitance C_{RF}. During the periods between the switching operations, the reference capacitance C_{REF} was switched in parallel to C_{RF} by closing the reed relay contact.

During each switching operation of the frequency converter the stray capacitances C_{SR} and C_{RF} (Fig. 5-3) are charged due to the *dv/dt*-currents, whereas during the periods between the switching operations these charges remain constant as long as no EDM-event happens. The addition of the (uncharged) capacitance C_{REF} in parallel to C_{RF} caused a decrease of the motor shaft-to-frame voltage V_{MSF} and a rise of the voltage V_{CREF} across C_{REF} until both voltages had reached the same level, because of the conservation of charge. That means, the total charge Q in the system comprising the capacitances C_{RF} and C_{REF} is constant. Before the closing of the reed relay contact the whole charge is contained in C_{RF}, but the charge is distributed among the capacitances C_{RF} and C_{REF} according to their capacitance values, when they are connected in parallel by the closed relay. The conservation of charge demands the voltages, $V_{MSF}(t_B)$ and $V_{MSF}(t_A)$, measured before and after the closing of the relay, and the corresponding capacitances C_{RF} and $C_{RF} + C_{REF}$, respectively, to fulfil equation (5.5).

$$V_{MSF}(t_B) \cdot C_{RF} = Q = V_{MSF}(t_A) \cdot (C_{RF} + C_{REF})$$

$$C_{RF} = C_{REF} \frac{V_{MSF}(t_A)}{V_{MSF}(t_B) - V_{MSF}(t_A)}$$

(5.5)

The unknown capacitance (C_{RF}) was calculated according to equation (5.5) from the value of C_{REF} and the values of the motor shaft-to-frame voltage $V_{MSF}(t_B)$ and $V_{MSF}(t_A)$, respectively, before and after the transient process that occurred when closing the reed relay contact. Here the same relations $C_{RF} \gg C_{B1}$ and $C_{RF} \gg C_{B2}$ were used, as described in the section before, hence the approximation $C_{RF} \cong C_{RF} + C_{B1} + C_{B2}$ was used.
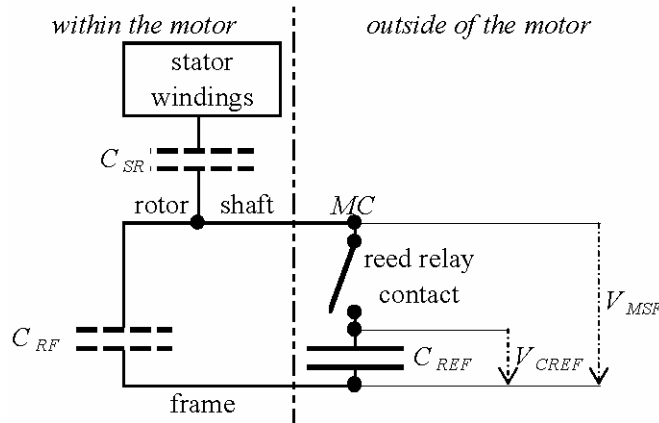
Fig. 5-3: Equivalent electric circuit of the measuring set-up shown in Fig. 5-2. To determine the stray capacitance C_{RF}, the voltage V_{CREF} across the reference capacitance C_{REF} and the motor shaft-to-frame voltage V_{MSF} are measured by an oscilloscope. The reference capacitance C_{REF} is connected to the motor frame and the motor shaft via a reed relay contact and a rotating mercury contact MC.
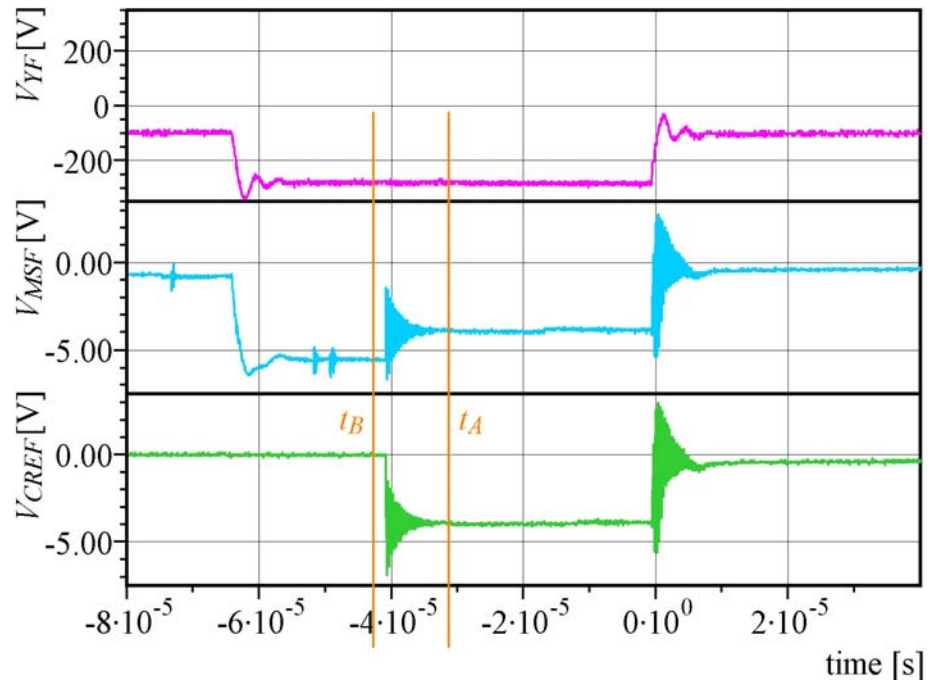

Fig. 5-4: Measurement of the star point-to-frame voltage (pink curve), the motor shaft-to-frame voltage (sky-blue curve) and the voltage across the reference capacitance C_{REF} (green curve) for the determination of the stray capacitance C_{RF} by means of the capacitance C_{REF} switched in parallel to C_{RF} by a reed relay contact. The reed relay contact was closed during a period (-55 µs and -5 µs) of constant star point-to-frame voltage. The capacitance C_{RF} was calculated according to equation (5.5) from the value of C_{REF} and the values of the motor shaft-to-frame voltage before (t_B) and after (t_A) the transient process that occurred when closing the reed relay contact.

5.4.2 Measuring of the stray capacitances between the stator windings and the rotor

A more sophisticated measuring set-up was needed for the measurement of the stray capacitances between the stator windings and the rotor. In usual three-phase induction motors at least one winding is available in the stator for each phase. The capacitance between the rotor and each end of each stator winding was measured separately, because the main part of the capacitive coupling, especially for higher frequencies, between the stator windings and the rotor is located at areas close to the ends of the windings. It is common knowledge, that damping of oscillating signals along windings increases with rising frequency.

In the terminal boxes of a usual motor normally seven terminals are available, two terminals for each of the three stator windings (W_1, W_2 and W_3), whereby one end of each stator winding is connected to one phase of the power supply and the other ends of the stator windings are wye-connected to the motor star point. The seventh terminal is provided for the PE-wire and is connected to the motor frame.
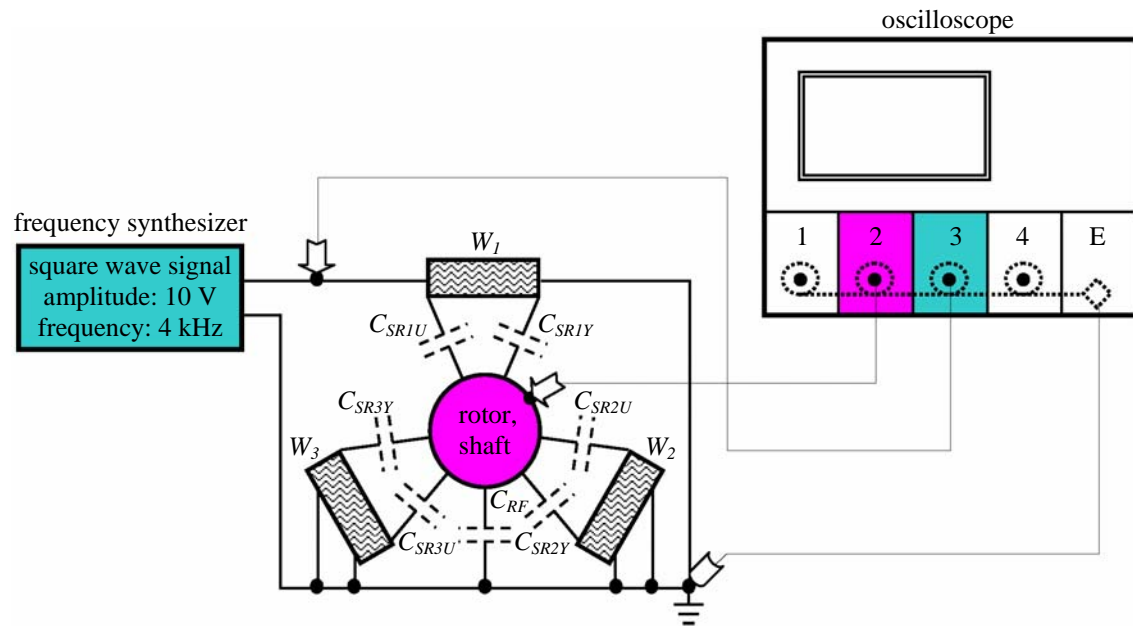
Fig. 5-5: Schematic diagram of the measuring set-up for the determination of the stray capacitances (C_{SF1U}, C_{SF1Y}, C_{SF2U}, C_{SF2Y}, C_{SF3U} and C_{SF3Y}) between each end of a stator winding (W_1, W_2 and W_3) and the rotor. The stray capacitance between the rotor and the frame is labelled C_{RF} and the earth connection of the oscilloscope E. The voltage probes connected to the channels 2 and 3 of the oscilloscope are represented by hollow arrows.

Fig. 5-6:   Schematic diagram of the measuring set-up for the determination of the total stray capacitances (C_{SF1}, C_{SF2} and C_{SF3}) between each stator winding (W_1, W_2 and W_3) and the rotor. The stray capacitance between the rotor and the frame is labelled C_{RF} and the earth connection of the oscilloscope E. The voltage probes connected to the channels 2 and 3 of the oscilloscope are represented by hollow arrows.
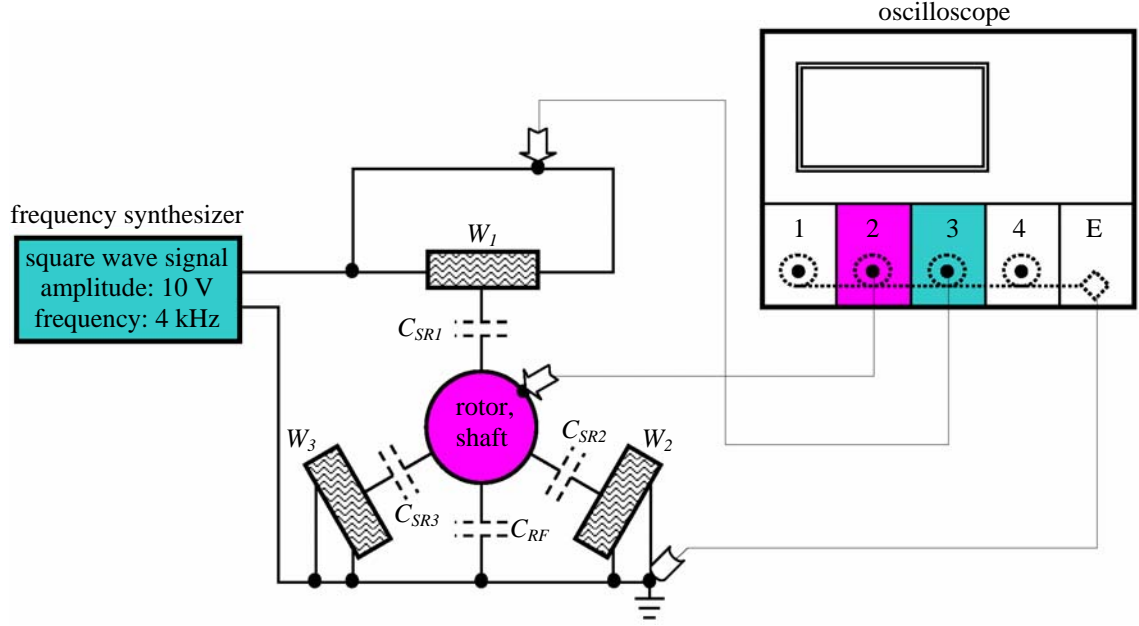
First of all, these connections were removed. Subsequently, one end of the first stator winding was connected to the output of a frequency synthesiser (HP33120A from Hewlett Packard), while the other end of this winding and both ends of all other stator windings were connected to the ground terminal of the frequency synthesiser (Fig. 5-5). A square wave signal V_{SW} with a frequency of 4 kHz and an amplitude of 10 V was applied to the stator winding connected to the synthesiser output. Using the oscilloscope, the signal at the stator winding and the signal V_{RF} capacitively coupled to the rotor were measured. The capacitive coupling at the second end of this stator winding and at both ends of the other windings was measured in the same way. Additionally, the total capacitive coupling between each stator winding and the rotor was measured. For that purpose, both ends of one stator winding were connected simultaneously to the output of the frequency synthesiser, while the ends of all other stator windings were grounded (Fig. 5-6).

The stray capacitances C_{SRE} (between one end of a stator winding or one stator winding and the rotor), C_{SRF} (sum of all stray capacitances between the rotor and that ends of the stator windings, which were connected to the motor frame) and C_{RF} (between the rotor and the motor frame) form a capacitive potential divider (Fig. 5-7). The capacitance C_{SRE} was calculated according to equation (5.6) by means of the peak to peak values of the signals V_{SW} and V_{RF}, and the value of the capacitance C_{RF} measured preliminarily

(chapter 5.4.1). Usually, C_{SRF} (a few tens of pF) can be neglected, because it is very small in relation to C_{RF} (a few nF).

$$\frac{V_{RF}}{V_{SW}} = \frac{C_{SRE}}{C_{SRE} + C_{RF} + C_{SRF}} \cong \frac{C_{SRE}}{C_{SRE} + C_{RF}} \rightarrow C_{SRE} = \frac{C_{RF}}{\frac{V_{SW}}{V_{RF}} - 1} \qquad (5.6)$$
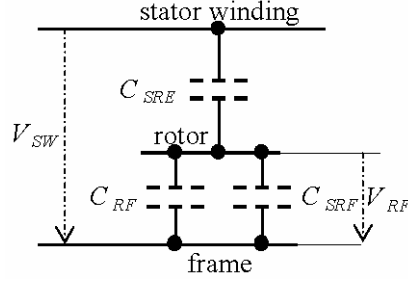

Fig. 5-7:   Schematic diagram of the capacitive potential divider formed by the stray capacitances C_{SRE} (between the stator winding and the rotor), C_{SRF} (the sum of all capacitances connected to the motor frame) and C_{RF} (between the rotor and the frame) and C_{RF} (between the rotor and the frame). The square wave signal V_{SW} is applied by the frequency synthesiser. The signals V_{SW} and V_{RF} (across C_{RF}) were measured by an oscilloscope.

5.5   Set-ups for investigation of the electrical regime of an induction motor driven by a frequency converter

The electrical regime of a drive system, available at SKF Österreich AG, Development Centre Steyr, was investigated, which comprised a frequency converter from SEW-Eurodrive (Movidrive MCV40A0110-5A3-4-00) and the "grey motor" characterised in chapter 5.4. Characteristic voltages and currents in this drive system, e.g. the star point-to-frame voltage, the motor shaft-to-frame voltage, the motor frame-to-ground voltage or voltages and currents in the PE-wire between the frequency converter and the driven motor, were monitored and measured by an oscilloscope (chapter 5.4). Quantitative knowledge of these voltages and currents is required for characterisation of the electrical regime of the drive system and for the calculation of important parameters, such as the capacitance and the resistance of an EDM-loop in an induction motor.

5.5.1   Measurement of the star point-to-frame voltage, the motor shaft-to-frame voltage and the phase voltages

The star point-to-frame voltage V_{YF} and the motor shaft-to-frame voltage V_{MSF}, respectively, were monitored or measured using an oscilloscope and connecting a high-voltage probe to the motor star point Y and a standard voltage probe to the motor

shaft via a mercury contact *MC*, which provided a good mechanical and electrical connection to the rotating motor shaft (Fig. 5-8).
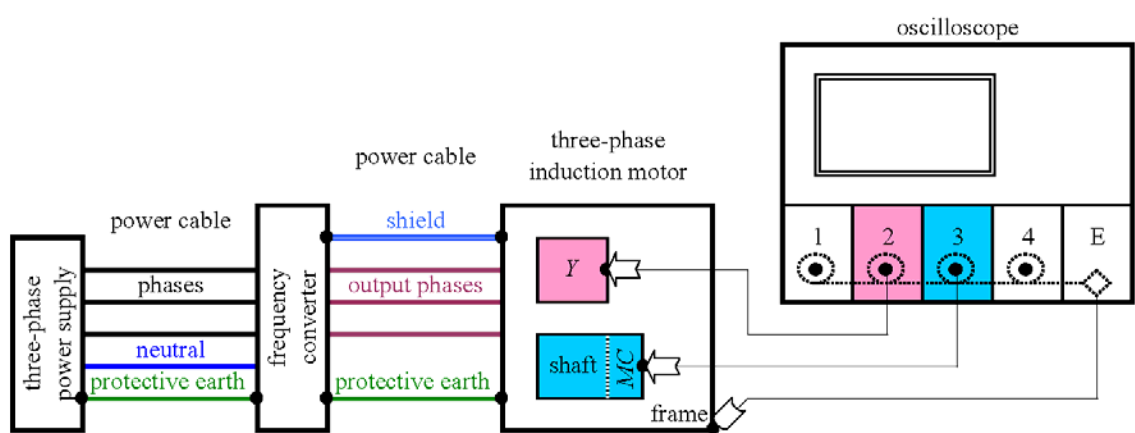

Fig. 5-8:   Schematic diagram for measurement of the star point-to-frame voltage (pink) and the motor shaft-to-frame voltage (sky-blue) at a three-phase induction motor driven by a frequency converter, whereby *Y* is the motor star point, *MC* the rotating mercury contact mounted at the motor shaft and *E* the earth connection of the oscilloscope. The voltage probes connected to the channels 2 and 3 of the oscilloscope are represented by hollow arrows.

Usually, the motor star point is accessible in the terminal box of an induction motor (chapter 5.4). The phase voltages (U_1, U_2 and U_3) applied by the frequency converter to the induction motor were measured by connecting high-voltage probes to the corresponding terminals in the terminal box of the motor. To ensure correct measurements, the oscilloscope was grounded only via the earth connection of the motor. Thus, the earth connection *E* of the oscilloscope was connected to the motor frame, which was electrically connected to the ground of the frequency converter by the PE-wire (protective earth) and the shield of the power cable.

5.5.2   Triggering on EDM-events

Switching operations of frequency converters happen periodically and can be monitored at the star point-to-frame voltage. However, the occurrence of EDM-processes does not necessarily depend on these switching operations. The motor shaft-to-frame voltage will change to a higher or a lower voltage level according to the corresponding changes of the star point-to-frame voltage as long as the bearings of the motor are in the full-film lubrication regime. But the motor shaft-to-frame voltage will break down immediately, if an EDM-process in one of the bearings happens. Using the feature "slew rate trigger" of the oscilloscope, EDM-processes were detected by triggering on the slew rates of the transients of the motor shaft-to-frame voltage due to the EDM-processes. These EDM-initiated slew rates were much higher than the slew rates caused at the motor shaft-to-frame voltage by the switching operations of the frequency converter. Positive

and negative voltage levels are possible at the star point-to-frame voltage as well as at the motor shaft-to-frame voltage. Therefore, negative and positive slopes at the motor shaft-to-frame voltage may occur, if the voltage breaks down due to EDM-processes. However, the feature "slew rate trigger" allows to trigger either on positive or negative slopes only.

5.5.3 Determination of the loop resistance of an EDM-loop

Not only the capacitance C_{RF} between the rotor and the frame in an induction motor but also the inherent resistance R_{LE} and inductance L_{LE} of an EDM-loop (Fig. 3-5) determine the time dependence of currents and voltages during EDM-processes in bearings (chapter 3.7). The capacitance C_{RF} was measured as described in chapter 5.4.1. The resistance R_{LE} and the inductance L_{LE} of the EDM-loop are not located at finite regions in the loop, but they are distributed along the whole EDM-loop. Therefore, they are not available for direct measurement. Here, neglection of the loop inductance L_{LE} was justified, because only very small oscillations in the time dependence of the motor shaft-to-frame voltage were observed (Fig. 5-9). Hence, the loop resistance R_{LE} could be calculated by means of the time constant τ as:

$$\tau = C_{RF} \cdot (R_{LE} + R_C)$$
$$\tau_S \approx C_{RF} \cdot R_{LE}$$

(5.7)
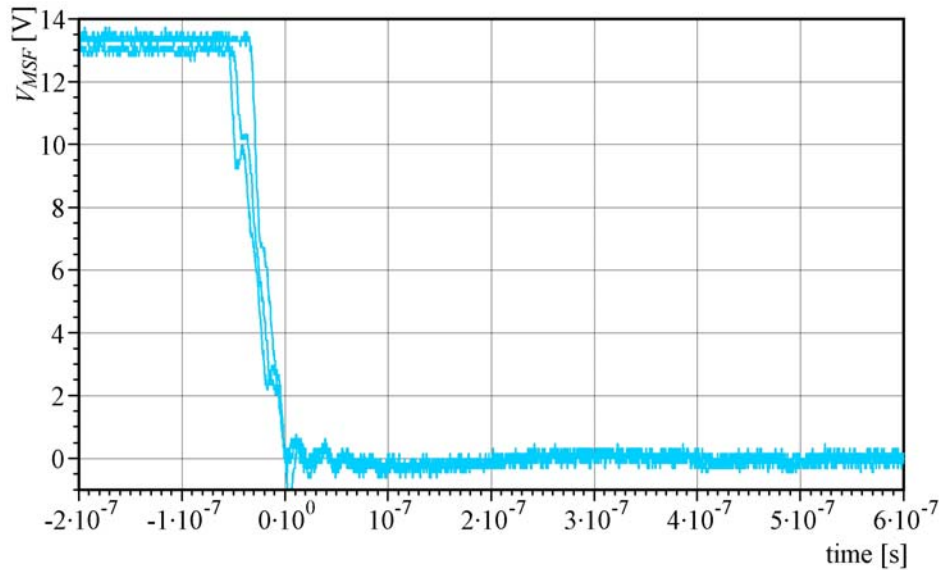
Fig. 5-9: Selected time dependence of the motor shaft-to-frame voltage V_{MSF} measured at the grey motor by the oscilloscope during EDM-events with the steepest slopes. Neglection of the loop inductance L_{LE} was justified, because only very small oscillations in the time dependence of the motor shaft-to-frame voltage were observed. The time constant τ is equal to the duration after that the voltage V_{MSF} is 1/e-times.

The values of the contact resistance fluctuate during each series of EDM-events. Therefore, the time constant was determined at the steepest slopes of the motor shaft-to-frame voltage during EDM-processes as triggered by the oscilloscope at the operated grey motor (Fig. 5-9). During these EDM-processes, the time constants τ_S are mainly determined by the constant loop resistance R_{LE}, because the contact resistance R_C is minimum and is small in relation to R_{LE}.

5.5.4   Measuring technique for EDM-currents

While the breakdowns at the motor shaft-to-frame voltage during EDM-processes can be measured with an oscilloscope as described, it is not possible to directly measure EDM-currents, because they flow inside the motor (Fig. 3-5). By means of a special measuring technique, EDM-currents could be measured indirectly and subsequently calculated. The capacitance C_{RF} and the resistance R_{LE}, respectively, symbolise the stray capacitance distributed between the stator windings and the rotor and the loop resistance, which is extended along the EDM-loop inside the motor (Fig. 5-10). Therefore, the point F is a fictive point and is not accessible for measurement. The externally connected measuring circuit, comprising the capacitor C_M and the resistor R_M, provides outside the motor the real point F^*, which is available for measurement. At F^* a voltage V_{F^*} can be picked up that shows the same time dependence as the voltage at F and, hence, allows to calculate the magnitude and the time progress of the current $I_{EDM}(t)$ in the EDM-loop inside the motor as:

$$I_{EDM}(t) = -V_{F^*}(t) / R_{LE} \tag{5.8}$$

The voltage probe at the point F^* is connected to the negative potential with respect to the capacitance C_M, therefore $-V_{F^*}$ is measured with the oscilloscope. This fact is included in equation (5.8) to calculate the correct EDM-current. As a prerequisite, the time constants of both loops, the internal EDM-loop and the external measuring circuit, have to be equal.

$$C_{RF} R_{LE} = \tau = C_M R_M \tag{5.9}$$

As soon as an EDM-event happens in one of the bearings, symbolised in the electric circuit by closing the switch S_C with the contact resistance R_C, both the EDM-loop and the measuring circuit are closed. The behaviour of the EDM-loop will basically not be affected by the external circuit, providing that the conditions $C_M \ll C_{RF}$ and $R_M \gg R_{LE}$ are fulfilled. The first condition ($C_M \ll C_{RF}$) ensures the capacitive potential divider

formed by C_{SR} and C_{RF} (Fig. 5-3) to be nearly not changed by connecting C_M in parallel to C_{RF}. The second condition ($R_M \gg R_{LE}$) provides the current in the external circuit to be very small in relation to the EDM-current inside the motor, so that the diminution of the EDM-current is negligibly. Further, must be ensured that measurements are undertaken only during EDM-events, which are not disturbed by switching operations of the frequency converter. Therefore, the star point-to-frame voltage has to be monitored simultaneously. To obtain correct measurement results, the same grounding as described in chapter 5.5.1 is necessary.
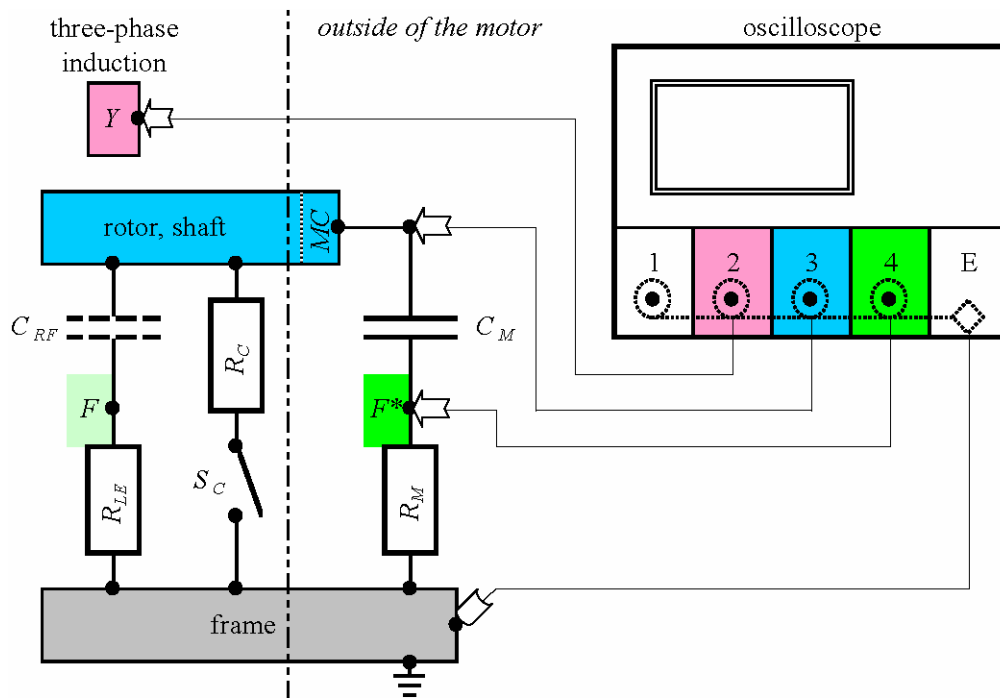

Fig. 5-10: Schematic diagram of the set-up for measuring EDM-currents. The EDM-loop consists of the stray capacitance C_{RF} between the rotor and the frame, the loop resistance R_{LE} extended along the EDM-loop and the (temporary) contact in the bearing described by the contact resistance R_C and switch S_C. The measuring circuit comprises the external capacitor C_M and resistor R_M and also the contact in the bearing. If the time constants of both loops are equal, the time dependence of the voltage measured at point F^* will be equal to that at the fictive point F. The motor star point is labelled Y, the rotating mercury contact MC and the earth connection of the oscilloscope E. The voltage probes connected to the channels 2, 3 and 4 of the oscilloscope are represented by hollow arrows.

5.5.5 Measurement of currents in the PE-wire and the shield and of the motor frame-to-ground voltage

In many drive systems the frames of frequency converters and driven motors are not only interconnected by PE-wires and sometimes by additional shields in the power cables, but they are also connected individually to a common ground. To correctly measure currents in the PE-wire or the shield of the power cable between a frequency converter and a driven motor, currents along other possible paths must be avoided.

Therefore, the investigated drive system was modified. The grey motor (chapter 5.4) was mounted electrically insulated from ground and the shielded control line between frequency converter and the tachometer was disconnected, that is, the drive system was operated in a mode without tachometer (Fig. 5-11). Currents in the PE-wire and the shield of the power cable between the frequency converter and the motor were measured with the oscilloscope by means of a current probe (LeCroy, AP015, DC - 50 MHz). Measurement of the motor frame-to-ground voltage required the motor to be electrically insulated from ground and the earth connection E of the oscilloscope being connected to the frame of the frequency converter (Fig. 5-11). Further, the star point-to-ground voltage was monitored to study possible coincidences between the switching operations of the frequency converter and peaks at the currents in the PE-wire and shield or at the motor frame-to-ground voltage.
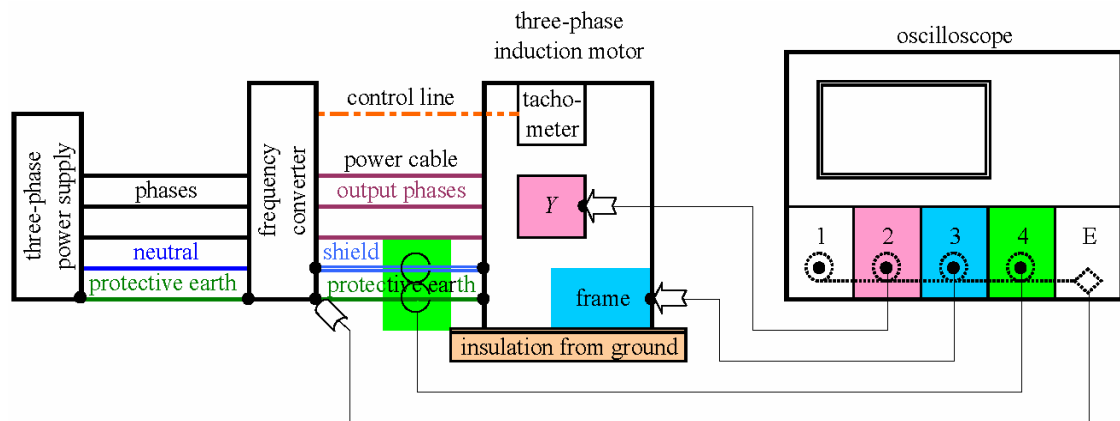
Fig. 5-11:   Schematic diagram of the measuring set-up enabling the measurement of currents in the shield and the PE-wire of the power cable between a frequency converter and a motor, and of the motor frame-to-ground voltage. Y is the motor star point and E the earth connection of the oscilloscope. Voltage probes, represented by hollow arrows, and a current probe, illustrated as an open circle, are connected to the channels 2, 3 and 4 of the oscilloscope.

5.6   Generation of EDM-processes with defined energy in a static test rig

Rolling bearings contain multiple rolling elements. From the electrical point of view, this means that many paths are available for a current to flow through a bearing, because the current may flow through any of the rolling elements. Further, it must be taken into account that such an electric current must pass two lubricant films, which exist between the inner ring and the outer ring, respectively, and the rolling elements. Additionally, nearly all components of a bearing are in motion during operation and so the raceways of all components may be damaged by electric current passage. In this work, a static test rig was designed and constructed to be able to initiate EDM-processes of defined energies at finite regions of test specimens and generate damages on the

surfaces of the test specimens. Standard bearing balls and cylindrical rolling elements (chapter 4) made of bearing-quality steel were used as test specimens to ensure the same materials and surface conditions, as they are present in real bearings. Different oil samples (chapter 4) were inserted into the gap between the test specimens, to be able to investigate the influence of these oils on the initiated EDM-processes, on the damages generated at the surfaces of the test specimens and on the deterioration of the oils.

5.6.1   Mechanical part of the static test rig

The mechanical part of the developed static test rig (Fig. 5-12 and appendix: engineering drawings of the static test rig) was constructed at SKF Österreich AG, Development Centre Steyr and comprises an X-Y-translational stage, two insulating plates, an upper and a lower holding device for a bearing ball and several cylindrical rolling elements, respectively, a linear Z-stage with a micrometer screw (TB 80-25 from Linos Photonics) and a piezo actuator (PV-10/80 from Linos Photonics) attached to the Z-stage. The holding devices were electrically insulated by plastic plates from the positioning systems and also from each other, to ensure that each holding device may separately be connected to the positive or negative terminal (*A*, *B*) of the electronic part of the static test rig. The cylindrical rolling elements were installed vertically in the lower holding device, i.e. their axes were perpendicular to the horizontal (X-Y) plane and their front surfaces were facing the bearing ball.

After each series of EDM-processes initiated between a single bearing ball and different points at the cylinder surfaces, these measuring points at the surfaces (also on the ball) had to be retrieved for subsequent analysis. Therefore, the measuring points at the surfaces of the cylindrical rolling elements were arranged according to a virtual grid with a spacing of 2 mm x 2 mm (Fig. 5-13). The position of the grid in relation to the surface of each cylindrical rolling element was indicated by two marks, which were also located at points of the virtual grid (Fig. 5-13). The positions of the marks and the measuring points, respectively, at the front surface of the investigated cylinder were adjusted by the X-Y-stage in relation to the bearing ball that was centrically fixed in the upper holding device.

The vertical distance between the bearing ball and the front surface of the cylindrical rolling element under test was adjusted in two steps. First, the gap was roughly reduced with the micrometer screw of the linear Z-stage and subsequently the fine adjustment of the vertical distance was controlled by an adjustable offset voltage, which was supplied by a frequency synthesiser (HP33120A from Hewlett Packard) and applied to the piezo

actuator at the micrometer screw via its control unit (Torque-Drive TD 1-200 from Linos Photonics). During the experiments the vertical oscillation of the upper holding device with the bearing ball was controlled by a sine wave signal generated by the frequency synthesiser and applied to the piezo actuator via the control unit.
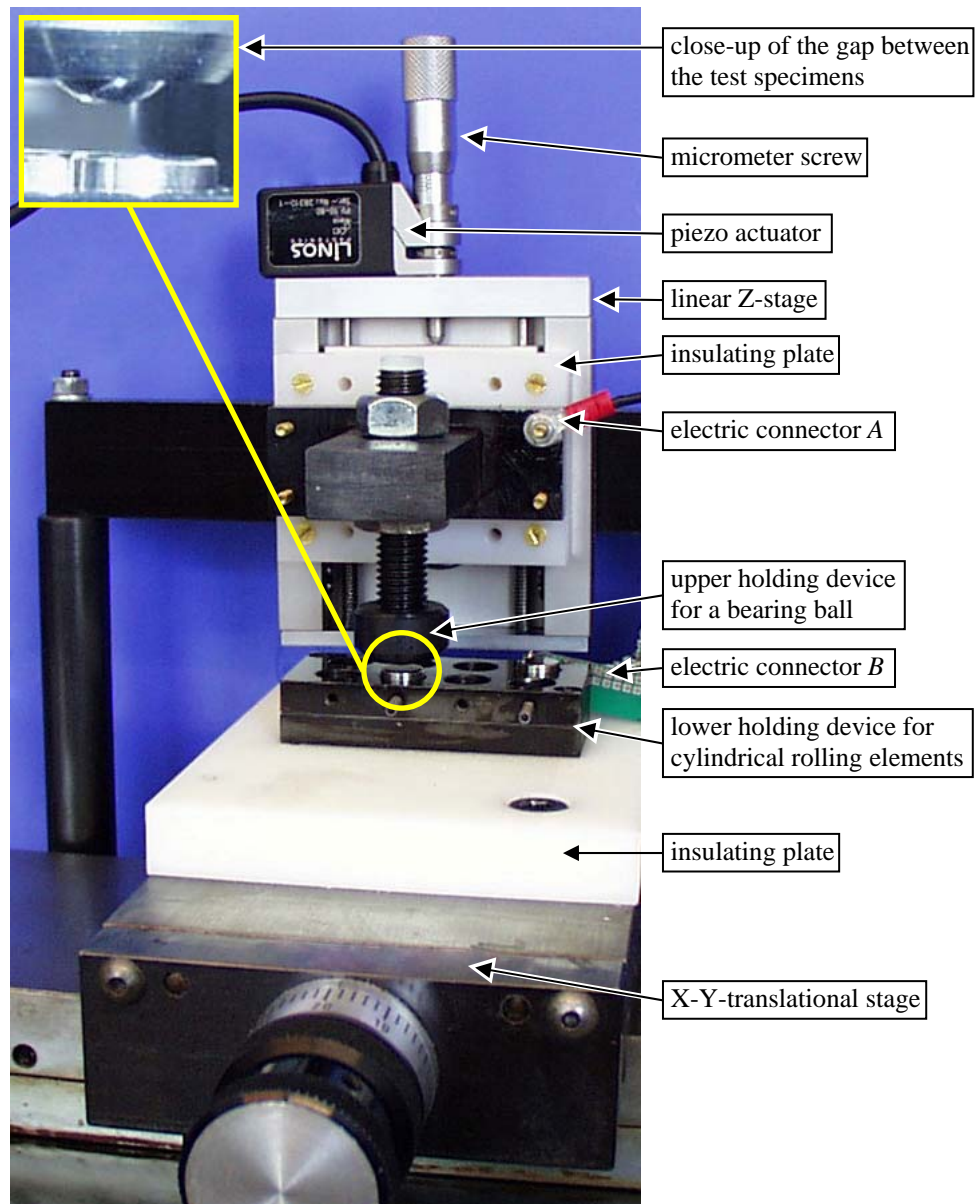

Fig. 5-12: Mechanical part of the static test rig for investigation of EDM-processes. The close-up in the upper left corner shows the gap between a bearing ball and a cylindrical rolling element fixed in the upper and the lower holding device, respectively. The static test rig is placed on a pneumatic shock absorber system to prevent mechanical vibrations and disturbances of the environment.

This static test rig has turned out to be very sensitive to mechanical vibrations and disturbances from the environment. Therefore, it was necessary to place the test rig on a pneumatic shock absorber system available at the Institut für Allgemeine Physik, TU Wien. This pneumatic shock absorber system comprised a heavy stone table mounted

on three stands with air-cushions supplied by compressed air and balanced by a control system.
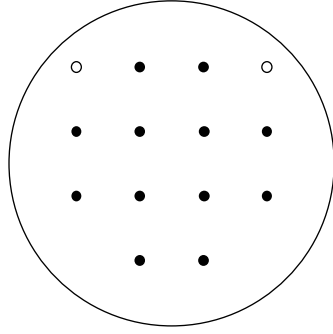

Fig. 5-13: Virtual grid (spacing: 2 mm x 2 mm) on the front surface of a cylindrical rolling element (Ø 10 mm). The open and full circles in the diagram depict the positioning marks and the measuring points, respectively.

5.6.2 Electronic part of the static test rig

The electronic part of the static test rig was designed to reproduce the EDM-loop of a typical three-phase induction motor (Fig. 5-14). Therefore, corresponding values were chosen for the capacitor C_S (2.5 nF) and the resistor R_S (5.8 Ω) of the designed EDM-circuit (depicted in red) according to the values C_{RF} and R_{LE} measured at the grey motor (chapter 5.4.1 and 5.5.3). The electrical and the mechanical part of the static test rig were electrically connected via the terminals A and B (Fig. 5-12 and Fig. 5-14) for contacting the bearing ball (*BB*) and the cylindrical rolling elements (*CRE*), respectively. An adjustable DC voltage source (DC-Konstanter 11 from Siemens) supplied the EDM-circuit via a limiting resistor R_I (24 kΩ). This resistance ensured that the additional current supplied by the DC voltage source to the test specimens during an EDM-event was negligible in relation to the current supplied by the capacitor C_S. Further, it prevented the DC voltage source from being short-circuited during an EDM-process. To create nearly realistic conditions in the test rig a voltage of 12 V was applied to the EDM-circuit by the adjustable DC voltage source.

The charging process of the capacitance C_S by the DC voltage source is determined by the time constant $\tau_C = C_S \cdot (R_I + R_S)$, whereas the discharge of C_S during an EDM-event depends on the time constant $\tau_D = C_S \cdot R_S$ and on the transition resistance between the test specimens during the EDM-process. Hence, the capacitance C_S was practically not recharged by the DC voltage source during an EDM-event, because the condition $\tau_C \gg \tau_D$ was fulfilled. The time dependences of the voltages $V_{RS}(t)$ and $V_{TS}(t)$ across the resistor R_S and the gap between the test specimens, respectively, during the EDM-processes were measured with the oscilloscope (Fig. 5-14).
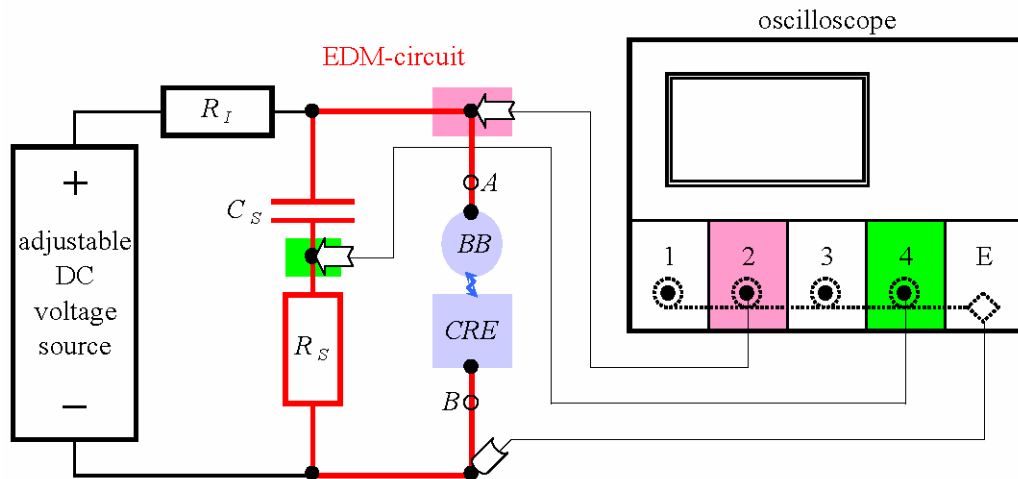
Fig. 5-14: Schematic diagram of the electronic part of the static test rig for investigation of EDM-processes. The EDM-circuit (depicted in red) for the generation of EDM-events comprises the capacitor C_S and the resistor R_S, which reproduce the EDM-loop existing in three-phase induction motors. During an EDM-process, that is a spark formation (depicted in blue) and current flow between the bearing ball *BB* and the cylindrical rolling element *CRE*, the current is supplied by the charged capacitor C_S and limited by the resistor R_S. The capacitor is permanently recharged by the DC voltage source connected via a limiting resistor R_I. The bearing ball and the cylindrical rolling element belong to the EDM-circuit as well as to the mechanical part of the test rig. The circuit is connected to the mechanical part via the terminals *A* and *B*. *E* is the earth connection of the oscilloscope. Voltage probes, represented by hollow arrows, are connected to the channels 2 and 4 of the oscilloscope.

5.6.3 Measuring procedure

New pairs of test specimens (bearing balls and cylindrical rolling elements) were used with each different oil sample for all measurement series. After cleaned with acetone, the cylindrical rolling elements were mounted at the lower holding device in the static test rig. Using a setting gauge and the X-Y-stage, one of the cylindrical rolling elements was arranged in a horizontal plane so that the (extended) vertical axis of the opposite bearing ball (only used for the generation of positioning marks) cut the cylinder surface at one of the fictive positioning marks on the virtual grid (Fig. 5-13). By means of initiated EDM current pulses, this position was branded on the surface of the cylinder. This procedure was repeated for the second positioning mark.

Subsequently, a new and cleaned bearing ball was centrically fixed in the upper holding device. Further, the cylindrical rolling element was horizontally positioned according to the first measuring point on the virtual grid, a small amount of an oil sample was placed on the surface of the cylinder and the distance between the test specimens was roughly reduced with the micrometer screw of the linear Z-stage. The vertical oscillation of the bearing ball was activated and controlled by a sine wave signal applied to the piezo actuator via the control unit. Thereafter, the distance between the bearing ball and the

cylindrical rolling element was fine adjusted by applying a DC offset voltage to the control unit of the piezo actuator. The distance was reduced until EDM-events could be registered. The time progress of the voltages V_{RS} and V_{TS} across the resistor R_S and the gap between the test specimens, respectively, were measured by the oscilloscope, whereas it was triggered on the falling edge of V_{TS}. The number of EDM-processes was counted by means of the "analog persistence" function of the oscilloscope. After each series of EDM-events, the vertical oscillation of the bearing ball was stopped and the distance between the test specimens was enlarged. Further, the cylinder was horizontally shifted to another measuring position by means of the X-Y-translational stage. Without replacing the oil sample, test series were carried out in the same way at the next measuring point after preliminary adjustment of the gap between the test specimens. The similar measuring procedure was executed using another oil sample, whereas a new pair of test specimens (bearing balls and cylindrical rolling elements) was mounted in the test rig.

Test series were undertaken at room temperature as well as at 80 °C. By means of a temperature sensor (PT 100), a ring heater (K-ring heating unit KKR40018001A from Thermoprozess), and a temperature controller (PXZ4 from Coulton Instrumentation LTD), the test specimens and the oil sample in the gap between the bearing ball and the cylindrical rolling element could be heated up and the temperature could be stabilised, if a test series was carried out at 80 °C.

5.7 Analysis of damages at the surfaces of test specimens due to EDM-processes

To study the generated damages at the measuring points on the surfaces of the test specimens, the structure of finite regions around the measuring points affected by EDM-processes in the stationary rig was analysed with a contactless optical profile meter ("µScan" from NanoFocus) available at AC^{2}T. The "µScan" uses white light and is based on confocal multi-pinhole technique. All test specimens analysed with the "µScan" were previously cleaned for 10 minutes in an ultrasonic bath using ethanol. Usually, the front surfaces of the cylindrical rolling elements were not exactly coplanar with respect to the optical plane of the "µScan". Therefore, the results of the analyses undertaken with the "µScan" were subsequently parallelised using implemented software, because only the structure of the surface but not the position of the surface in relation to the measuring system was important for investigation. The possible existence of cavities or elevations at the surfaces of the bearing balls as a consequence of the EDM-processes should be studied. Thus, with the available software, the calotte of the

bearing ball was subtracted from the raw data to visualise the structural changes at the surface in relation to the undisturbed (ideal) surface of the bearing ball.

5.8   Set-up for photographic documentation of EDM-events

The appearance of sparks between the test specimens during the excitation of EDM-processes in the static test rig should be documented by pictures. Visible sparks could be generated with the static test rig in air (no oil between the test specimens) using a DC voltage of 120 V between the test specimens, contrary to the voltage of 12 V applied during the test series. The sparks were photographed with a monochrome high speed digital camera ("i-speed camera" from Olympus) mounted at a tripod. To be able to use the maximum frame speed (33000 pictures per second) of the camera, the object had to be illuminated by spot lights. However, under these conditions the light of the sparks was outshone by the spot lights. Therefore, a much lower frame speed (100 pictures per second) had to be chosen, because in this case it was possible to take photographs at daylight (sunshine) and to catch photographically some sparks being in most instances brighter than the surrounding light.

6   Results

6.1   Relative permittivity of oil samples

By means of the method described in chapter 5.1, the relative permittivities (ε_r) of the oil samples were measured at room temperature and at 80 °C, because at these temperatures EDM test series were undertaken with the static test rig using samples of the same oils. As expected, at room temperature the permittivities of nearly all oil samples, except for the samples 220 and 221, are essentially constant over the frequency range from 1 MHz to 10 MHz (Fig. 6-1). In contrast, a larger and a smaller decrease of the permittivity values could be noticed for the polar ester (220) and the ester (221), respectively, in the considered frequency range. Additional investigations of this behaviour would be necessary to clarify, whether these effects depend of the chemical constitution of theses esters, on their polarity, their interaction with the electrodes of the measuring device (hollow cylinders) or on other reasons.
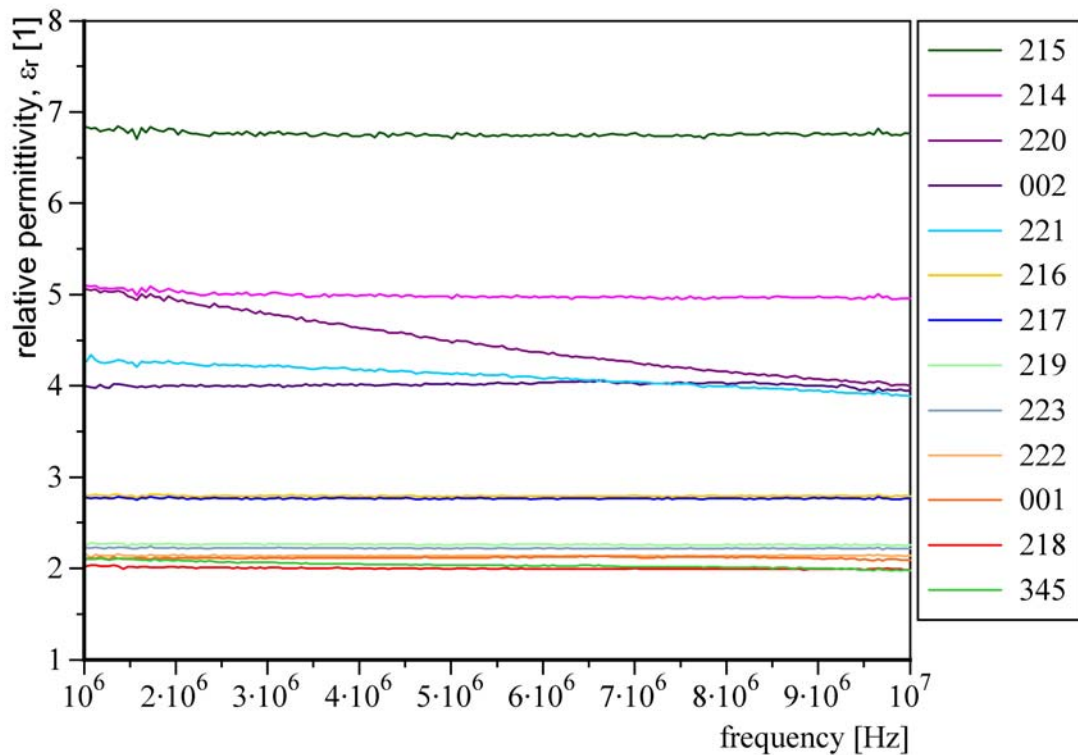

Fig. 6-1:   Relative permittivities (ε_r) over frequency of oil samples at room temperature. Samples are labelled by numbers according to Tab. 4-1 in chapter 4.2.

A slight decrease with increasing frequency of the permittivity can be seen for all investigated oil samples at a temperature of 80 °C (Fig. 6-2). Generally, the permittivities of the mineral oils (219, 223), polyalfa-olefin (222), perfluor-polyether

(218, 345) and squalan (001) are in the range from 2 to 2.8, of the silicon oils in the range from 2.8 to 3.2, of di-2-ethylhexyl-sebacat and ester (002, 221) in the range from 3.6 to 4.4, of one polyglycol (214) in the range from 4.6 to 5.4 and of the other polyglycol (215) in the range from 5.9 to 6.7. The permittivity values specified by oil producers of 2.79 (oil 216), 2.76 (oil 217), 2.235 (oil 219), 2.196 (oil 223) and 4.01 (oil 002) match very well with the measured results (compare Tab. 4-1 and Fig. 6-1).
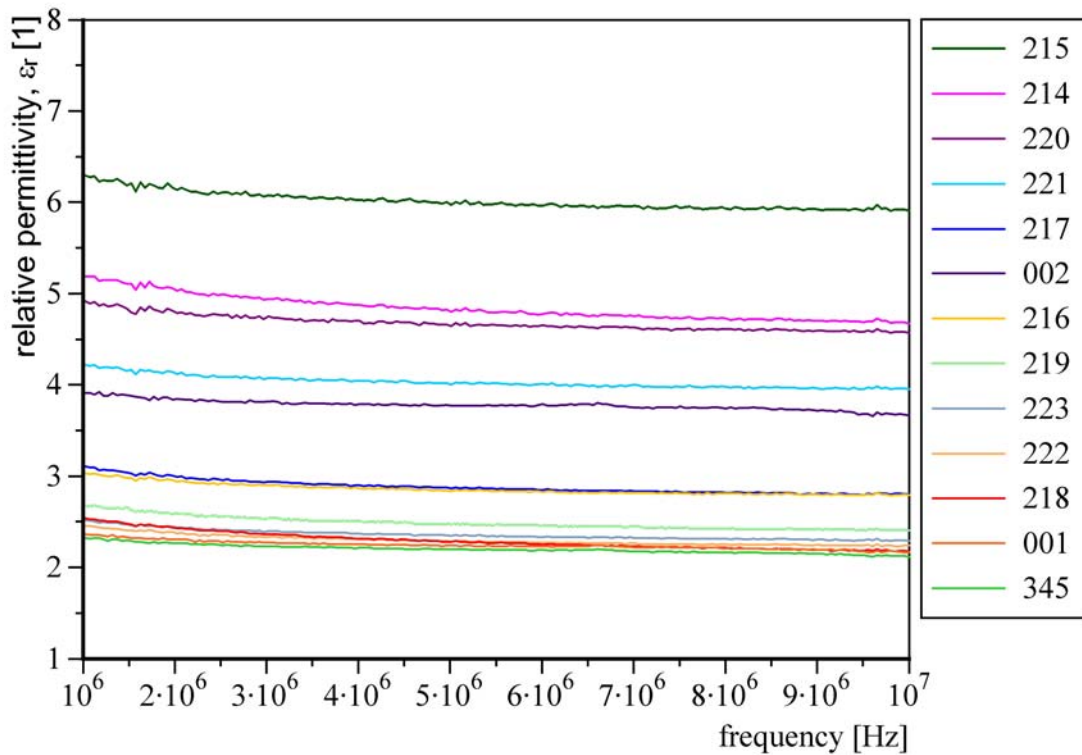

Fig. 6-2:   Relative permittivities (ε_r) over frequency of oil samples at 80 °C. Samples are labelled by numbers according to Tab. 4-1 in chapter 4.2.

6.2   Kinematic viscosity and mass density of oil samples

At room temperature and at temperatures of 80 °C, 40 °C and 100 °C, the kinematic viscosities (ν) and the mass densities (ρ) of the oil samples were measured with the SMV 3000 (chapter 5.2), because at the first two temperatures the EDM test series were carried out with the static test rig and the last two temperatures (40 °C and 100 °C) are standard temperatures for the measurement and specification of viscosities. The values of the kinematic viscosities and the mass densities available from oil producers for some oil samples are listed in Tab. 6-1 for comparison with the values measured by the SMV 3000. These values match very well. In Fig. 6-3 and Fig. 6-4, respectively, the values of the mass densities and the kinematic viscosities for all oil samples measured with the SMV 3000 are shown. In contrast to the perfluor-polyethers (218, 345) which

have considerably higher mass densities (between 1730 kg/m^3 and 1900 kg/m^3), the mass densities of all other oil samples are in the range from 750 kg/m^3 to 1040 kg/m^3. The oil samples were selected in such a way, that their kinematic viscosities are spread over a wide range. At room temperature di-2-ethylhexyl-sebacat (002) and naphthenic mineral oil (219), respectively, offered the smallest (20.9 mm^2/s) and the highest (343.5 mm^2/s) kinematic viscosity. The mass densities of the oil samples decrease only slightly with rising temperature, but their kinematic viscosities fall dramatically in the same temperature range (Fig. 6-3 and Fig. 6-4).

temperature	23 °C			40 °C		80 °C		100 °C	
oil sample	ρ [kg/m^3]	temp.	ρ [kg/m^3]	ν [mm^2/s]	ν [mm^2/s]	ν [mm^2/s]	ν [mm^2/s]	ν [mm^2/s]	ν [mm^2/s]
214	991.8	25 °C	996	127.0300	120	34.8280	32	22.3330	
215	1036.1	20 °C	1038	73.0590	70	22.5940	22	15.0290	
216	996.5	25 °C	990	70.5950	70	35.4210	34	26.2840	
217	964.7	25 °C	960	79.1450	76	42.7850	40	33.2830	
218	1892.1	20 °C	1880	101.2000	100	21.5500	21	12.4530	
219	901.4	15 °C	907	99.4140	105	15.3940	16	8.4566	
220	1003.7			52.7260	55	14.0430	14	8.7545	
221	959.6	20 °C	970	73.5140	80	16.6040	16	9.8853	
222	829.6	20 °C	840	61.1120	65	15.4110	16	9.4221	
223	871.0	15 °C	877	67.4570	68	14.6370	15	8.6990	
001	806.6			19.1520		6.1546		4.1458	
002	911.6	20 °C	920	11.7140		4.5534	4.7	3.2509	
345	1872.3	20 °C	1880	27.8440	28	7.5360	7.6	4.7268	4.8

Tab. 6-1:   Mass densities (ρ) and kinematic viscosities (ν) of oil samples for selected temperatures. The blue printed values were measured at AC^{2}T with the SVM 3000 and the orange coloured values were specified by oil producers. Samples are labelled by numbers according to Tab. 4-1 in chapter 4.2.
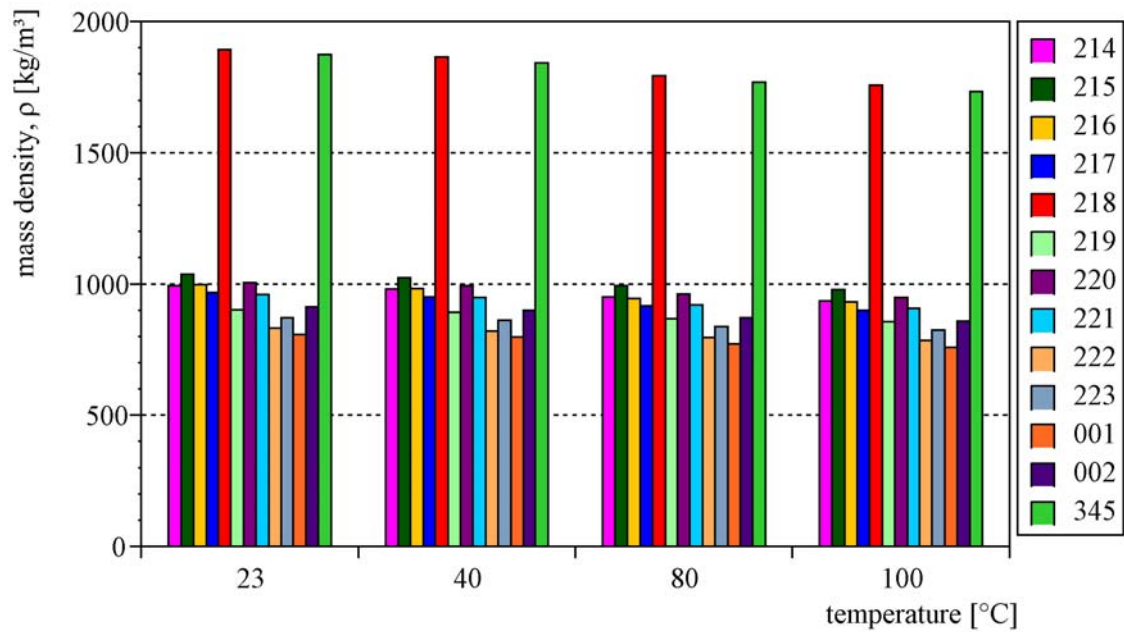
Fig. 6-3:   Mass densities (ρ) of oil samples for selected temperatures measured with the SMV 3000. Samples are labelled by numbers according to Tab. 4-1 in chapter 4.2.

Fig. 6-4:   Kinematic viscosities (ν) of oil samples for selected temperatures measured with the SMV 3000. Samples are labelled by numbers according to Tab. 4-1 in chapter 4.2.
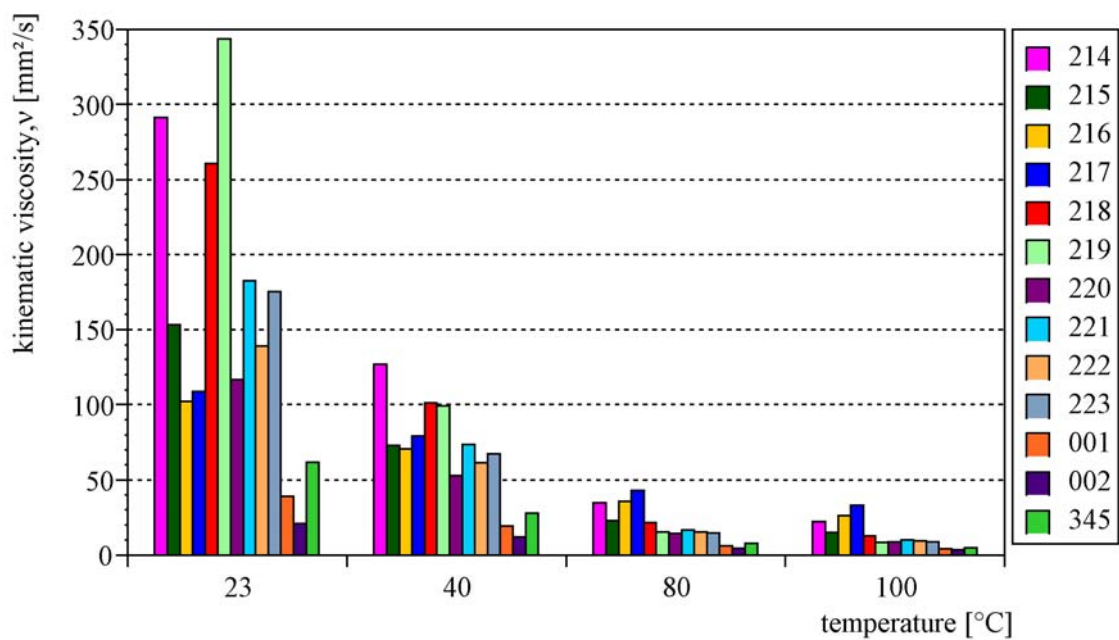
6.3   Infrared transmission spectra of oil samples

Infrared transmission spectra (IRTS) of the oil samples were analysed by means of the equipment described in chapter 5.3. To verify the IRTS of the reference oils (001 and 002) measured with ATR (attenuated total reflection), they were compared with results from Klüber Lubrication München, where the measurements of the IRTS were undertaken with a cuvette. Comparison of these results showed that the peaks at the curves (depicted in red) measured with ATR were clearly smaller than the peaks at the curves (depicted in blue) measured with a cuvette, but corresponding peaks in the IRTS of both reference oils were found at the same wave numbers (Fig. 6-5 and Fig. 6-6). Additionally, IRTS were measured for all other oil samples (Fig. 6-7 to Fig. 6-12) before treatment by EDM-processes in the static test rig. In these spectra, important peaks characterising the oil samples are labelled. The wave number σ_{IR} at the abscissas of the diagrams depends on the wave length λ_{IR} (or the frequency f_{IR}) of the infrared wave (equation (6.1)). In IRTS the wave number $\sigma_{IR}[1/cm]$ is traditionally not indicated in SI-units, therefore also a conversion formula is given in equation (6.1), whereby SI-units are used for all other quantities ($\sigma_{IR}[1/m]$, $\lambda_{IR}[m]$, $f_{IR}[Hz]$ and $c[m/s]$, the velocity of light).

$$\sigma_{IR} = \frac{1}{\lambda_{IR}} = \frac{f_{IR}}{c} \longrightarrow \sigma_{IR}[1/cm] = \frac{\sigma_{IR}}{100} = \frac{1}{100\lambda_{IR}} = \frac{f_{IR}}{100c} \qquad (6.1)$$

To check the sensitivity of IRTS on the deterioration of oil samples due to EDM-processes initiated in the static test rig, spectra of stressed and unstressed reference oils were compared. Reference oils were used for these tests because it was expected that changes in the IRTS could be observed more clearly for the pure reference oils than for other oil samples. Different series of EDM-processes were carried out in the static test rig applying a DC voltage of 120 V (approximately 3000 and 32000 EDM-events) and 12 V (approximately 32000 EDM-events) across the gap between the test specimens. However, the IRTS of fresh reference oils and of reference oils stressed by EDM-processes did not show any significant differences (Fig. 6-13 and Fig. 6-14), although a distinct change in the colour of the stressed oils could be observed (Fig. 6-15).
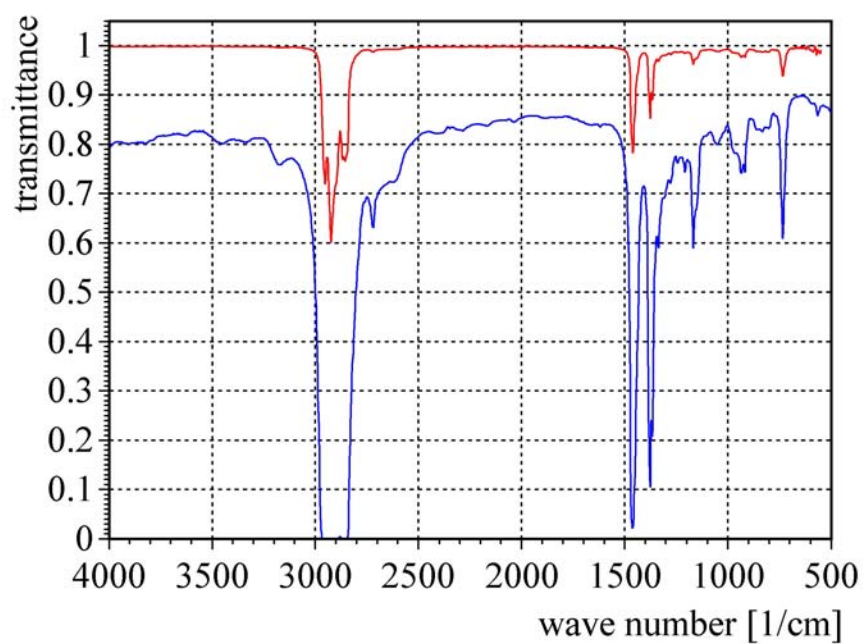
Fig. 6-5:   Infrared transmission spectra of squalan (001) measured with a cuvette (blue curve) and with
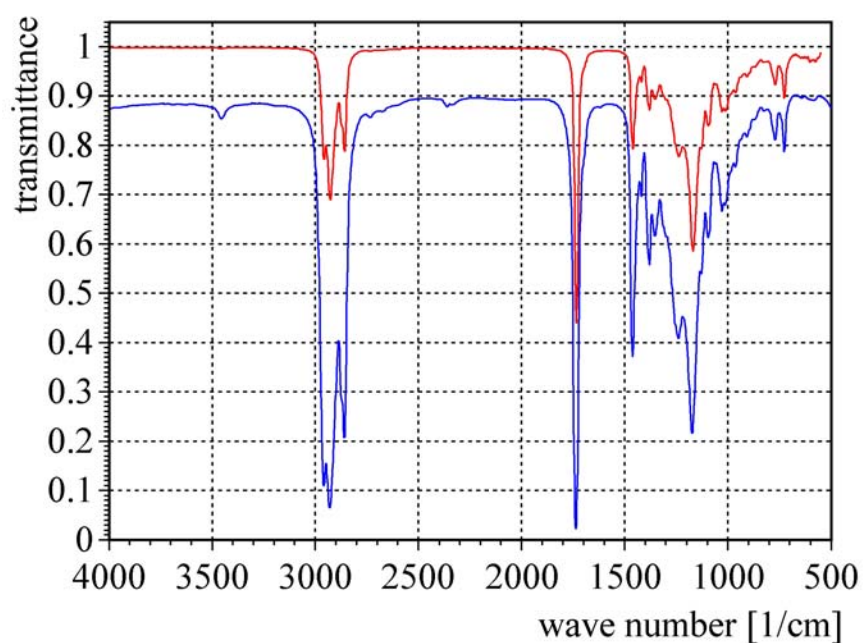ATR (red curve) for comparison.

Fig. 6-6:   Infrared transmission spectra of di-2-ethylhexyl-sebacat (002) measured with a cuvette
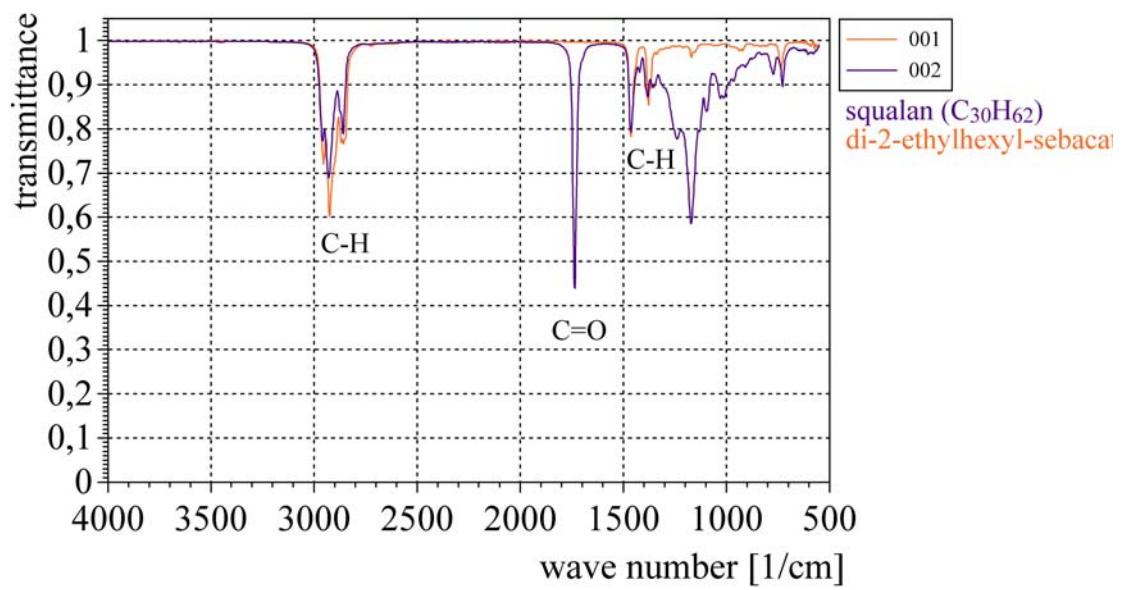(blue curve) and with ATR (red curve) for comparison.

Fig. 6-7:   Infrared transmission spectra of squlan and di-2-ethylhexyl-sebacat measured with ATR. Characteristic peaks of the oil samples are labelled.

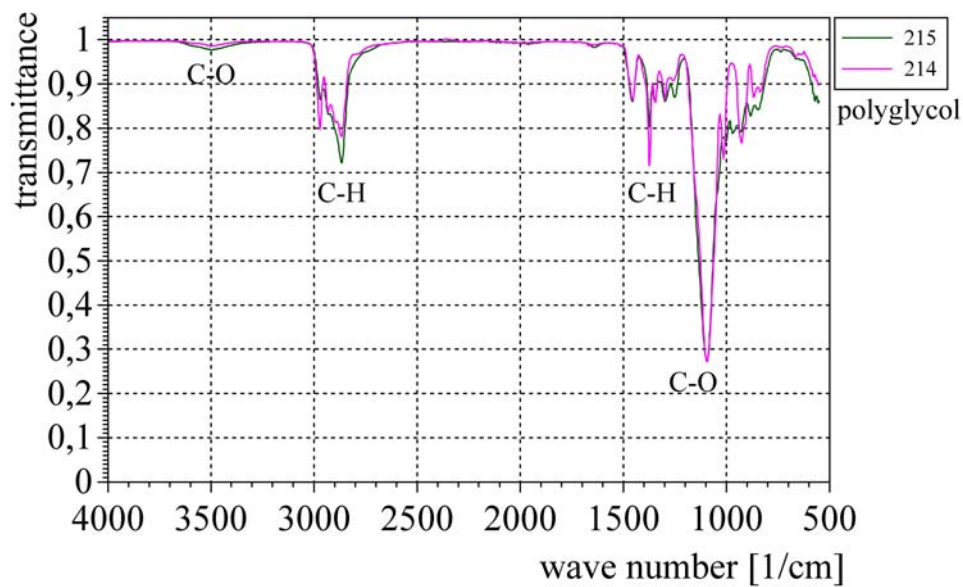Fig. 6-8:   Infrared transmission spectra of polyglycol measured with ATR. Characteristic peaks of the oil samples are labelled.

Fig. 6-9:   Infrared transmission spectra of silicone measured with ATR. Characteristic peaks of the oil samples are labelled.

Fig. 6-10: Infrared transmission spectra of naphtenic and paraffinic mineral oil measured with ATR. Characteristic peaks of the oil samples are labelled.
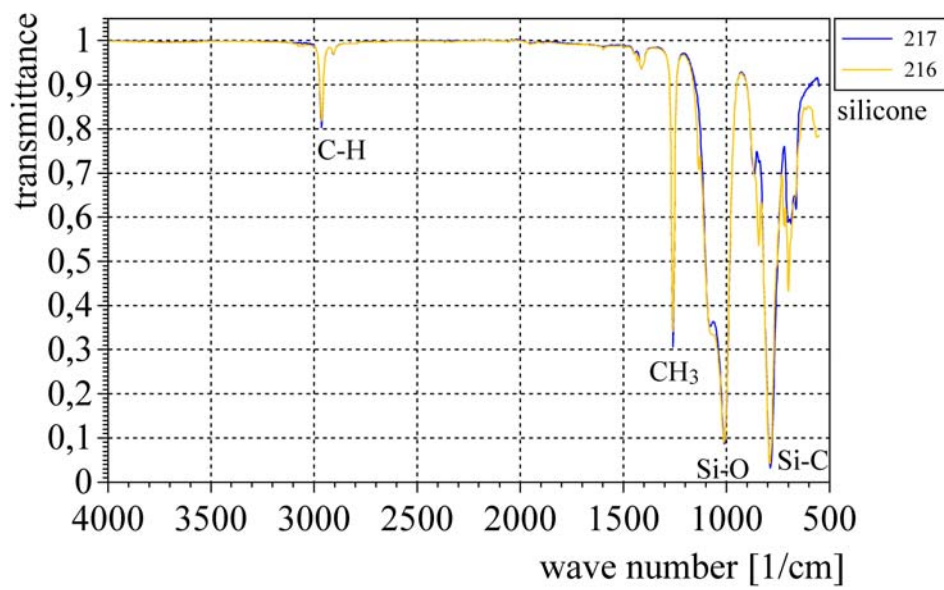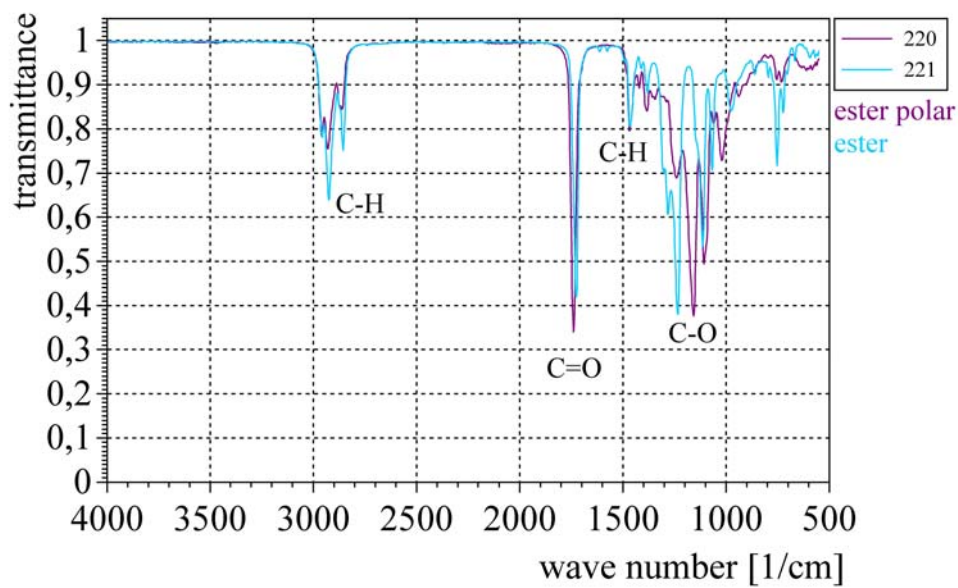
Fig. 6-11: Infrared transmission spectra of polar ester and ester measured with ATR. Characteristic peaks of the oil samples are labelled.
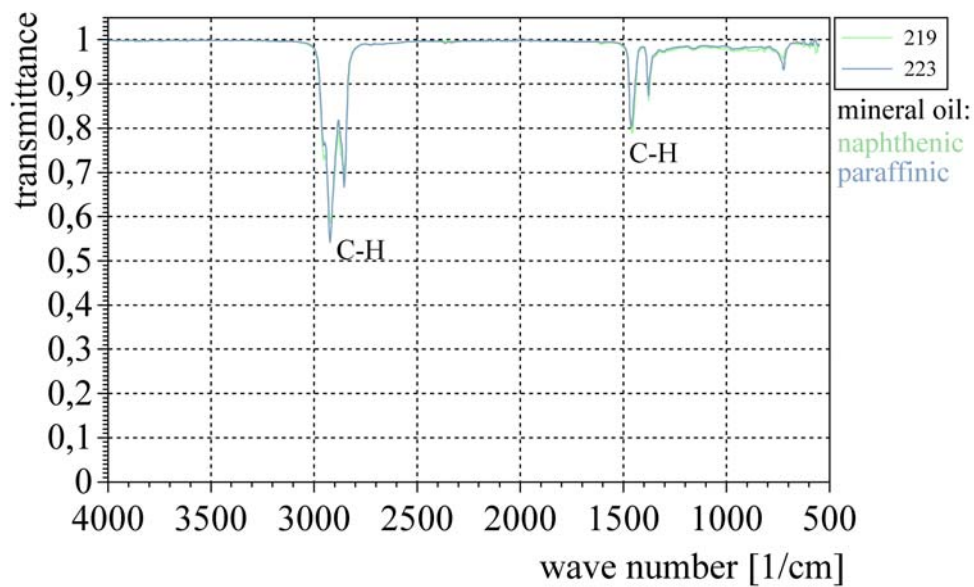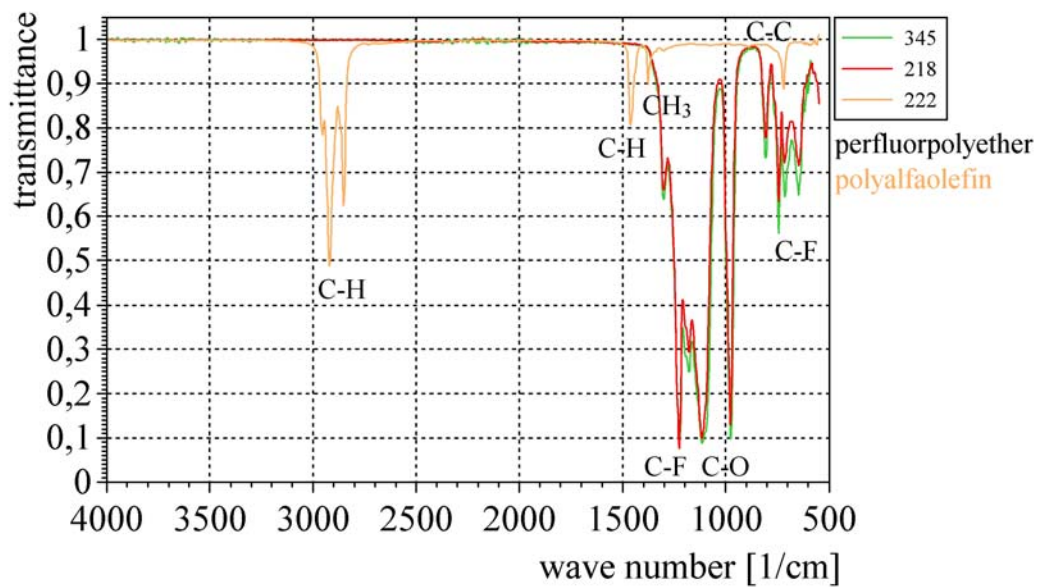

Fig. 6-12: Infrared transmission spectra of perfluorpolyether and polyalfaolefin measured with ATR. Characteristic peaks of the oil samples are labelled.
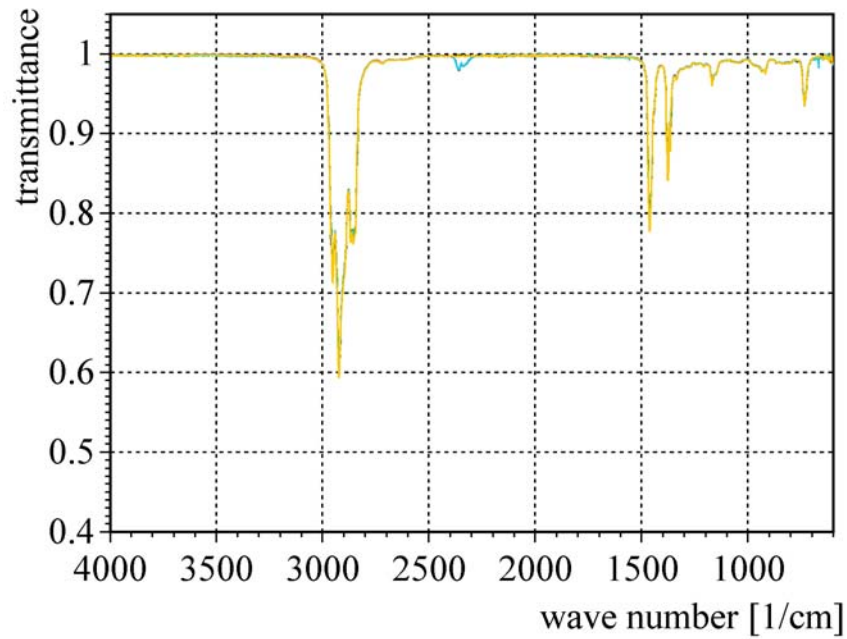
Fig. 6-13: Infrared transmission spectra of squalan (001). Essentially, similar spectra were obtaind for oil samples stressed in the static test rig applying a DC voltage of 120 V (approximately 3000 and 32000 EDM-events) and 12 V (approximately 32000 EDM-events) across the gap between the test specimens.
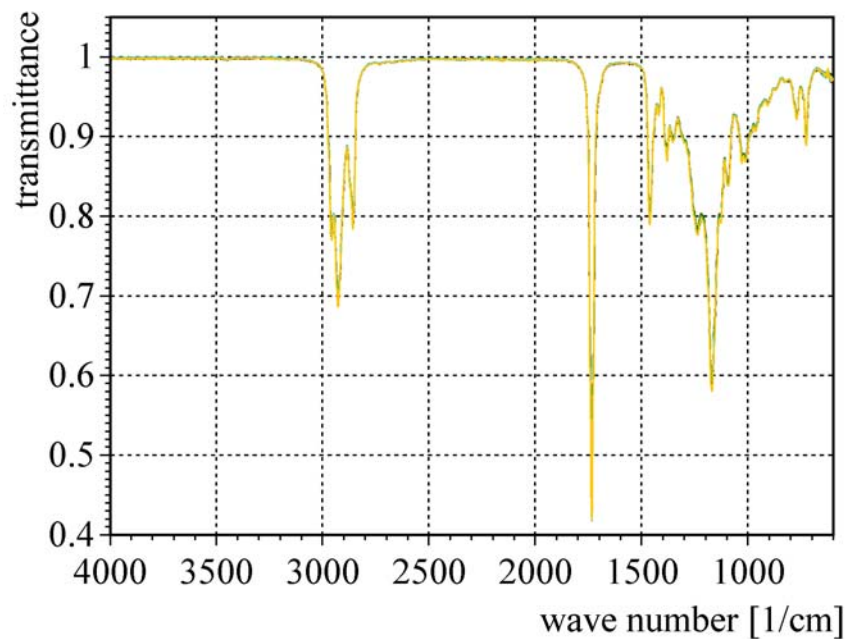
Fig. 6-14: Infrared transmission spectra of di-2-ethylhexyl-sebacat (002). Essentially, similar spectra were obtaind for oil samples stressed in the static test rig applying a DC voltage of 120 V (approximately 3000 and 32000 EDM-events) and 12 V (approximately 32000 EDM-events) across the gap between the test specimens.

Fig. 6-15: Appearance of di-2-ethylhexyl-sebacat (002) unstressed (left), after 32000 EDM-events initiated in the static test rig with a voltage of 12 V (middle) and of 120 V (right).

6.4 Stray capacitances of two investigated three phase induction motors

Two different three-phase induction motors, the green motor (Elin, ÖVE-M10/80, 7.5 kW, modified with insulating sleeves) and the grey motor (SEW-Eurodrive, DU160M2/TF/EV1S, 11 kW, equipped with standard non-insulating bearings), were available for the investigation of their stray capacitances (chapter 5.4). The capacitances between the rotor and the frame and the capacitances between the stator windings and the rotor were determined.

6.4.1 Stray capacitances between the rotor and the motor frame

Two different methods as described in chapter 5.4.1 were employed to determine the stray capacitance C_{RF} between the rotor and the motor frame. According to the first method, an LCR-meter was used to measure C_{RF} directly at the green motor, whereas the grey motor additionally had to be rotated via a belt by another motor to create an insulating lubricant film in its bearings. The values of C_{RF} of the green and the grey motor have been determined as 1.5 nF and 2.6 nF, respectively.

By means of the second method, which can also be utilized for motors in operation, the capacitance C_{RF} of the grey motor was calculated with equation (5.5) (chapter 5.4.1) from the values of the motor shaft-to-frame voltage V_{MSF} (Fig. 6-16) measured before (t_B) and after (t_A) switching a reference capacitance C_{REF} (1 nF) in parallel to C_{RF} by closing a reed relay contact during a period of constant star point-to-frame voltage V_{YF}:

$$C_{RF} = C_{REF} \frac{V_{MSF}(t_A)}{V_{MSF}(t_B) - V_{MSF}(t_A)} = 1 \text{ nF} \frac{6.39 \text{ V}}{8.79 \text{ V} - 6.39 \text{ V}} = 2.66 \text{ nF} \qquad (6.2)$$

After closing the reed relay contact, the motor shaft-to-frame voltage $V_{MSF}(t_A)$ must be measured at a time subsequent to the transient phenomenon (Fig. 6-16). The value of the stray capacitance C_{RF} in the grey motor, determined of this method (2.66 nF), matches very well with the value measured by the LCR-meter (2.6 nF).
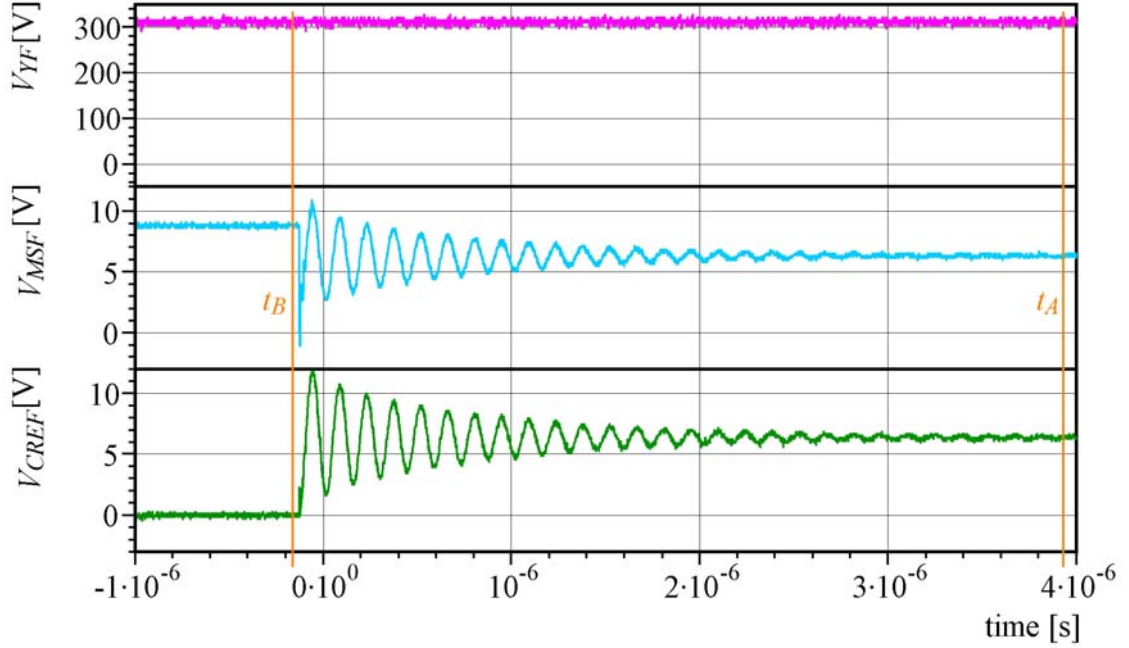
Fig. 6-16: Time dependence of the star point-to-frame voltage (V_{YF}), the motor shaft-to-frame voltage (V_{MSF}) and the voltage across the reference capacitance (V_{CREF}) when the reference capacitance C_{REF} is switched in parallel to the stray capacitance C_{RF} by closing a reed relay contact. The values $V_{MSF}(t_B)$ and $V_{MSF}(t_A)$ used to calculate C_{RF} were measured before (t_B) and after (t_A) the closing of the contact.

To be applicably for the measurement of C_{RF}, both methods require a good electrical contact at the motor shaft (here a rotating mercury contact was used). The first method using only a common LCR-meter requires the motor shaft to be rotated by an external drive, whereas a more complex measuring set-up between the motor shaft and the motor frame is needed for the second method applying a reference capacitance. Although this measurement has to be undertaken only during a period of constant star point-to-frame voltage, the second method permits to measure C_{RF} at motors during normal operation. In both cases, the motor shaft must not be electrically connected to a driven machine, to avoid additional capacitive coupling between the motor shaft and the frame of the driven machine or grounding of the motor shaft via the driven machine.

6.4.2   Stray capacitances between the stator windings and the rotor

The stray capacitances between the stator windings and the rotor of the grey and the green motor were measured on the one hand separately for each end of the windings (Fig. 5-5) and on the other hand for the whole windings (Fig. 5-6). The results of these measurements are listed in Tab. 6-2 and Tab. 6-3. Representatively, the square wave signal (4 kHz) V_{SW} (depicted in sky-blue) between the stator winding W_3 and the motor frame supplied by the frequency synthesiser and the signal V_{RF} (depicted in pink) capacitively coupled between the rotor and the motor frame, both measured with the oscilloscope at the green motor, are shown in Fig. 6-17. The stray capacitance C_{SRE} between one end of one stator winding or the whole stator winding and the rotor can be calculated using equation (6.3) (according to equation (5.6) in chapter 5.4.2), if the capacitance C_{RF} between the rotor and the motor frame and the peak to peak values of the signals V_{SW} and V_{RF} are known.

$$C_{SRE} = \frac{C_{RF}}{\frac{V_{SW}}{V_{RF}} - 1} \longrightarrow C_{SR3} = \frac{1.5 \text{ nF}}{\frac{19.69\,[\text{V}]}{0.438[\text{V}]} - 1} = 34{,}1 \text{ pF} \tag{6.3}$$

The values for C_{RF} of the two motors have been measured before (chapter 6.4.1). The total capacitive coupling C_{SR3} between the stator winding W_3 and the rotor in the green motor was calculated from equation (6.3) using the peak-to-peak values of the signals V_{SW} and V_{RF} obtained from measurement (Fig. 6-17). Two differences in the investigated stray capacitances of both motors are obvious (Tab. 6-2 and Tab. 6-3).

stator winding		W_1		W_2		W_3	
end of the winding		U	Y	U	Y	U	Y
stray capacitance		C_{SR1U}	C_{SR1Y}	C_{SR2U}	C_{SR2Y}	C_{SR3U}	C_{SR3Y}
green motor	[pF]	17.3	10.6	20.2	14.0	18.7	14.1
grey motor	[pF]	2.2	2.1	29.3	31.7	11.3	12.0

Tab. 6-2:   Stray capacitances between the ends of the stator windings and the rotor measured at the green motor and the grey motor. The third index indicates the corresponding stator winding W_1, W_2 and W_3 by the numbers 1, 2 and 3, respectively. The ends of the stator windings, usually connected to the power supply and the motor star point, are denoted by the fourth index with U and Y, respectively.

The total capacitive coupling between each stator winding and the rotor is nearly equal for the green motor ($C_{SR1} \approx C_{SR2} \approx C_{SR3}$), whereas in the grey motor the corresponding stray capacitances are significantly different. Further, in the grey motor the capacitive coupling between both ends of each stator winding and the rotor match well

($C_{SR1U} \approx C_{SR1Y}$; $C_{SR2U} \approx C_{SR2Y}$; $C_{SR3U} \approx C_{SR3Y}$),   whereas   the   corresponding   stray capacitances in the green motor exhibit noticeable differences. It is assumed, that these inhomogeneities in the stray capacitances originate from differences in the arrangement of the stator windings.

stator winding		W_1	W_2	W_3	W_1	W_2	W_3
stray capacitance		C_{SR1}	C_{SR2}	C_{SR3}	$C_{SR1U}+C_{SR1Y}$	$C_{SR2U}+C_{SR2Y}$	$C_{SR3U}+C_{SR3Y}$
green motor	[pF]	28.5	35.5	34.1	27.9	34.2	32.8
grey motor	[pF]	4.0	57.2	21.9	4.3	61.0	23.3

Tab. 6-3:   Stray capacitances C_{SR1}, C_{SR2} and C_{SR3} between the whole stator winding W_1, W_2 and W_3, respectively, and the rotor measured at the green motor and the grey motor. The sums of corresponding stray capacitances, measured separately at both ends of each stator winding (Tab. 6-2), are listed in the last three columns on the right side for comparison.
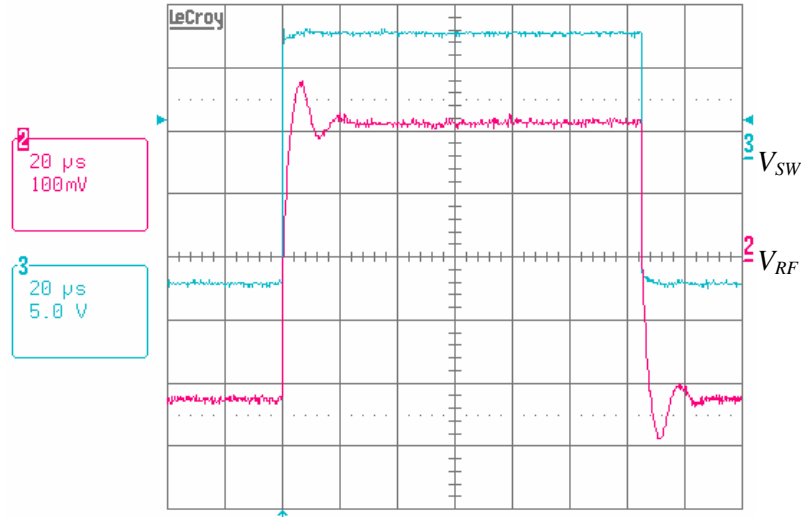
Fig. 6-17:   Square wave signal (4 kHz) V_{SW} (sky-blue curve) supplied by the frequency synthesiser between the stator winding W_3 and the motor frame and the signal V_{RF} (pink curve) capacitively coupled between the rotor and the motor frame, both measured with the oscilloscope at the green motor.

6.5   Electrical regime of an induction motor driven by a frequency converter

The characterisation of the electrical regime of an induction motor driven by a frequency converter needs the knowledge of some important properties of such a system, which are determined by, e.g., the star point-to-frame voltage, the motor shaft-to-frame voltage, the motor frame-to-ground voltage, or voltages and currents in the PE-wire between the frequency converter and the driven motor. If the motor shaft-to-frame voltage is available, it exists also across the bearings and may cause EDM-processes and, hence, bearing damage.

6.5.1   Star point-to-frame voltage, motor shaft-to-frame voltage and phase voltages

The star point-to-frame voltage (V_{YF}), the motor shaft-to-frame voltage (V_{MSF}), and the phase voltages (V_1, V_2 and V_3), at the grey motor driven by a frequency converter measured with the oscilloscope as described in chapter 5.5.1, are shown in Fig. 6-18. It is evident that the star point-to-frame voltage depends on the sum of the phase voltages supplied by the frequency converter to the motor according to equation (3.1). The star point-to-frame voltage changes its level at each switching operation, when one of the phase voltages is switched to another voltage level by the frequency converter. Additionally, it can be seen clearly that the shape of the motor shaft-to-frame voltage, which is capacitively coupled from the stator to the rotor (and the motor shaft), is related to the star point-to-frame voltage. The motor shaft-to-frame voltage changes its level at the same moments as the star point-to-frame voltage, but the voltage steps ΔV_{MSF} between two successive voltage levels are different for V_{MSF}, in comparison to V_{YF}, which show three equal voltage steps ΔV_{YF} (Tab. 6-4).

voltage steps measured at	$X =$	1	2	3
the star point-to-frame voltage	ΔV_{YF} [V]	181	181	181
the motor shaft-to-frame voltage	ΔV_{MSF} [V]	3.1	9.1	5.6
voltage steps calculated for	$X =$	1	2	3
the motor shaft-to-frame voltage	ΔV_{MSF} [V]	3.52	8.99	5.36

Tab. 6-4:   Voltage steps measured at the star point-to-frame voltage and the motor shaft-to-frame voltage during the switching operation of the frequency converter (Fig. 6-18). With the measured values of the different stray capacitances between the stator windings and the rotor (Tab. 6-2), the voltage steps generated at the motor shaft were also calculated from equation (6.4) for comparison with measurement. The values of the variable X (= 1, 2 or 3) indicate the corresponding stator winding (W_1, W_2 or W_3).

The voltage steps ΔV_{MSF} in the grey motor at the motor shaft-to-frame voltage during each switching operation of the frequency converter, generated by capacitive coupling of V_{YF} to the rotor, were calculated from the stray capacitances between the ends of the stator windings and the rotor (Tab. 6-2) and from the voltage steps ΔV_{YF} at the star point-to-frame voltage as (Fig. 6-19):

$$\Delta V_{MSF}\left(X\right) = \frac{\left(3C_{SRXU} + C_{SR1Y} + C_{SR2Y} + C_{SR3Y}\right)\Delta V_{YF}}{C_{SR1U} + C_{SR2U} + C_{SR3U} + C_{SR1Y} + C_{SR2Y} + C_{SR3Y} + C_{RF}} \qquad (6.4)$$

Here, the variable X (= 1, 2 or 3) in equation (6.4) indicates the output phase (U_1, U_2 or U_3), which is switched over by the frequency converter and, hence, generates voltage

steps at V_{YF} and V_{MSF}. The calculated voltage steps are listed in Tab. 6-4 and they match very well with the corresponding voltage steps actually measured at V_{MSF}.
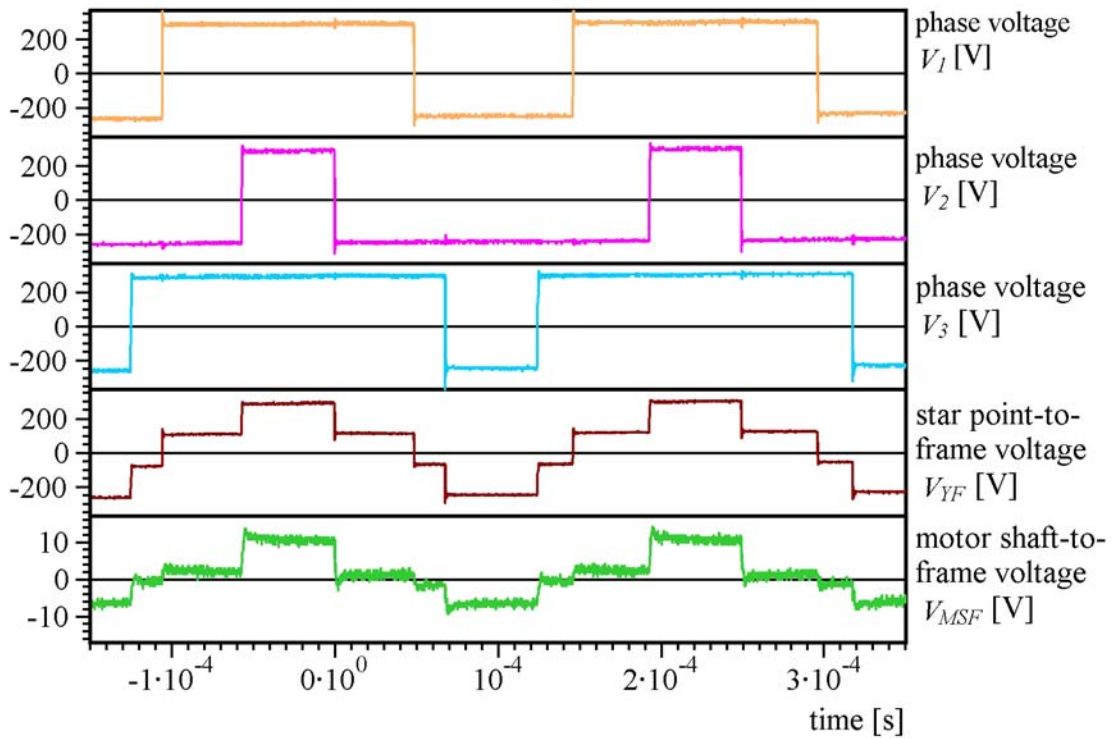

Fig. 6-18: Phase voltages (V_1, V_2 and V_3) supplied by the frequency converter to the grey motor, and the star point-to-ground voltage (V_{YF}) and the motor shaft-to-frame voltage (V_{MSF}) at the grey motor measured with an oscilloscope. Although the voltage steps ΔV_{YF} at V_{YF} are equal, the corresponding voltage steps ΔV_{MSF} at V_{MSF} are different due to the non-uniform capacitive coupling between the stator windings and the rotor.
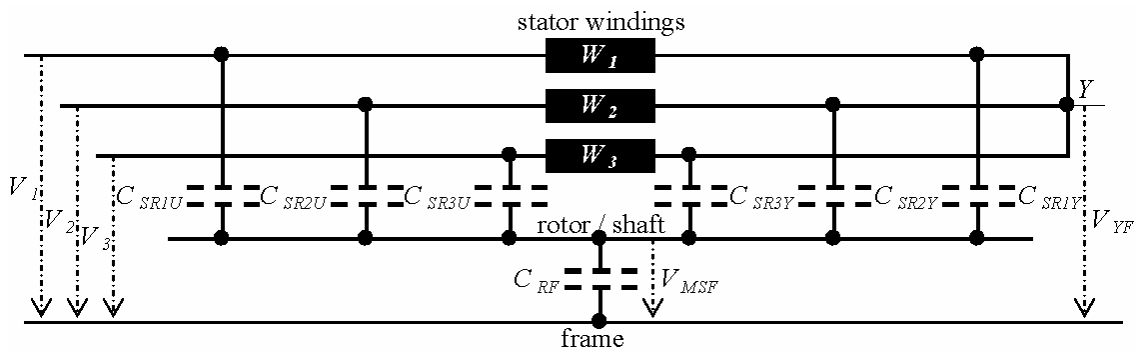
Fig. 6-19: Schematic diagram of the stray capacitances between each end of each stator winding and the rotor (Tab. 6-2) in series to the capacitance C_{RF} between the rotor and the frame. The star point-to-frame voltage V_{YF} is determined by the phase voltages (V_1, V_2 and V_3) supplied by the frequency converter. The motor shaft-to-frame voltage V_{MSF} is generated due to the capacitive coupling of V_{YF} to the rotor (and the motor shaft).

6.5.2 Occurrence of EDM-processes due to the motor shaft-to-frame voltage and surface roughness
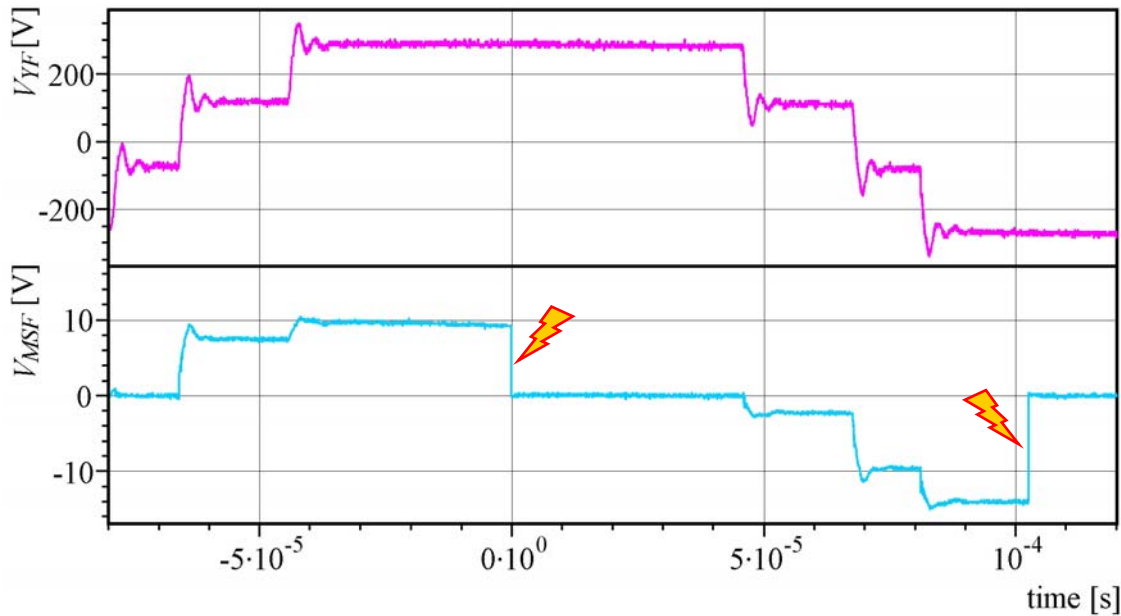

Fig. 6-20: Star point-to-frame voltage V_{YF} (pink curve) and motor shaft-to-frame voltage V_{MSF} (sky-blue curve) measured with an oscilloscope at the grey motor driven by a frequency converter. During EDM-events, breakdowns at the motor shaft-to-frame voltage occur (indicated by yellow arrows).

EDM-processes and consequently EDM-currents occur under certain conditions in bearings of frequency converter driven motors (chapter 3.7), i.e., the electric field strength across the lubricant film in the bearing must exceed a threshold to initiate an EDM-process. The threshold of the electric field strength can be reached either by diminishing the lubricant film due to the approach of asperities at the raceways of the inner ring, the outer ring and the rolling elements of the bearing, or by increasing the voltage V_{MSF} across the bearing. Thus, the appearance of EDM-events does *not* necessarily coincide with the switching operations of the frequency converter (Fig. 6-20). If no EDM-process occurs, under full-film lubrication conditions the shape of the motor shaft-to-frame voltage is similar to the shape of the star point-to-frame voltage, except for the non-uniform voltage steps, and is, in general, different from zero potential (Fig. 6-18). In contrast, after an EDM-event V_{MSF} is equal (or close to) zero potential and will remain at this level until the next following voltage step at V_{YF} occurs (Fig. 6-20, 45 µs). It must be pointed out that each voltage step at V_{MSF} generated subsequently to an EDM-event starts at (or close to) zero potential. Hence, the motor shaft-to-frame voltage is shifted in relation to its usual levels (Fig. 6-18), which are available until the first EDM-process occurs.

6.5.3   Loop resistance of an EDM-loop

The loop resistance R_{LE} of the EDM-loop (Fig. 3-5) in the grey motor was calculated by means of equation (5.7) from the values of the stray capacitance C_{RF} (2.6 nF) and the shortest time constants τ_S (16.9 ns…19.7 ns) measured with the oscilloscope at the breakdowns of the motor shaft-to-frame voltage (EDM-events) in the grey motor driven by a frequency converter as described in chapter 5.5.3.

$$R_{LE} = \frac{\tau_S}{C_{RF}} \longrightarrow R_{LE} = \frac{(16.9...19.7)\ \text{ns}}{2.6\ \text{nF}} = (6.5...7.6)\ \Omega \qquad (6.5)$$

This result for R_{LE} of the grey motor is in the same order of magnitude as the value (10 Ω) obtained from Fig. 2-6 [14] (chapter 2.3).

6.5.4   EDM-currents, high-frequency *dv/dt*-currents and EDM-energies

By means of the developed measuring technique (chapter 5.5.4), EDM-currents were measured indirectly at the grey motor driven by a frequency converter (Fig. 6-21) using a capacitor C_M (0.12 nF) and a resistor R_M (235 Ω) in the external measuring circuit (Fig. 5-10). The EDM-current (Fig. 6-21, green curve) was calculated according to equation (5.8) from the voltage V_{F*} and the loop resistance R_{LE}. The knowledge of the time dependence of the voltage $V_{MSF}(t)$ (blue curve) across the bearing and the EDM-current $I_{EDM}(t)$ flowing through the bearing during an EDM-process allows to calculate the power $P_{EDM}^*(t)$ (orange curve) and the EDM-energy $E_{EDM}^*(t)$ (red curve) transferred to the bearing as:

$$P_{EDM}^*(t) = \left| V_{MSF}(t) \cdot I_{EDM}(t) \right| \qquad (6.6)$$

$$E_{EDM}^*(t) = \int P_{EDM}^*(t)\,dt = \int \left| V_{MSF}(t) \cdot I_{EDM}(t) \right|\,dt \qquad (6.7)$$

During the observed EDM-process (Fig. 6-21), a fraction ($E_{EDM}^* = 146\ \text{nWs}$) of the total EDM-energy was transferred to the bearing. The total EDM-energy E_{EDM}, was stored as electric energy in the stray capacitance C_{RF} before onset of the EDM-process. It could be calculated for this EDM-event by means of equation (6.8). Here, it must be taken into account that the measured value of the capacitance C_{RF} also includes the bearing capacitances C_{B1} and C_{B2} (chapter 5.4.1).

$$E_{EDM} = \tfrac{1}{2} \cdot \left(C_{RF} + C_{B1} + C_{B2} \right) \cdot V_{MSF}^2 \left(t_0 \right) \; \triangleq \; \tfrac{1}{2} \cdot C_{RF} \cdot V_{MSF}^2 \left(t_0 \right)$$

$$\longrightarrow \; E_{EDM} = \tfrac{1}{2} \cdot 2.6 \text{ nF} \cdot \left(14.2 \text{ V} \right)^2 = 262 \text{ nWs}$$

(6.8)

The value $V_{MSF}(t_0)$ of the motor shaft-to-frame voltage was measured at the time t_0 before the onset of the EDM-process (Fig. 6-21). The results show that about 55 % of the total energy E_{EDM} was transferred to the bearing during this EDM-process. The residual fraction of the energy is assumed to be dissipated at the loop resistance R_{LE}, distributed along the EDM-circuit.
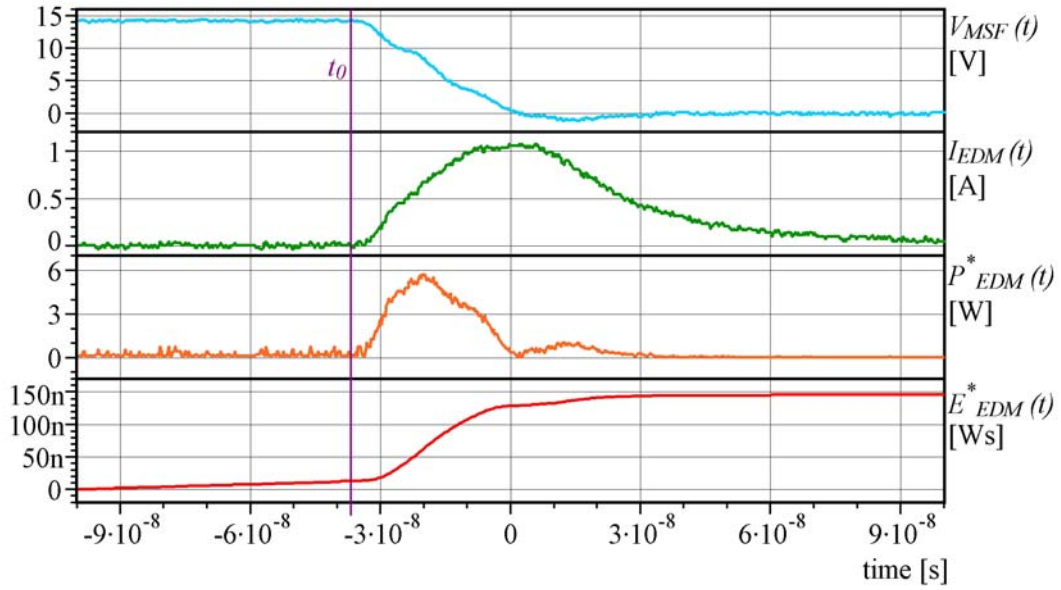

Fig. 6-21: Time dependence of the voltage $V_{MSF}(t)$, the EDM-current $I_{EDM}(t)$, the power $P^*_{EDM}(t)$ and the EDM-energy $E^*_{EDM}(t)$ during an EDM-process in a bearing of the grey motor. The voltages $V_{MSF}(t)$ and $V_{F*}(t)$ were measured with the oscilloscope (chapter 5.5.4, Fig. 5-10) and the other quantities, $I_{EDM}(t)$, $P^*_{EDM}(t)$ and $E^*_{EDM}(t)$, were calculated by means of the equations (5.8), (6.6) and (6.7).

Additionally, the behaviour of $V_{MSF}(t)$ in relation to $I_{EDM}(t)$, both measured during an EDM-process in a bearing of the grey motor (Fig. 6-21), is shown in Fig. 6-22. In this representation, the EDM-process starts at the point of maximum voltage (here about 14 V) and zero current. It is obvious that during this EDM-event the current increased while the motor shaft-to-frame voltage decreased in the same time span (negative slope of the curve, green line in Fig. 6-22). Such a behaviour indicates an avalanche-like discharge effect during the observed EDM-process and supports the assumption that sparks, occurring during EDM-events, in finite regions of the bearings crack the lubricants and melt the steel at the raceways of the rolling elements, the inner rings and the outer rings of bearings and, hence, generate mirco craters. The duration of the spark can be estimated from the period of the negative slope in Fig. 6-22 and was about 35 ns. The corresponding resistance during this period was determined by means of the slope

of the green line and was approximately $-11\,\Omega$. The absolute value of this result matches well with the result ($10\,\Omega$, chapter 2.3) from V. Hausberg et al. [14]. But more information on the behaviour of EDM-processes was obtained from the measurement results shown in Fig. 6-21 and Fig. 6-22. In contrast to the described behaviour, in an ohmic regime the current and the voltage obey Ohm's law. That means they will form a straight line with positive slope, if they are plotted in a diagram according to Fig. 6-22. The comparison of the values of $V_{MSF}(t)$ and $I_{EDM}(t)$ with the trajectories of constant power (orange curves) exhibits that the instantaneous power rises up to nearly 6 W. The same value for the maximal power can be read from Fig. 6-21.
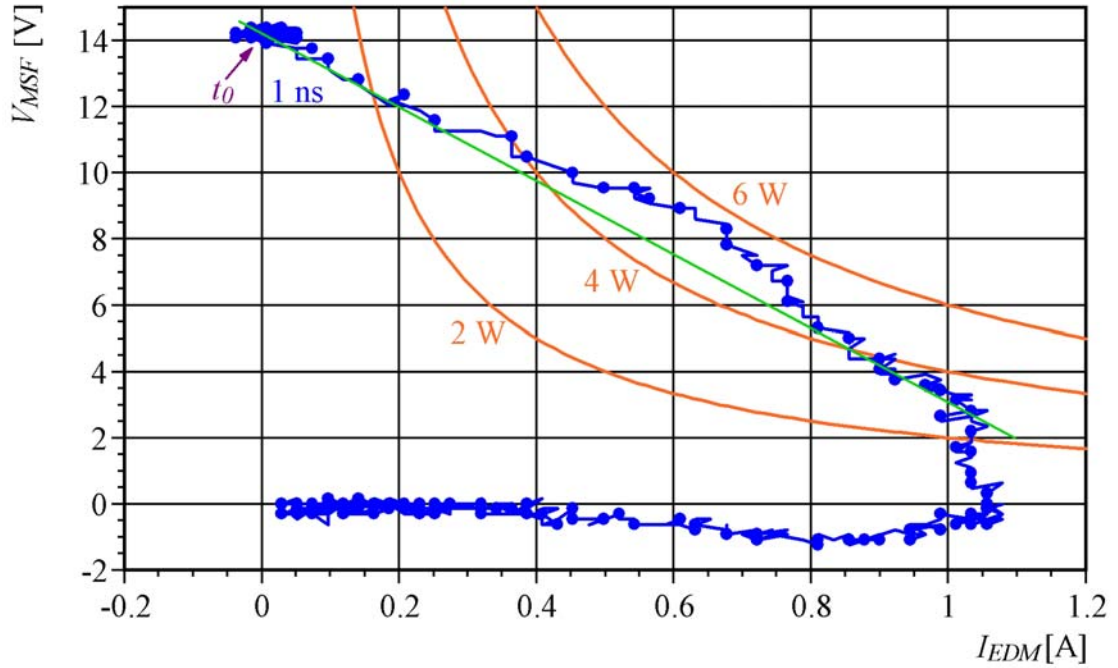

Fig. 6-22: The motor shaft-to-frame voltage V_{MSF} in relation to the EDM-current I_{EDM}, both measured during an EDM-process in a bearing of the grey motor (Fig. 6-21). The duration between two blue circles is 1 ns. The time t_0 is also shown in Fig. 6-21. The orange curves are trajectories of equal power. The slope of the green curve corresponds to the resistance, which had the system during the period of the negative slope.

A series of EDM-events was detected with the oscilloscope at the motor shaft-to-frame voltage of the grey motor (sky-blue curves in Fig. 6-23) of the grey motor, to obtain data for the verification of a simulated EDM-event (red curve). The EDM-loop of the grey motor was described by means of an equivalent electric circuit (Fig. 6-24) comprising a capacitance C_E, a resistance R_E, an inductance L_E and a switch S_E, which represent the stray capacitance C_{RF}, the loop resistance R_{LE}, the inductance L_{LE} and the contact in the bearing, respectively. It must be pointed out that the loop resistance R_{LE} and the inductance L_{LE} of a real system are distributed along the EDM-loop in contrast to schematic diagrams which always comprise lumped elements.
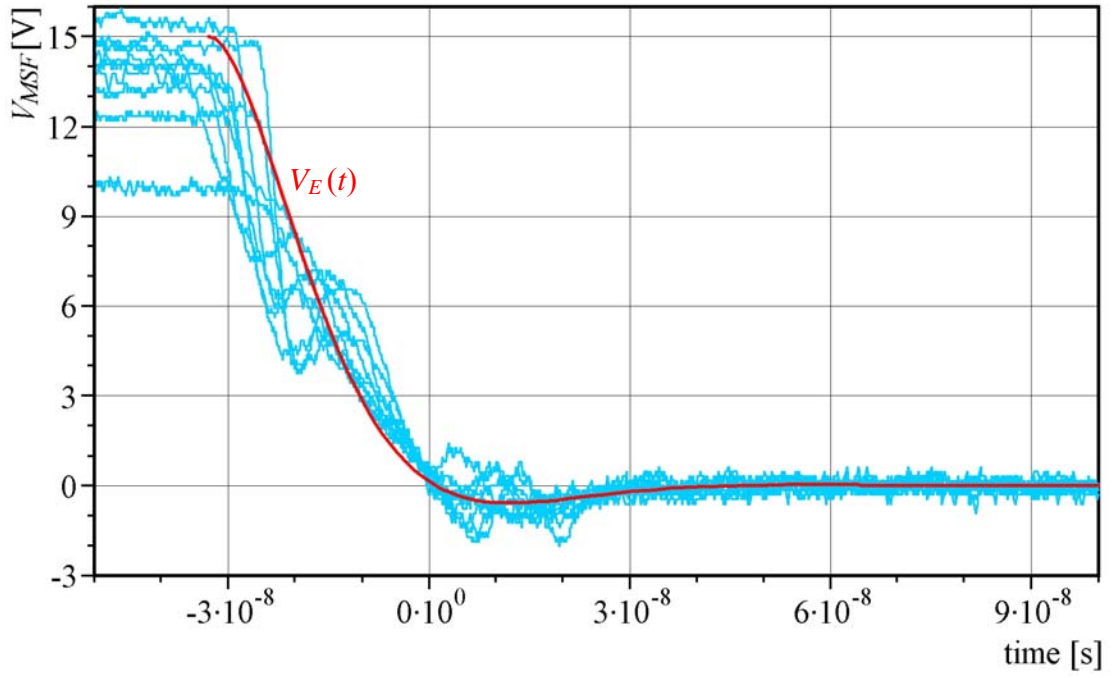
Fig. 6-23:   Time dependence of a series of EDM-processes measured with an oscilloscope at the motor shaft-to-frame voltage V_{MSF} (sky-blue curves) of the grey motor. The EDM-loop of the grey motor was described by means of an equivalent electric circuit (Fig. 6-24). The red curve shows the calculated time dependence of the voltage $V_E(t)$ after closing the switch in the equivalent electric circuit.
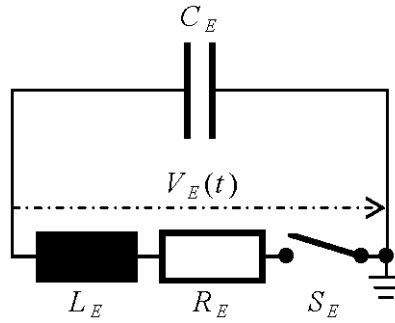
Fig. 6-24:   Schematic diagram of the equivalent electric circuit comprising a capacitance C_E, a resistance R_E, an inductance L_E and a switch S_E for the simulation of the EDM-loop of an induction motor. The voltage V_E was calculated by means of equation (6.9).

A simulated EDM-event can be initiated in the equivalent electric circuit by closing the contact S_E. The time dependence of the voltage $V_E(t)$ was calculated by means of equation (6.9), whereby the values for R_E, L_E, C_E and $V_E(t_0)$, the initial voltage before the closing of the switch S_E, were fitted for optimal simulation of V_{MSF} by $V_E(t)$.

$$V_E(t) = V_E(t_0)\left(\frac{R_E L_E}{2\omega} \sin(\omega_E t) + \cos(\omega_E t) \right) e^{-\frac{R_E}{2L_E}t}$$

$$\text{with } \omega_E = \sqrt{\frac{1}{L_E C_E} - \frac{R_E^2}{4L_E^2}}$$

(6.9)

The final values used for R_E, L_E, C_E and $V_E(t_0)$ in this simulation are 5.5 Ω, 38 nH, 2.6 nF, and 15 V respectively. The good match is evident of R_E and C_E with the values for R_{LE} (6.5 Ω to 7.6 Ω, chapter 6.5.3) and C_{RF} (2.6 nF and 2.66 nF, chapter 6.4.1), respectively, as determined before by different methods. Further, the results show that the inherent inductance L_{LE} represented by L_E in the equivalent electric circuit is small and hence may be neglected.
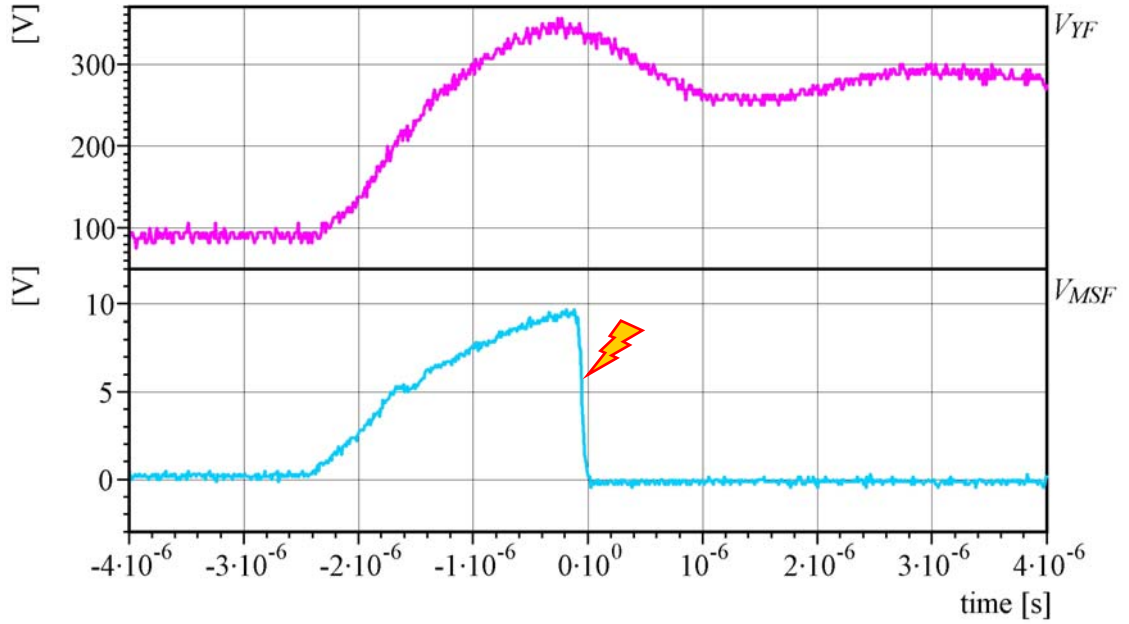

Fig. 6-25: Time dependence of the star point-to-frame voltage (pink curve) and the motor shaft-to-frame voltage (sky-blue curve) in the grey motor during a switching operation of the frequency converter. Additionally, an EDM-event (marked by a yellow arrow) is visible here during the transient phenomenon of the switching operation. It is obvious that the slew rate of V_{MSF} is much higher during this EDM-process than during the switching operation.

Voltage steps (ΔV_{MSF}) appear at the motor shaft-to-frame voltage (Fig. 6-25) by the switching operations of the frequency converter as well as by EDM-processes. In the first case, these voltage steps V_{MSF} are produced by the capacitive coupling between the star point-to-frame voltage and V_{MSF} and, in the second case, the voltage steps are caused by breakdowns of V_{MSF} during EDM-events. The magnitudes of the corresponding currents (I_{dV}) across the stray capacitance (C_{RF}), generated by these voltage steps, depend on the slew rates of the steps at V_{MSF} and the magnitude of the capacitance C_{RF}, and result from equation (6.10) as:

$$I_{dV} = C_{RF} \left| \frac{dV_{MSF}}{dt} \right| \tag{6.10}$$

At the grey motor the slew rates of V_{MSF}, measured during EDM-processes, were typically in the range from 90 V/μs to 630 V/μs, whereas the corresponding values

detected during the switching operations of the frequency converter were only between 1.2 V/μs to 7.8 V/μs. Thus, equation (6.10) has yields peak values of up to 1.6 A for typical EDM-currents but only of about 20 mA for the so-called high-frequency *dv/dt*-currents originating from the switching operations of the frequency converter. The slew rates of the motor shaft-to-frame voltage as evident in from Fig. 6-25, are 90 V/μs for the EDM-process and 4.2 V/μs during the switching operation. With equation (6.10) this leads peak values of the corresponding currents of 234 mA and 10.9 mA, respectively. Also the peak value of the current (1.06 A) (Fig. 6-21), measured during an EDM-process at the grey motor, matches very well with the value (1.1 A) resulting from equation (6.10) using the corresponding slew rate (417 V/μs) of V_{MSF}.

The energy E^*_{EDM} transferred to the contact area in a bearing depends on the motor shaft-to-frame voltage and the EDM-current (equation (6.7)). Therefore, not only a high motor shaft-to-frame voltage but also high EDM-currents, originating from the high slew rates at V_{MSF}, are responsible for high energies E^*_{EDM}, which may deteriorate or destroy the lubricant and a finite region at the surfaces of the raceways in the contact area of the bearing. By means of equation (6.10) a good estimation for the peak values of EDM-currents is possible, but a more sophisticated analysis of EDM-processes is possible by the measurement of $V_{MSF}(t)$ and $I_{EDM}(t)$, as discussed in chapter 5.5.4, and the subsequent calculation of $P^*_{EDM}(t)$ and $E^*_{EDM}(t)$ (equations (6.6) and (6.7)).

6.5.5   Effects of currents in the PE-wire and the shield of power cables and of the motor frame-to-ground voltage

Using the measuring set-up as described in chapter 5.5.5, the time dependences of the motor frame-to-ground voltage (V_{FG}) at the grey motor and of currents in the PE-wire (I_{PE}) and the shield (I_S) were measured. Thereby, the motor was operated without load at standstill (0 rpm) or at a rotational speed of 2000 rpm and was connected to the frequency converter either by a shielded standard power cable of 2.5 m length or an unshielded cable of 37 m length.

If the grey motor was operated at standstill, only two voltage levels, the maximum and the minimum level, were observed (Fig. 6-26). That means all three phase voltages were switched over nearly simultaneously by the frequency converter. Thus the motor shaft-to-frame voltage varied only between the maximum and the minimum level and the highest possible voltage steps were applied to the system during the switching operation of the frequency converter. Therefore, also the high-frequency *dv/dt*-currents were

maximised in this situation. When the shield of the standard power cable was disconnected, high peaks occurred at V_{FG} (up to 51 V peak) and I_{PE} (up to 7 A peak) (Fig. 6-27). In contrast, with the shield connected, the peak values at V_{FG} and I_{PE} were distinctly smaller, up to 12 V and 2 A, respectively (Fig. 6-26).

Fig. 6-26: Star point-to-ground voltage (pink curve), frame-to-ground voltage (sky-blue curve) and current in the PE-wire (green curve) between the frequency converter and the motor frame measured with an oscilloscope at the grey motor at standstill (0 rpm). The standard power cable (2.5 m) was installed between the motor and the frequency converter, whereby the PE-wire and the shield were connected in the usual way.

Fig. 6-27: Star point-to-ground voltage (pink curve), frame-to-ground voltage (sky-blue curve) and current in the PE-wire (green curve) between the frequency converter and the motor frame measured with an oscilloscope at the grey motor at standstill (0 rpm). The standard power cable (2.5 m) was installed between the motor and the frequency converter, whereby only the PE-wire was connected but the shield was disconnected.

Obviously, the shield provided good high-frequency grounding with respect to *dv/dt*-currents in the drive system. If the shield was disconnected, the *dv/dt*-currents had to flow along the PE-wire. Thus, this insufficient high-frequency grounding conditions generated high voltage peaks at V_{FG} originating from the high-frequency *dv/dt*-currents and the (unavoidable) inductance of the PE-wire. Even worse operating conditions were created at the drive system, replacing the standard power cable by a long (37 m) and unshielded cable between the frequency converter and the motor and, hence, increasing the inductance in the PE-wire. Thus, the transient phenomena were augmented at the star point-to-ground voltage and the motor frame-to-ground voltage during the switching operations of the frequency converter (Fig. 6-28). All these circumstances resulted in peak values up to 78 V and 5.2 A at V_{FG} and I_{PE}, respectively.
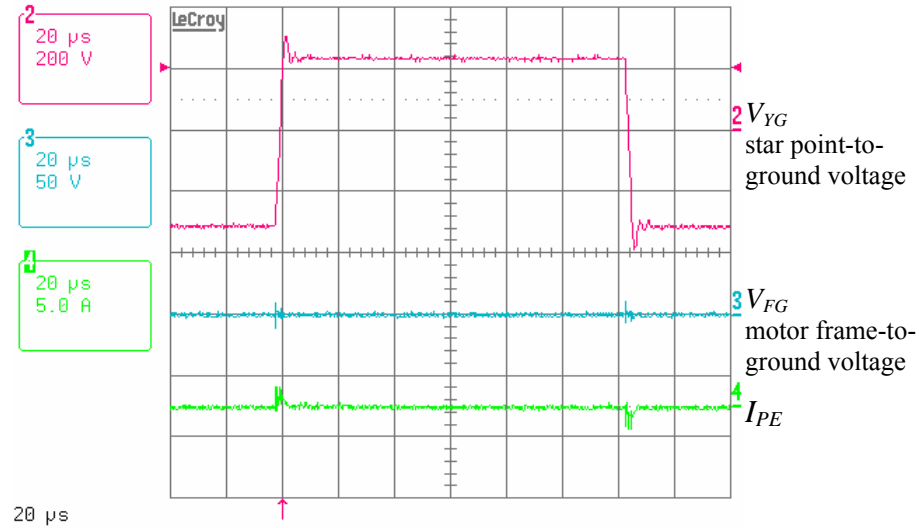

Fig. 6-28:   Star point-to-ground voltage (pink curve), frame-to-ground voltage (sky-blue curve) and current in the PE-wire (green curve) between the frequency converter and the motor frame measured with an oscilloscope at the grey motor at standstill (0 rpm). A long (37 m) and unshielded power cable was installed between the motor and the frequency converter.

Additionally, the drive system was investigated while the motor rotated without load at a rotational speed of 2000 rpm. Under these operating conditions, the common shape of the star point-to-ground voltage was observed (Fig. 6-29 and Fig. 6-30). The figures show that the peaks at the motor frame-to-ground voltage and the current ($I_{PE}+I_S$), flowing through the PE-wire and the shield coincide with the voltage steps at V_{YG}, i.e. they occurred during the switching operation of the frequency converter. Hence, these peaks were caused by the high-frequency *dv/dt*-currents and the inductance of the PE-wire and the shield. When the standard power cable was used, peak values of up to 16 V and 6.7 A, respectively, were measured at V_{FG} and $I_{PE}+I_S$, whereas the installation of the long (37 m) and unshielded power cable yielded to peak values of up to 46 V and 3.3 A, respectively.

Fig. 6-29: Star point-to-ground voltage (pink curve), frame-to-ground voltage (sky-blue curve) and sum of the currents in the PE-wire and the shield (green curve) between the frequency converter and the motor frame measured with an oscilloscope at the grey motor operating at a rotational speed of 2000 rpm. The standard power cable (2.5 m) was installed between the motor and the frequency converter, whereby the PE-wire and the shield were connected in the usual way.
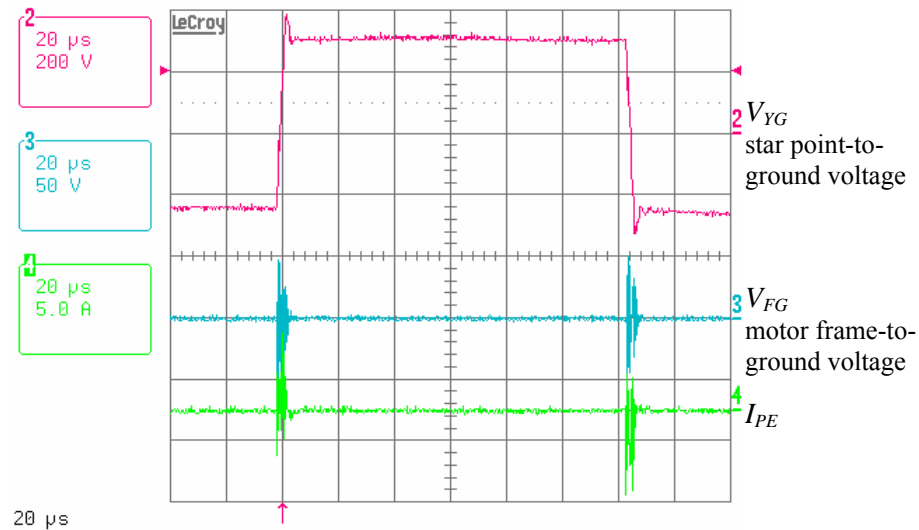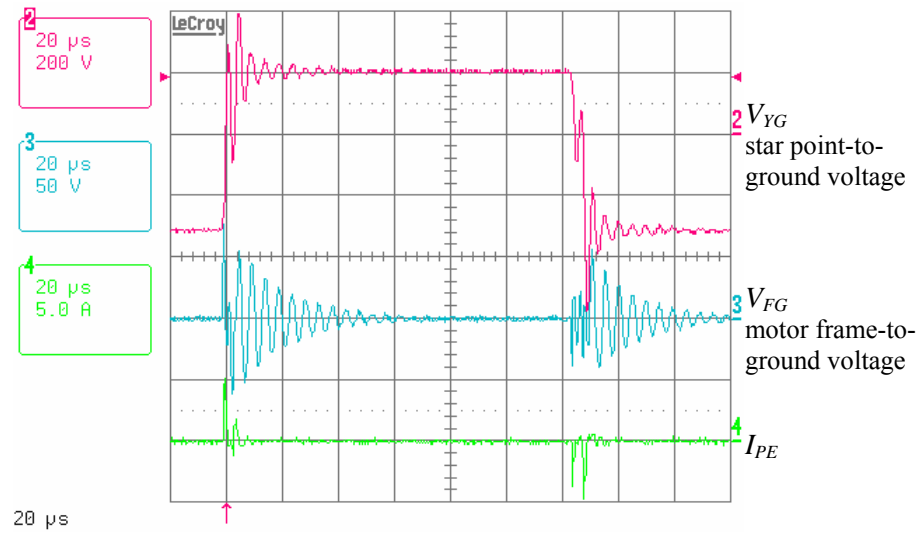

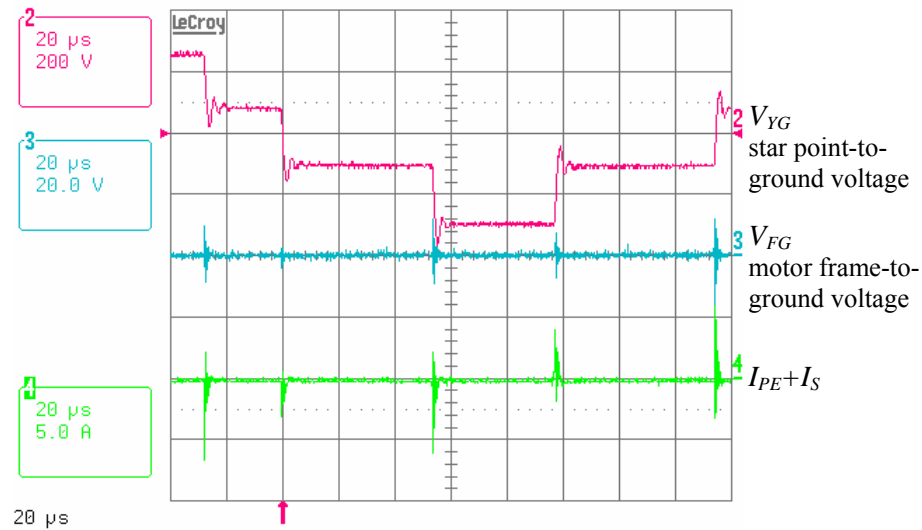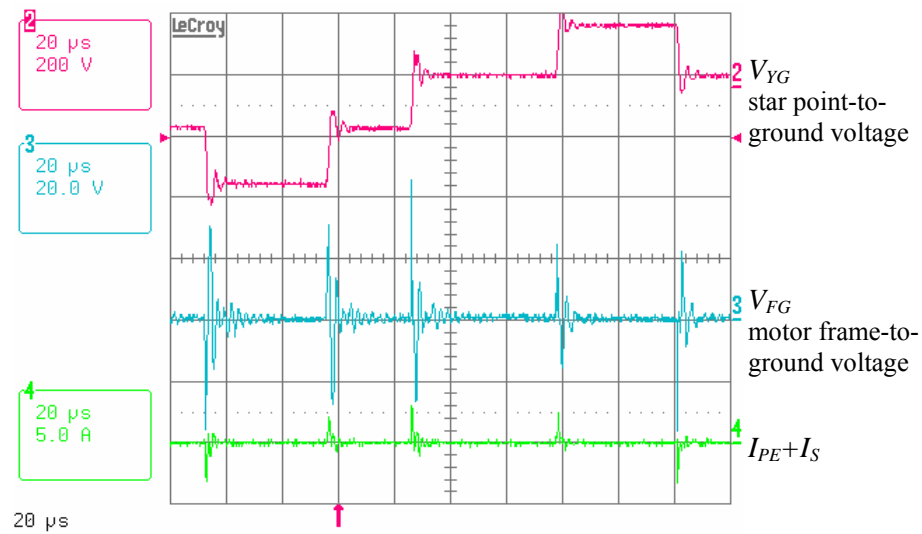Fig. 6-30: Star point-to-ground voltage (pink curve), frame-to-ground voltage (sky-blue curve) and sum of the currents in the PE-wire and the shield (green curve) between the frequency converter and the motor frame measured with an oscilloscope at the grey motor operating at a rotational speed of 2000 rpm. A long (37 m) and unshielded power cable was installed between the motor and the frequency converter.

6.6 Typical time dependence of the voltage and the current during EDM-processes in the static test rig and the resulting energy transfers

During each EDM-test series in the static test rig, undertaken according to a specified measuring procedure (chapter 5.6.3), the voltages $V_{TS}(t)$, between the bearing ball (*BB*) and the cylindrical rolling element (*CRE*), and $V_{RS}(t)$, across the resistor R_S in the EDM-circuit of the static test rig, were monitored and measured with the oscilloscope (Fig. 5-14). Thereby, the function "analog persistence" of the oscilloscope enables to count the number of initiated EDM-processes. A screenshot from the oscilloscope (Fig. 6-31) was stored after each series of EDM-events.
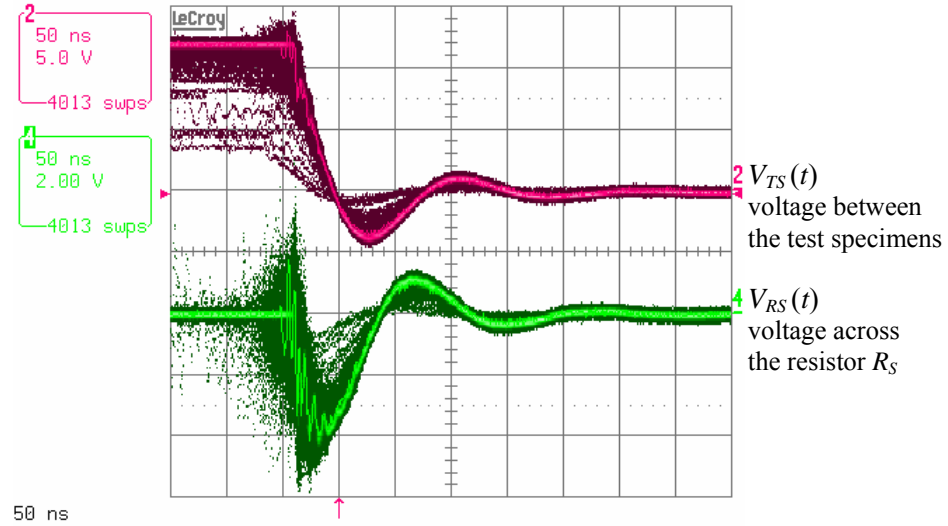
Fig. 6-31: Screenshot from the oscilloscope stored after a series of EDM-processes. The voltages $V_{TS}(t)$ (between the test specimens) and $V_{RS}(t)$ (across the resistor R_S, Fig. 5-14) were measured at the static test rig with the oscilloscope, using the function "analog persistence" to accumulate the voltages and to count the number of EDM-events. The cumulative percentage of the curves is indicated by their brightness.

Monitoring of the time dependence of the voltages $V_{TS}(t)$ and $V_{RS}(t)$ during a test series was necessary for the calculation of the power $P_G(t)$ and the energy $E_G(t)$ transferred to the gap between the test specimens. Fig. 6-31 shows that the progress with time of the voltages $V_{TS}(t)$ and $V_{RS}(t)$ during essentially all EDM-processes was similar, i.e. comparable values of power $P_G(t)$ and energy $E_G(t)$ were transferred to the gap between the test specimens during each EDM-event. The EDM-current $I_{SEDM}(t)$ (Fig. 6-32), flowing in the EDM-circuit of the test rig during an EDM-event, was calculated according to equation (5.8) (chapter 5.5.4) from $V_{RS}(t)$ and the resistance $R_S = 5.8\ \Omega$.

$$I_{SEDM}(t) = -V_{RS}(t)/R_S \qquad\qquad (6.11)$$

Further, the power $P_G(t)$ and the energy $E_G(t)$ (Fig. 6-32) transferred to the gap between the test specimens were calculated from the EDM-current $I_{SEDM}(t)$ according to equations (6.6) and (6.7).

$$P_G(t) = \left| V_{TS}(t) \cdot I_{SEDM}(t) \right| \tag{6.12}$$

$$E_G(t) = \int P_G(t)\, dt = \int \left| V_{TS}(t) \cdot I_{SEDM}(t) \right| dt \tag{6.13}$$
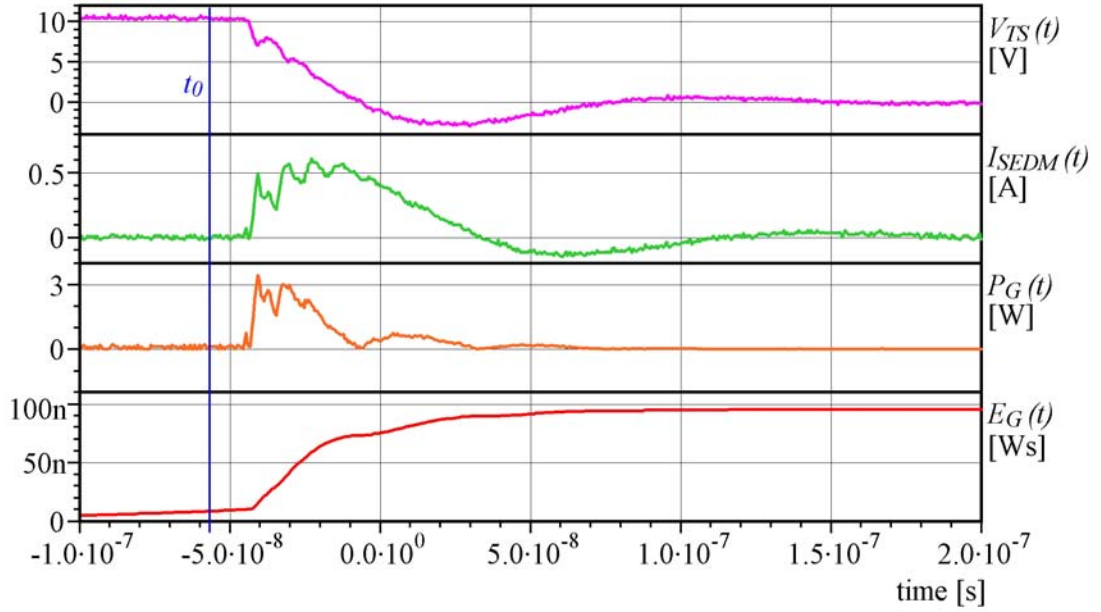
Fig. 6-32: Time dependence of the voltage $V_{TS}(t)$ and the current $I_{SEDM}(t)$ (calculated from $V_{RS}(t)$ (Fig. 6-31) by means of equation (6.11)) during an EDM-event in the static test rig. The power $P_G(t)$ and the EDM-energy $E_G(t)$ transferred to the gap between the test specimens during an EDM-process result from equations (6.12) and (6.13).

The energy stored in the capacitor C_S (Fig. 5-14) just before the initiation of an EDM-process was calculated from the values of C_S and the voltage $V_{TS}(t_0)$ measured at time t_0 just before the beginning of the EDM-event.

$$E_{CS} = \tfrac{1}{2} \cdot C_S \cdot V_{TS}^2(t_0) \longrightarrow E_{CS} = \tfrac{1}{2} \cdot 2.5\ \text{nF} \cdot (12\ \text{V})^2 = 180\ \text{nWs} \tag{6.14}$$

Comparison of the energy E_{CS} stored in the capacitor and the energy fraction of $E_G = 95$ nWs (Fig. 6-32, red curve) reveals that about 53 % of E_{CS} (similar to the fraction of E_{EDM} (55 %) transferred to the bearing, chapter 6.5.4) was consumed in this EDM-process at the gap between the test specimens. The residual fraction of the energy is dissipated at the resistor R_S of the EDM-circuit. The EDM-processes initiated with the static test rig are similar to those occurred in the grey motor, because the time

dependences of the voltages and the currents measured during EDM-processes in both systems, and hence, calculated powers and energies are quite similar (compare Fig. 6-21 and Fig. 6-32). The total energy transfer to the gap during a test series for a single measuring point on the surface of a cylindrical rolling element results from the energy E_G of a single EDM-process multiplied by 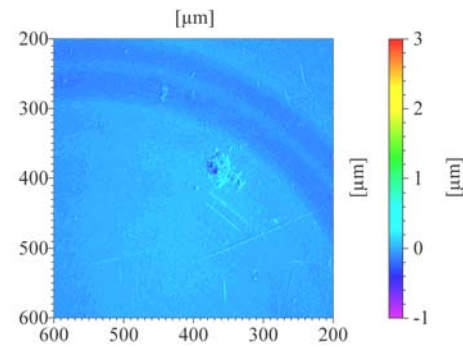the number of EDM-events initiated for each measuring point, because nearly all EDM-events (Fig. 6-31) were initiated at 12 V (supplied by the electric part of the test rig, chapter 5.6.2).

At each measuring point about 4000 EDM-processes were initiated in each of the test series, carried out with different oil samples. At room temperature test series were undertaken at eight measuring points on the surface of a single cylindrical rolling element and at 80 °C four measuring points each were affected by series of EDM-events. Due to the ring heater the working range at the front surfaces of the cylindrical rolling elements was limited, and hence, test series could be undertaken only at the four measuring points in the middle of the virtual grid (Fig. 5-13, chapter 5.6.1). One fixed bearing ball was used for each complete test series made with one oil sample at room temperature or at 80 °C. The damages at the surface of a single bearing ball were generated by the accumulated influence of 4000 EDM-processes initiated at eight measuring points on a cylindrical rolling element (room temperature) or at four measuring points (80 °C). The corresponding total energy transfers resulted to $4000 \cdot 8 \cdot E_G = 3.04$ mWs and $4000 \cdot 4 \cdot E_G = 1.52$ mWs for the test series carried out at room temperature and at 80 °C, respectively.

6.7 Damages at the surfaces of test specimens due to EDM-processes in the static test rig

Each measuring point at the front surfaces of the cylindrical rolling elements was affected by approximately 4000 EDM-processes. Thus, in the majority of cases, no and otherwise only very small damages were found at these measuring points by means of a contactless optical profile meter (µScan, chapter 5.7). The structures of the surfaces at those regions of the bearing balls affected by about 32000 (room temperature) and 16000 (80 °C) EDM-processes in the static test rig were analysed also by means of the µScan. The results are presented in Fig. 6-33 (room temperature) and Fig. 6-34 (80 °C), whereby the structural changes at the surface in relation to the undisturbed (ideal) surface of the bearing ball were visualised by means of software implemented in the µScan. The surface damages generated by EDM-processes appeared to be significantly different depending on the oil samples used. The most drastic damages at the surfaces could be observed for the test series carried out at room temperature using the oil

samples 218 and 345, whereas essentially no influence of EDM treatment as noticed in the result for the oil sample 214 (numbers of oil samples according to Tab. 4-1 in chapter 4.2). During the test series undertaken at 80 °C, about half the number of EDM-events were initiated in comparison to the tests at room temperature, therefore, the damages generated at 80 °C could be expected to be less pronounced as evident from comparison between Fig. 6-33 and Fig. 6-34.

air

oil 001

oil 002

oil 214

oil 215

oil 216

oil 217

oil 218

oil 219

oil 220

oil 221

oil 222

oil 223

oil 345
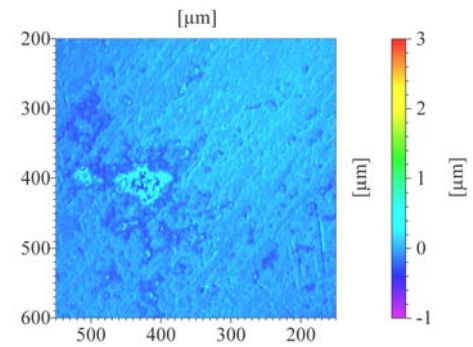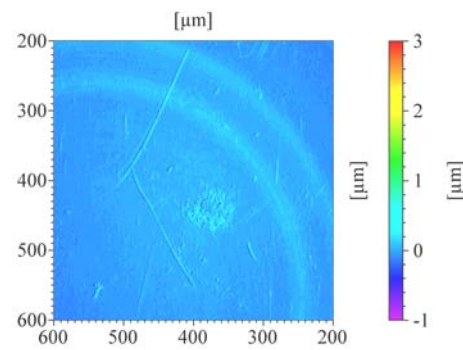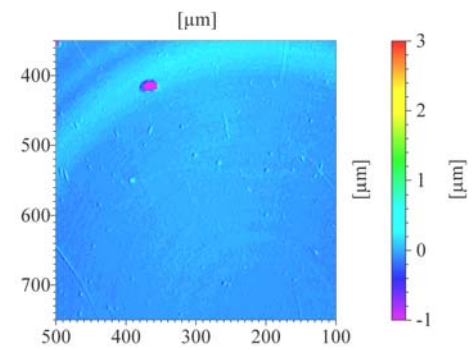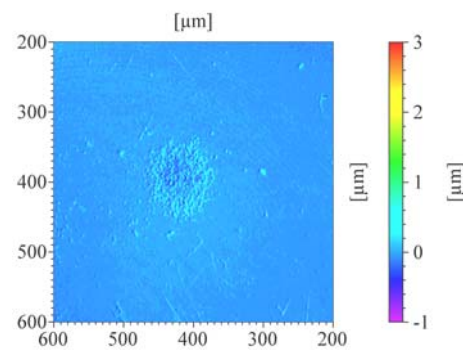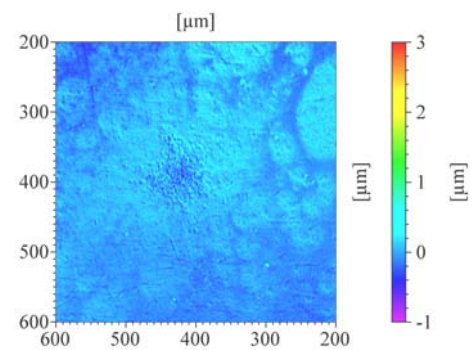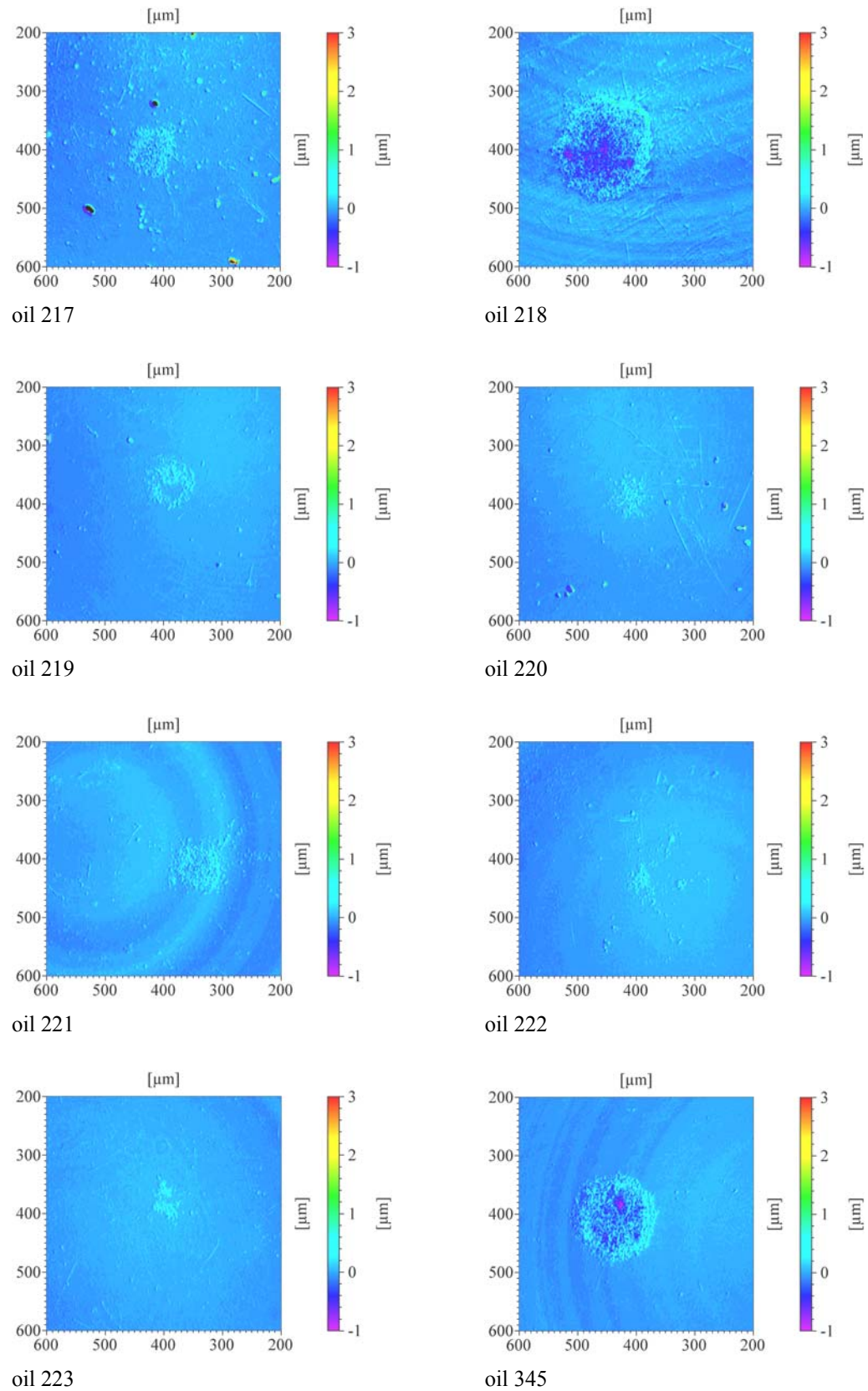
Fig. 6-33: Top views of the structures at the surfaces of bearing balls analysed with the μScan after approximately 32000 EDM-processes initiated at room temperature using different oil samples. The color scales at the right side of the pictures denote the elevations and cavities in relation to the ideal spherical shape of the bearing ball. The oil samples are denoted by the numbers according to (Tab. 4-1).

air
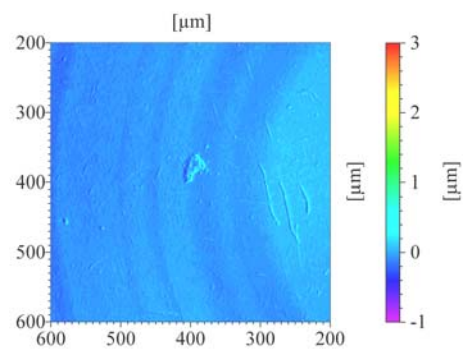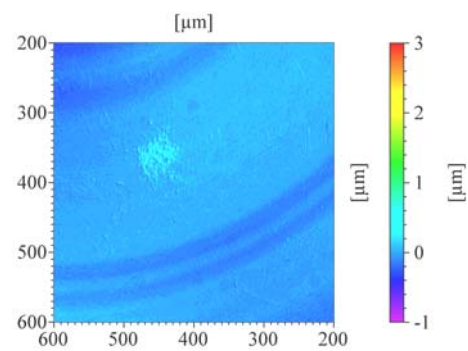
oil 001
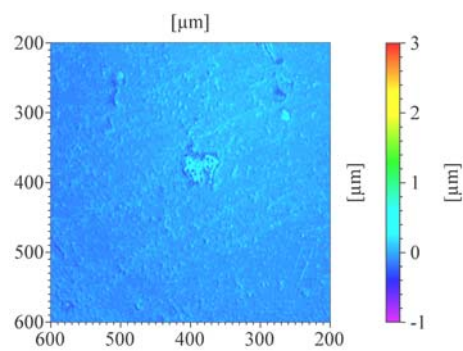
oil 002
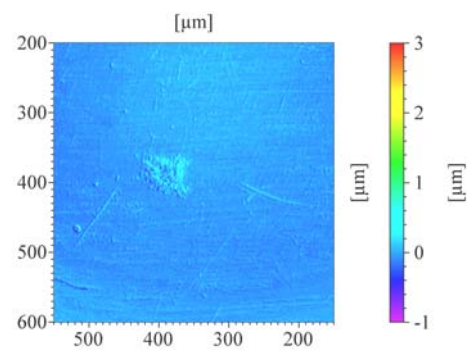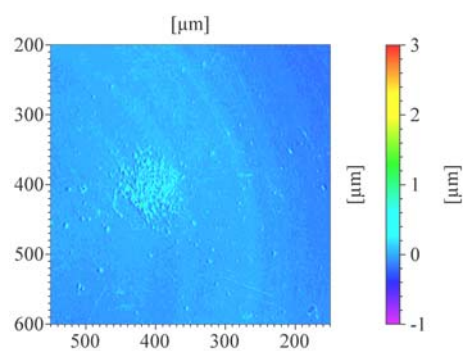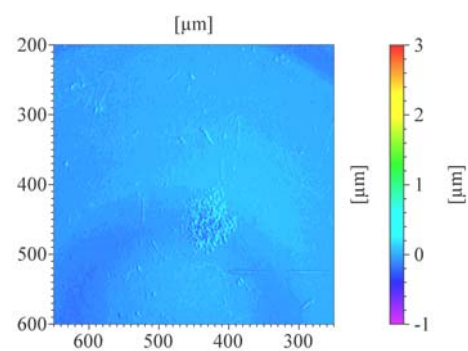
oil 214
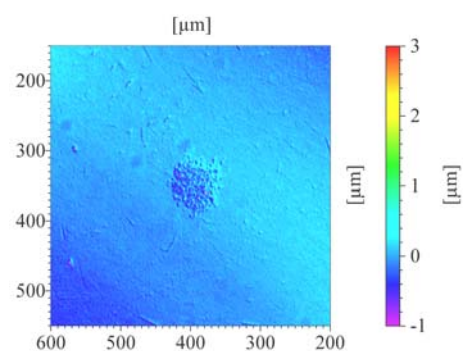
oil 215
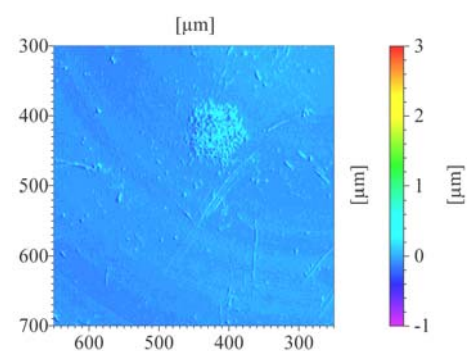
oil 216

oil 217

oil 218
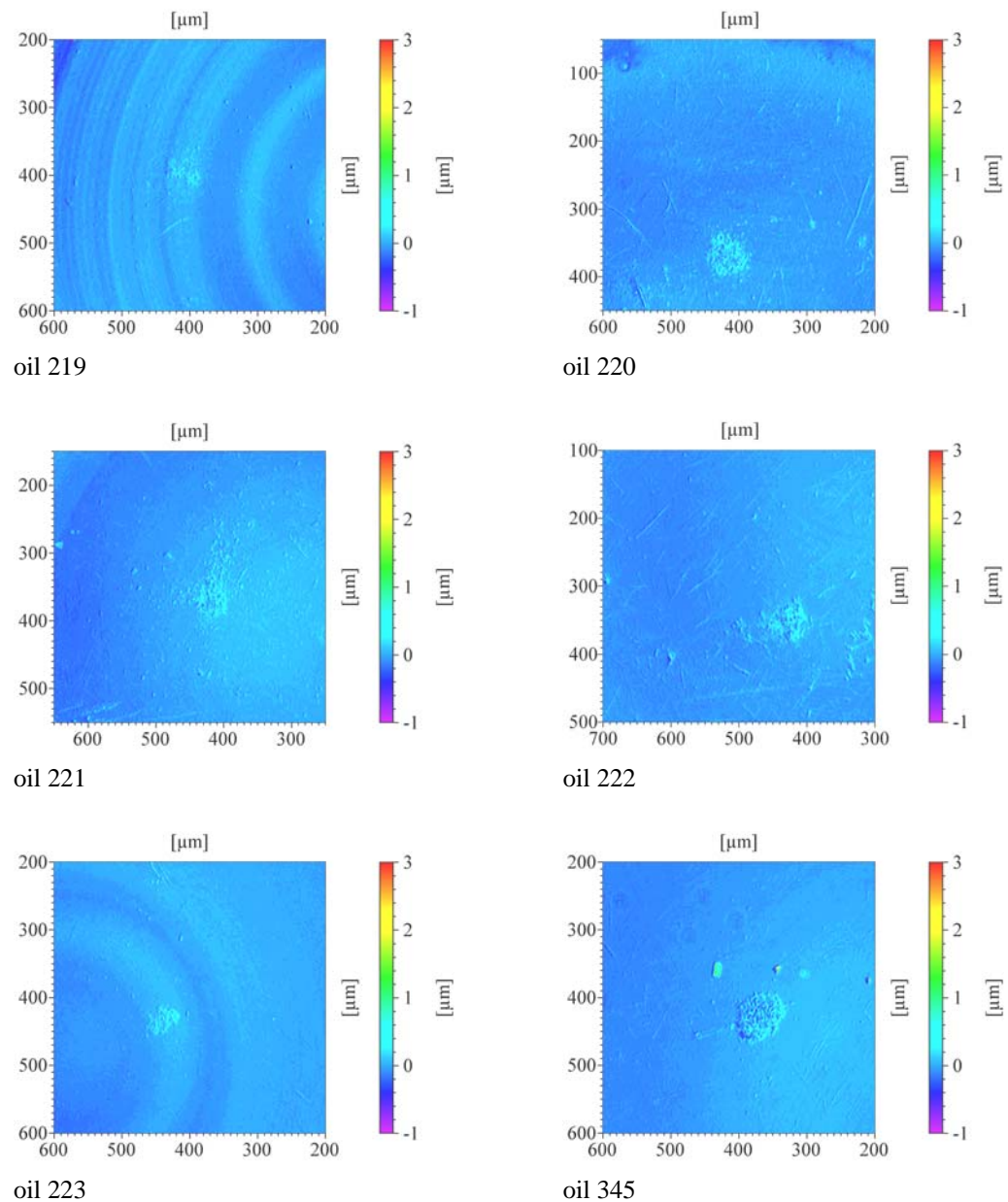
Fig. 6-34: Top views of the structures at the surfaces of bearing balls analysed with the µScan after approximately 16000 EDM-processes initiated at 80 °C using different oil samples. The color scales at the right side of the pictures denote the elevations and cavities in relation to the spherical shape of the ideal bearing ball. The oil samples are denoted by the numbers according to (Tab. 4-1).

The regions at the surfaces of the bearing balls damaged by EDM-processes were mathematically enclosed each by the smallest possible ellipse, for further analysis. The calculated areas of these ellipses characterising the damaged regions are shown in Fig. 6-35 and Fig. 6-36 for the test series at room temperature and at 80 °C, respectively. The largest areas (ellipses) at the bearing balls comprising damages were obtained at room temperature with the oil samples 218, 222 and 345, whereby nearly the whole areas were damaged using sample 218 and 345, but undamaged regions were found within the ellipse enclosing the damages generated at the bearing ball using oil

sample 222. At room temperature as well as at 80 °C, only small regions were damaged at the surfaces of those bearing balls subjected to EDM-processes in air or in the presence of the oil 001, 002, 214, 220 and 223.

Moreover, the structures of the generated damages were investigated with respect to their distribution of altitudes. Therefore, the partial areas of the ellipses lying between certain altitudes were determined from the analysis data delivered by the μScan. The percentages of the partial areas in relation to the total area of the ellipse were calculated and added up for each oil samples (Fig. 6-37 and Fig. 6-38). The greatest percentage of the damaged areas are in the altitude range from 0 μm to 0.5 μm (elevations) and in the altitude range from 0 μm to -0.5 μm (cavities), whereby the partial areas in the positive altitude range are larger. Furthermore, the volumes of the elevations within the damaged regions (ellipses) of the bearing balls accumulated over all test series with a single oil are larger than the accumulated volumes of the cavities. This applies both for the test series at room temperature and at 80 °C (Fig. 6-39 and Fig. 6-40).
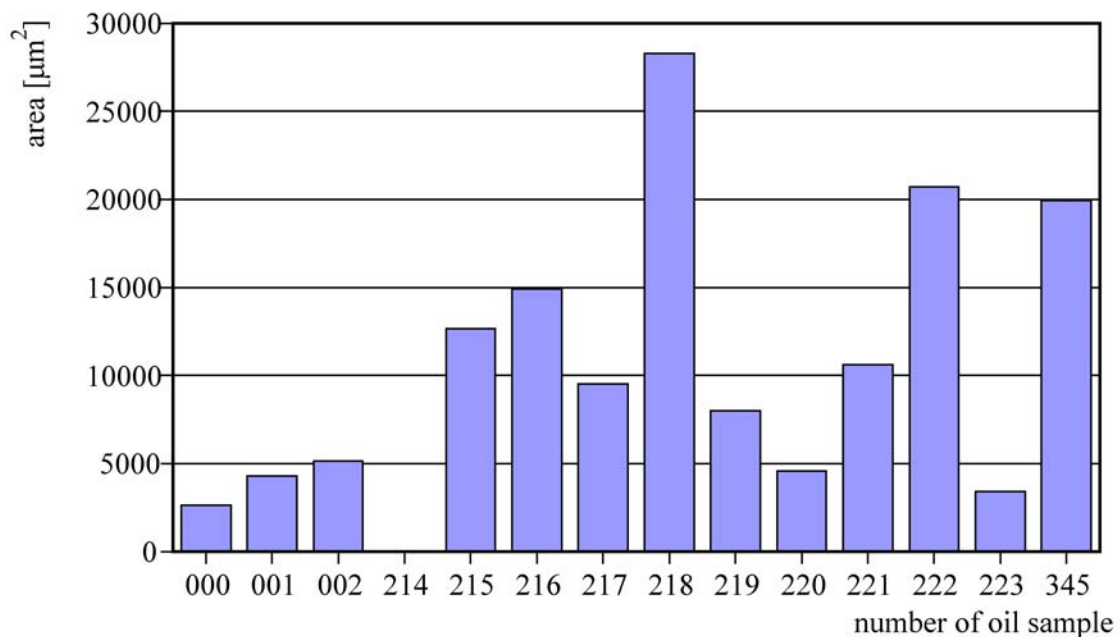
Fig. 6-35: Areas of the smallest ellipses enclosing those regions at the surfaces of the bearing balls, which were damaged by approximately 32000 EDM-processes at room temperature using different oil samples (numbers according to Tab. 4-1) or carrying out in air (000).
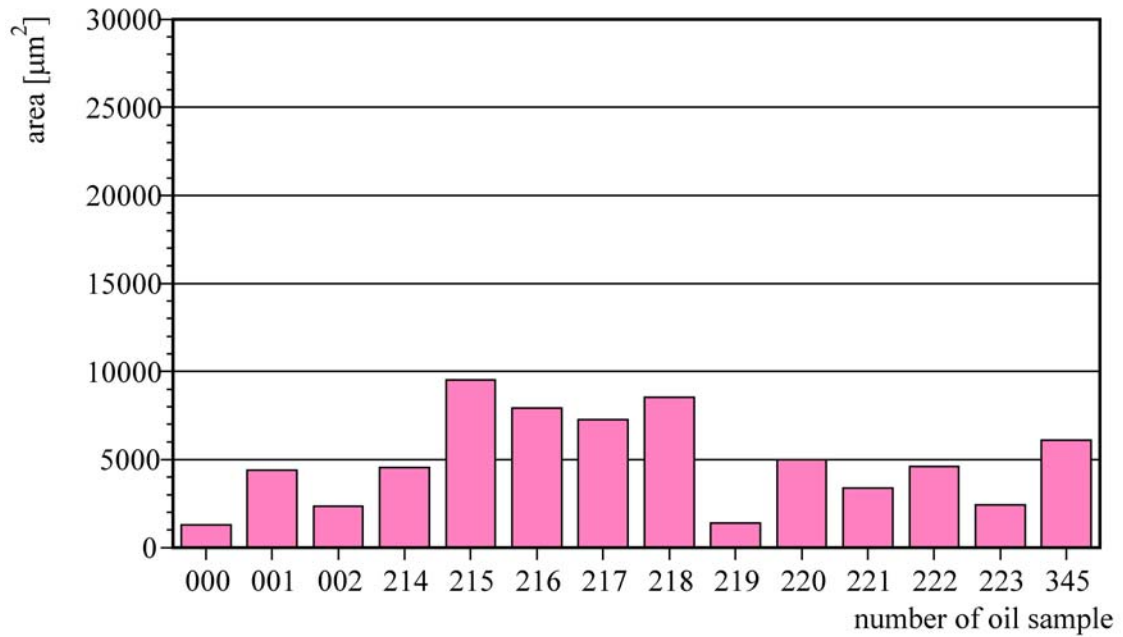
Fig. 6-36: Areas of the smallest ellipses enclosing those regions at the surfaces of the bearing balls, which were damaged by approximately 16000 EDM-processes at 80 °C using different oil samples (numbers according to Tab. 4-1) or carrying out in air (000).
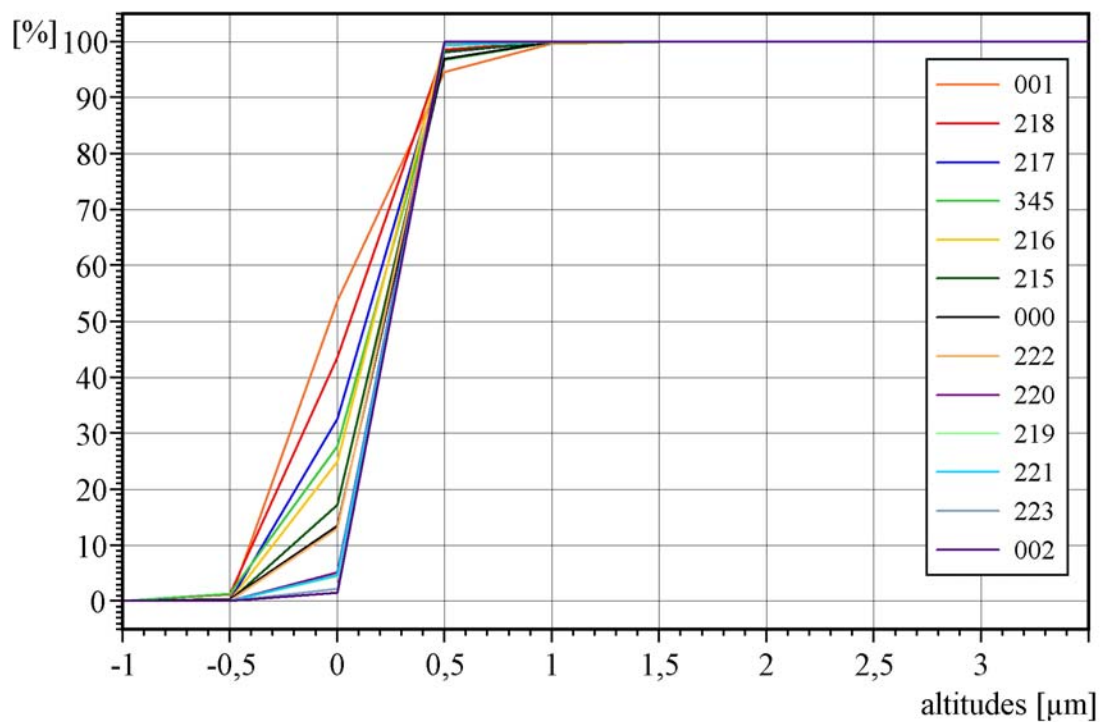
Fig. 6-37: Percentages of the partial areas lying between certain altitudes in relation to the total areas of damage for damages generated by approximately 32000 EDM-processes at room temperature using different oil samples (numbers according to Tab. 4-1) or carrying out in air (000).
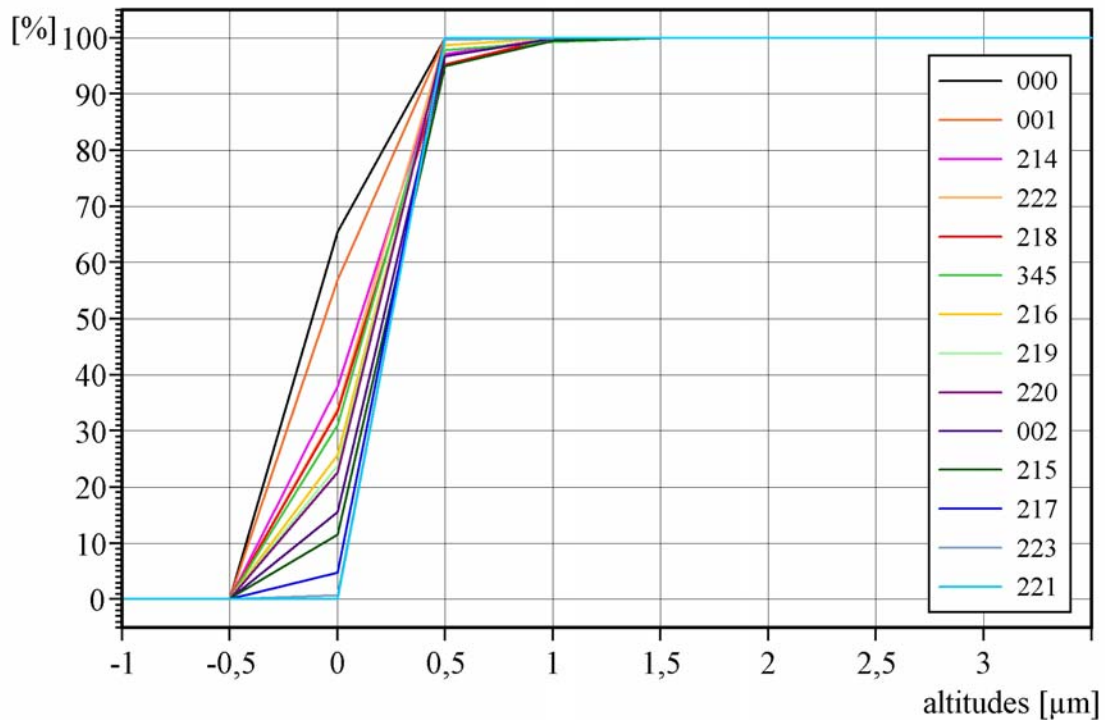
Fig. 6-38:   Percentages of the partial areas lying between certain altitudes in relation to the total areas of damage for damages generated by approximately 16000 EDM-processes at 80 °C using different oil samples (numbers according to Tab. 4-1) or carrying out in air (000).
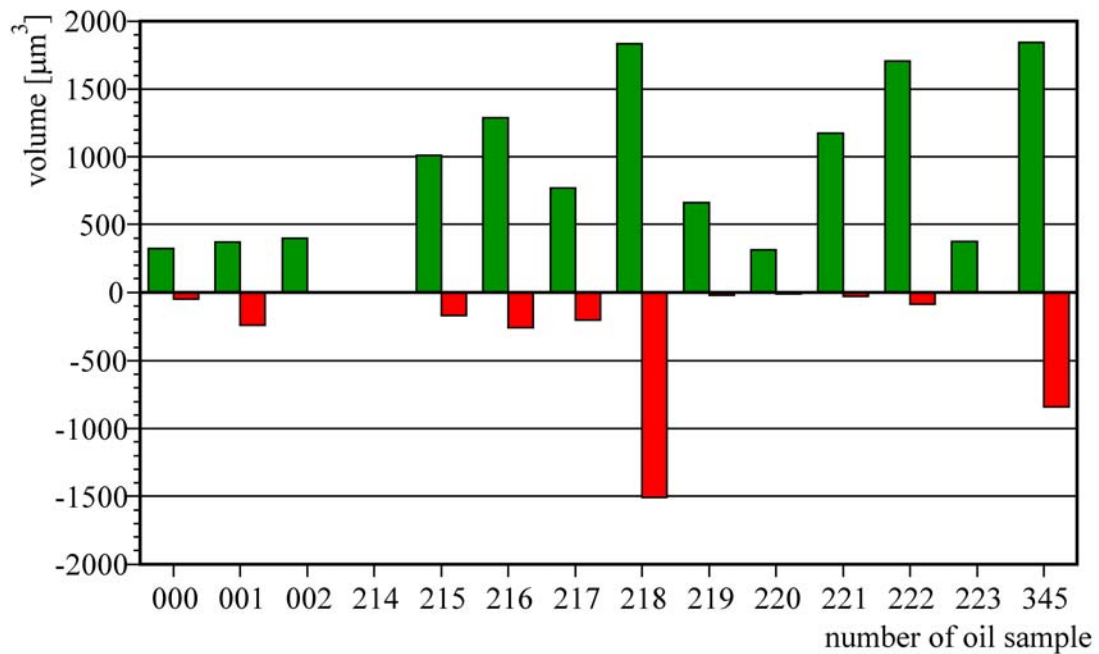
Fig. 6-39:   Accumulated volumes of elevations (green bars) and cavities (red bars) within the damaged regions (ellipses) at the surfaces of bearing balls affected by approximately 32000 EDM-events at room temperature using different oil samples (numbers according to Tab. 4-1) or carrying out in air (000).
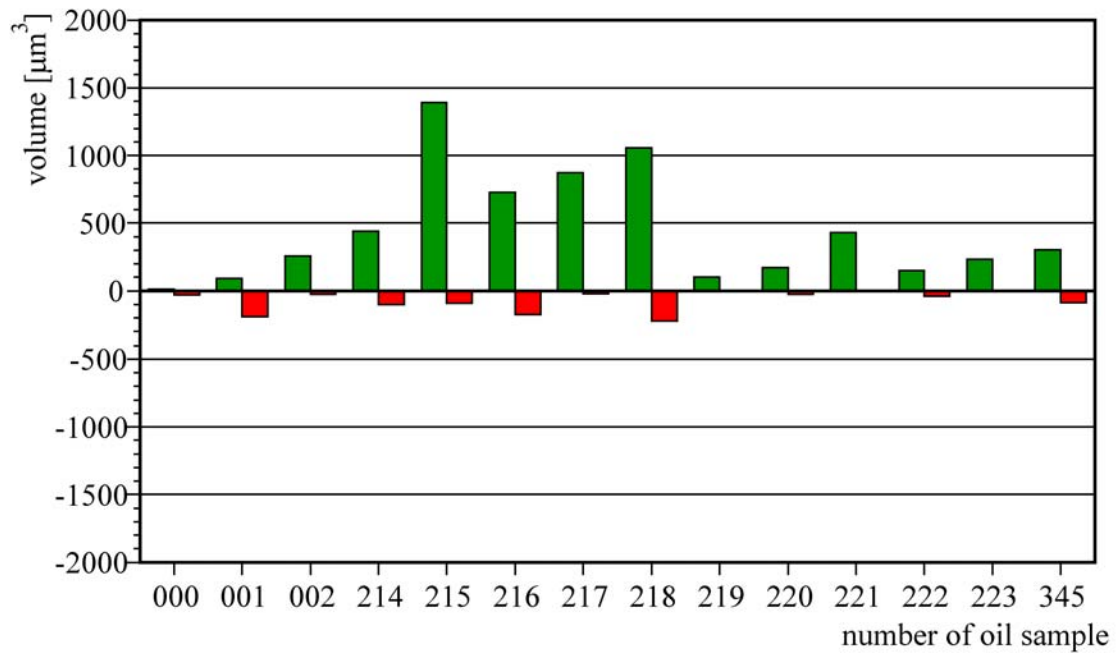
Fig. 6-40: Accumulated volumes of elevations (green bars) and cavities (red bars) within the damaged regions (ellipses) at the surfaces of bearing balls affected by approximately 16000 EDM-events at 80 °C using different oil samples (numbers according to Tab. 4-1) or carrying out in air (000).
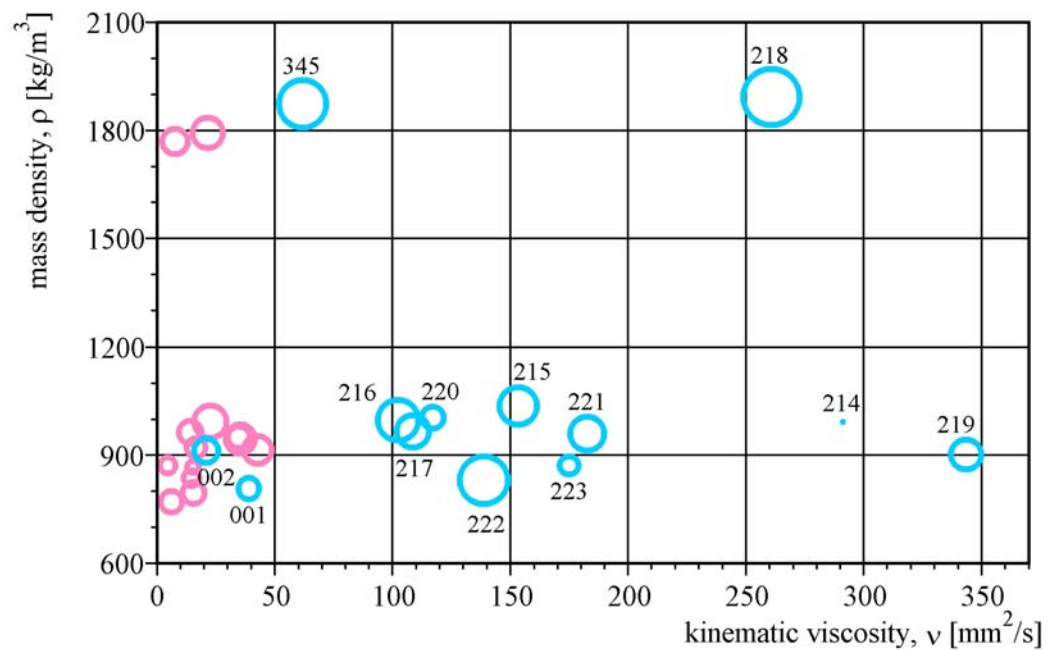
Fig. 6-41: Correlation between the sizes of damaged regions at bearing balls and the mass densities and kinematic viscosities of the oil samples (numbers according to Tab. 4-1) used for EDM-test series. The areas of the circles are proportional to the damaged regions (ellipses) at the surfaces of the bearing balls after approximately 32000 EDM-events initiated at room temperature (sky-blue circles) or 16000 EDM-events at 80 °C (pink circles). The mid points of the circles indicate the viscosities and mass densities of the oil samples at the respective temperature. A close-up of the viscosity range from $0 \text{ mm}^2/\text{s}$ to $45 \text{ mm}^2/\text{s}$ is shown in Fig. 6-42.
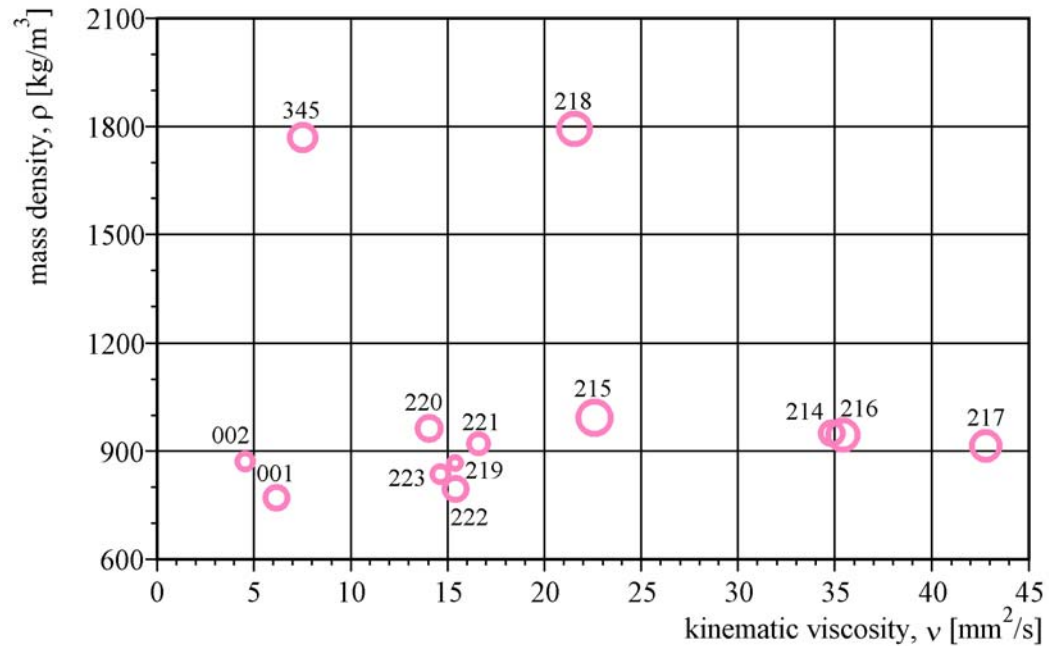
Fig. 6-42: Correlation between the sizes of damaged regions at bearing balls and the mass densities and kinematic viscosities of the oil samples (numbers according to Tab. 4-1) used for EDM-test series. The areas of the circles are proportional to the damaged regions (ellipses) at the surfaces of the bearing balls after approximately 16000 EDM-events initiated at 80 °C. The mid points of the circles indicate the viscosities and mass densities of the oil samples at 80 °C.
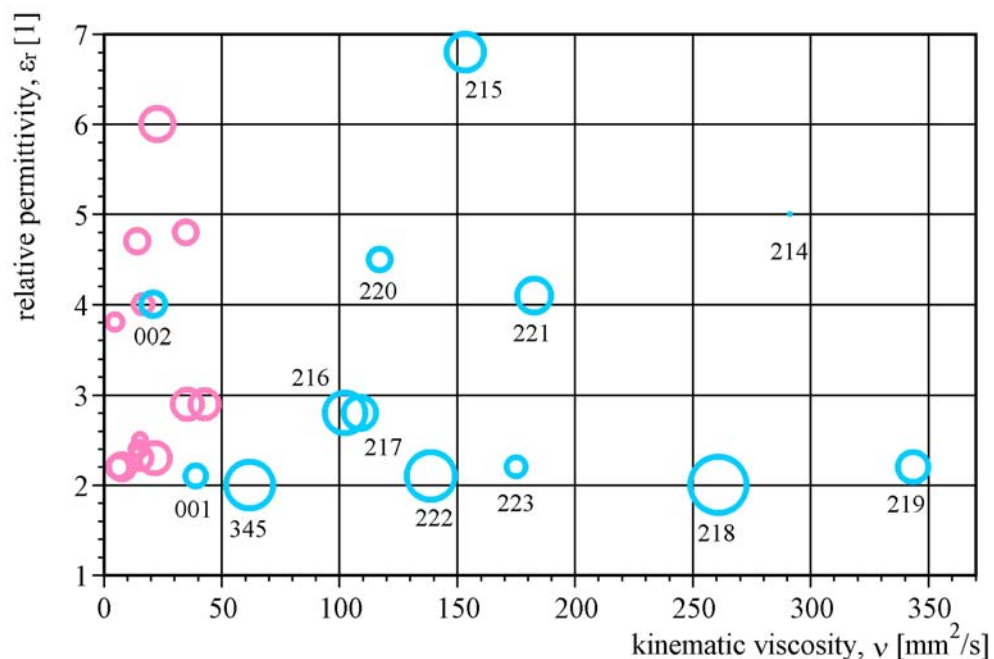
Fig. 6-43: Correlation between the sizes of damaged regions at bearing balls and the relative permittivities and kinematic viscosities of the oil samples (numbers according to Tab. 4-1) used for EDM-test series. The areas of the circles are proportional to the damaged regions (ellipses) at the surfaces of the bearing balls after approximately 32000 EDM-events initiated at room temperature (sky-blue circles) or 16000 EDM-events at 80 °C (pink circles). The mid points of the circles indicate the viscosities and relative permittivities of the oil samples at the respective temperature. A close-up of the viscosity range from 0 mm^2/s to 45 mm^2/s is shown in Fig. 6-44.

Fig. 6-44: Correlation between the sizes of damaged regions at bearing balls and the relative permittivities and kinematic viscosities of the oil samples (numbers according to Tab. 4-1) used for EDM-test series. The areas of the circles are proportional to the damaged regions (ellipses) at the surfaces of the bearing balls after approximately 16000 EDM-events at 80 °C. The mid points of the circles indicate the viscosities and relative permittivities of the oil samples at the respective temperature.
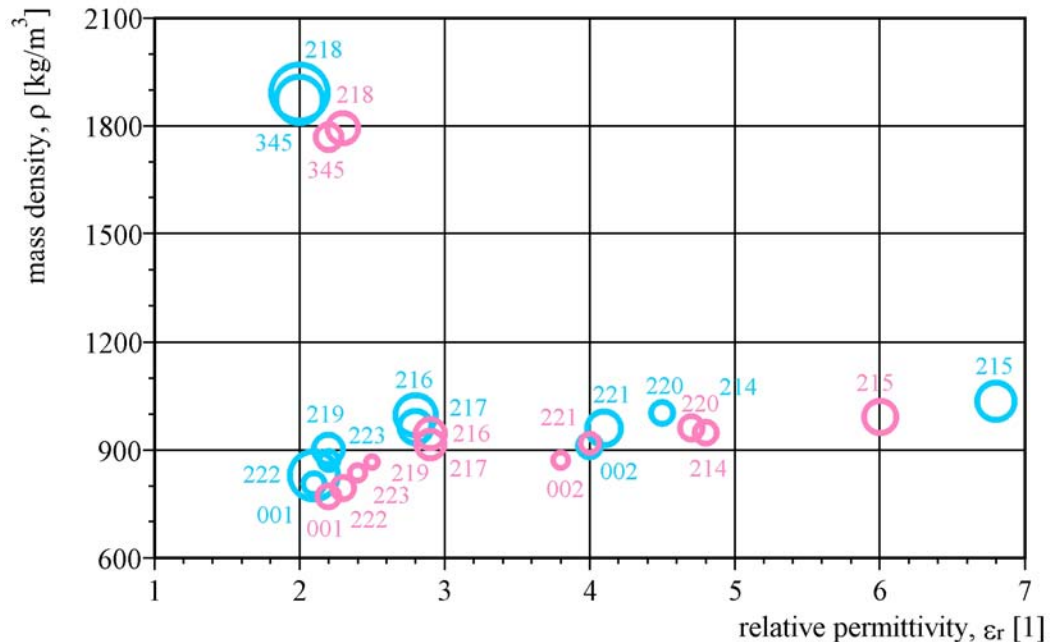
Fig. 6-45: Correlation between the sizes of damaged regions at bearing balls and the mass densities and relative permittivities of the oil samples (numbers according to Tab. 4-1) used for EDM-test series. The areas of the circles are proportional to the damaged regions (ellipses) at the surfaces of the bearing balls after approximately 32000 EDM-events initiated at room temperature (sky-blue circles) or 16000 EDM-events at 80 °C (pink circles). The mid points of the circles indicate the relative permittivities and mass dendities of the oil samples at the respective temperature.

The correlation between the sizes of damaged regions (ellipses) and the mass densities and kinematic viscosities of the oil samples used in the test series is illustrated in Fig. 6-41 and Fig. 6-42. It is noticeable that the greatest damages at the bearing balls were generated using the oil samples (218 and 345) with the highest mass densities, whereby no distinct influence of the kinematic viscosity could be observed. No systematic correlation between the sizes of damaged regions (ellipses) and the relative permittivites and kinematic viscosities of the oil samples used in the test series are shown by the measurement results (Fig. 6-43 and Fig. 6-44). According to Fig. 6-41, Fig. 6-45 exhibits that, the oil samples (218 and 345) with the highest mass densities caused the greatest damages, whereby no distinct influence of the relative permittivity could be observed. To verify these tendencies, further test series and also a higher number of EDM-events should be carried out with the static test rig.

Further, the chemical properties of the oil samples 218 and 345 must be taken into account. Both oils are perfluor-polyethers. Therefore, the generation of hydrofluoric acid (HF) due to the EDM-energy may be possible. Hence, chemical etching additionally may damage the surfaces of the test specimens. The clarification of this possible effect needs specific investigations.

The local distribution of elevations and cavities over certain regions at the affected surfaces of the bearing balls indicates that the initiated EDM-processes are not restricted to the region of the smallest gap between the test specimens but spread over a certain area. A distribution of EDM-events over a certain region was observed by photography of EDM-events (following chapter).

6.8   Photographs of EDM-events

EDM-events were initiated with the static test rig in air (no oil between the test specimens) applying a DC voltage of 120 V across the gap between the test specimens, to be able to catch photographically the generated sparks with a monochrome high speed digital camera (chapter 5.8). As the EDM-energy depends on the square of the applied voltage (equation (2.3)), the energy available during these EDM-processes initiated for photography was about 100 times greater than the energy used during the test series under realistic conditions with an applied DC voltage of 12 V (chapter 5.6.2).

The duration of EDM-events is typically shorter than 100 ns (Fig. 6-32), therefore the photographically recorded sparks are available only on single frames. Six typical photographs of such sparks are shown in Fig. 6-46. It is obvious that the sparks do not

appear on a single position (smallest gap width between test specimens) but are distributed over a certain region of the gap. This observation is in agreement with the detected local distribution of cavities and elevation on the surfaces of EDM-affected bearing balls, indicating that EDM-processes under realistic conditions are also distributed over certain areas of the gaps.
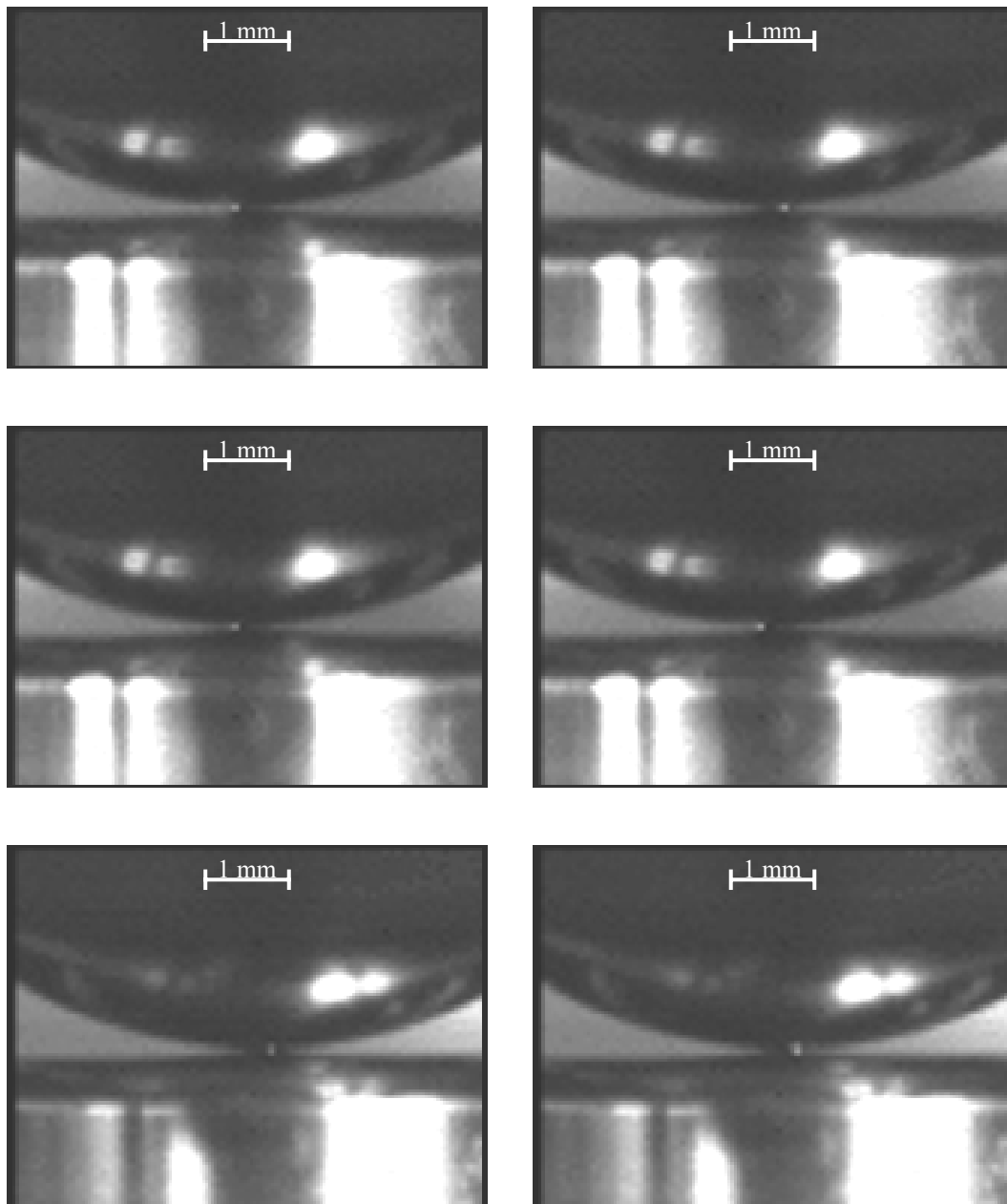
Fig. 6-46: Photographs of sparks occurring between a bearing ball and a cylindrical rolling element during EDM-events initiated with the static test rig in air using a DC voltage of 120 V across the gap between test specimens. The photographs were taken with a monochrome high speed digital camera.

7   Supposed new counter measures against bearing damages caused by electrical current passage

Different state-of-the-art counter measures against electrical current passage through bearings have been discussed in chapter 2.4. Thereby, brushes need enhanced maintenance, conductive greases increase the wear in the bearings or work only for limited periods, and several types of filters, chokes, transformers or different mitigation techniques may to some extent reduce electric current passage and hence bearing damage. Coated bearings are effective against circulating currents, but they are generally not able to break high-frequency dv/dt-currents because of the large capacitance of their insulating layers. Circulating currents as well as high-frequency dv/dt-currents are avoided by hybrid bearings, but the motor shaft-to-frame voltage still exists and may damage the bearings of the driven machine.

Two novel counter measures against bearing damages due to electrical current passage are described in the next sections. First, a method for the compensation of the motor shaft-to-frame voltage is presented, which was initiated within a preceding dissertation project conducted by G. Preisinger [2]. This method was applied for a patent by AB SKF, Göteborg, Sweden, and has been published recently in the meantime (EP 1 445 850 A1) [40]. During this work, a prototype based on this method was designed and constructed. The effectiveness of the set-up was investigated and could be improved substantially during several steps of development. The second counter measure, developed in the present work, prevents the generation of the motor shaft-to-frame voltage by means of an earth-balanced power supply of the motor. This method was also filed for a patent by AB SKF.

7.1   Compensation of the motor shaft-to-frame voltage

Except for circulating currents, which are not affected by this technique, bearing damages are mainly generated by EDM-currents, if the bearings are in the full-film lubrication regime and a motor shaft-to-frame voltage (V_{MSF}) is present. It is common knowledge that the EDM-energy transferred to the contact area in a bearing is proportional to the square of the motor shaft-to-frame voltage, which is available just at the moment when an EDM-process starts (equation (2.3) in chapter 2.3). Thus, it is obvious that, e.g., a reduction of V_{MSF} by 50 percent would reduce the available EDM-energy by a factor of 4. Hence, also bearing damages could be decreased significantly, if the motor shaft-to-frame voltage is reduced. According to the method discussed here, this reduction of V_{MSF} is accomplished by generating a voltage signal,

which is in opposite phase to the initial motor shaft-to-frame voltage and feeding this inverted voltage to the motor shaft through a cylindrical air capacitor [40]. This air capacitor C_A is formed by two coaxial cylinders and an air gap between these cylinders. The inner cylinder is mounted at the motor shaft as well as connected electrically to the shaft. Whereas the inner cylinder rotates with the motor shaft, the outer cylinder is fixed at the motor frame, but electrically insulated from the frame. Hence, the inverted voltage can be coupled to the rotating motor shaft via the fixed outer cylinder of C_A.
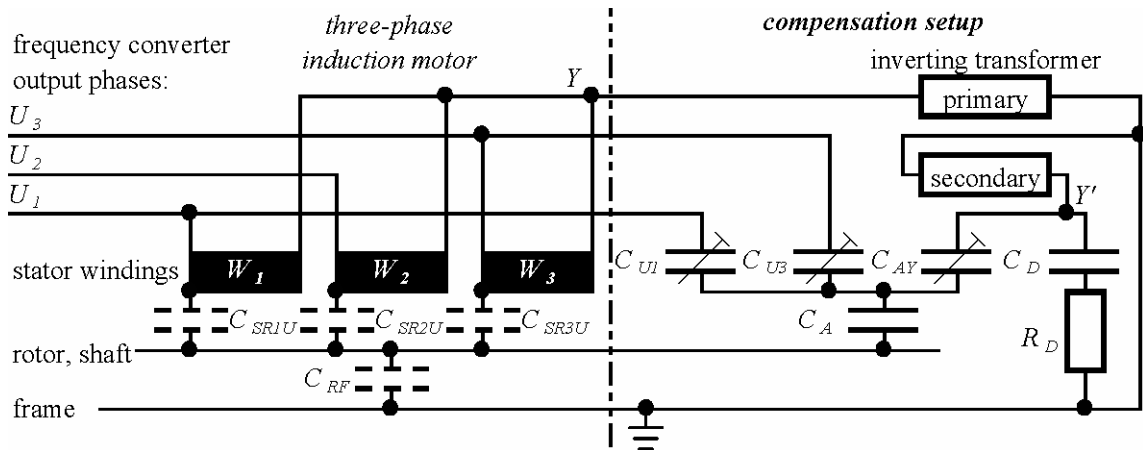
Fig. 7-1:   Schematic diagram of the set-up for compensation of the motor shaft-to-frame voltage. The stray capacitance C_{RF} and C_{SR1U}, C_{SR2U}, and C_{SR3U} illustrate the capacitive coupling between the rotor and the motor frame, and between the rotor and those ends of stator windings, which are connected to the phase voltages (compare Fig. 6-19, chapter 6.5.1). The inverted voltage (applying between Y' and the motor frame) is generated by a transformer from the voltage between the motor star point Y and the motor frame, adjusted by the tunable capacitor C_{AY} and coupled to the motor shaft through the cylindrical air capacitor C_A. By means of the tunable capacitors C_{U1} and C_{U3} the capacitive coupling between the stator windings W_1 and W_3, respectively, and the rotor can be adjusted individually to match the capacitive coupling between the stator winding W_2 and the rotor. The damping capacitor C_D and resistor R_D are installed to minimise the transients occurring after each voltage steps.

To produce the inverted voltage, the star point-to-frame voltage (V_{YF}) is picked up at the star point (Y) of the motor and inverted by a broadband inverting transformer, manufactured by Nejdl & Pold Mechatronic OEG, Vienna (Fig. 7-1). On the one hand, this transformer must be able to transmit the pulse-shaped star point-to-frame voltage, which has a switching frequency of typically a few kilohertz and very steep edges (several 100 V/μs), and, on the other hand, the transformer must not be saturated by the superimposed 150 Hz sine wave component, which is caused by the three-phase rectifier of the frequency converter. Therefore, to verify proper transformer operation, the voltages V_{YF} (between Y and the motor frame in Fig. 7-1) and $V_{Y'F}$ (inverted voltage between Y' and the motor frame) were measured at the grey motor by means of an oscilloscope, whereby the secondary winding of the transformer was only connected to the damping capacitor C_D and resistor R_D. It is obvious that $V_{Y'F}$ (green curve in

Fig. 7-2) comprised a 150 Hz component in opposite phase to the 150 Hz component of V_{YF} (pink curve). The sum (orange curve) of both voltages, V_{YF} and $V_{Y'F}$, does not show this 150 Hz component. Thus, the ripple voltages at the motor star point is properly transmitted and inverted by the broadband transformer, as necessary for optimal compensation of the motor shaft-to-frame voltage. A damping capacitor C_D and resistor R_D were connected to the secondary winding of the inverting transformer to minimise the transients occurring at $V_{Y'F}$ after each voltage step at V_{YF}.
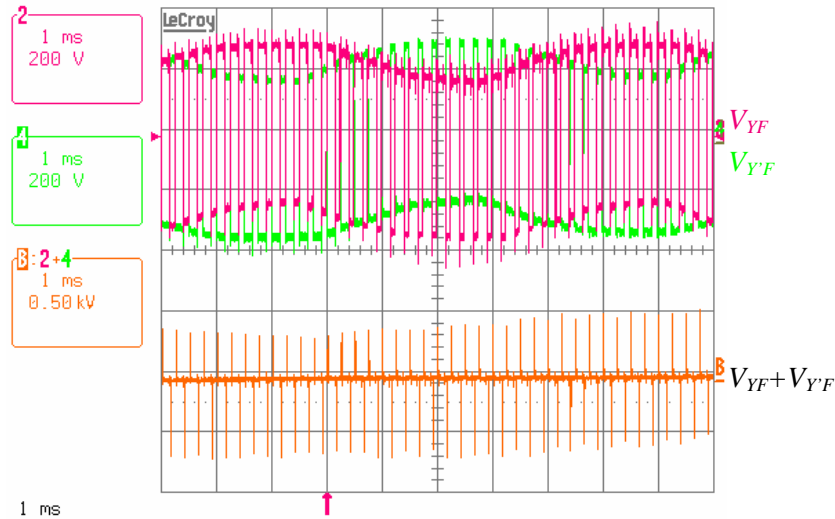
Fig. 7-2:   Time dependence of the star point-to-frame voltage V_{YF} (pink curve) and the inverted voltage $V_{Y'F}$ (green curve) measured between the points Y and Y' ,respectively, and the motor frame according to Fig. 7-1. The orange curve is the sum of V_{YF} and $V_{Y'F}$.

Prior to the activation of the compensation circuit, the voltages V_{YF} and V_{MSF} were measured at the grey motor under normal operating conditions, i.e., without feeding a compensation signal through the air capacitor (Fig. 7-3). Except for the breakdown of the motor shaft-to-frame voltage during an EDM-process (marked with a yellow arrow), the different voltage steps at V_{MSF} are generated by the capacitive coupling of V_{YF} to the motor shaft through the stray capacitances C_{SR1U}, C_{SR1Y}, C_{SR2U}, C_{SR2Y}, C_{SR3U} and C_{SR3Y} as, discussed in chapter 6.5.1. Thereby, the coupling from the different stator windings W_1, W_2 and W_3, respectively, generates voltages steps at V_{MSF} of different step heights because of the differences in the respective stray capacitances (Tab. 6-2). In contrast, the inverted voltage ($V_{Y'F}$), which is generated from the star point-to-frame voltage (V_{YF}), exhibits voltage steps of uniform height, according to the shape of V_{YF}. Thus, to achieve optimal compensation results, the motor shaft-to-frame voltage (V_{MSF}) has to be modified to show uniform voltage step heights before feeding the inverted voltage through the air capacitor.

At first, those stator winding (and corresponding phase voltage) had to be identified which generated the largest voltage steps at V_{MSF}. Therefore, two of the three phase voltages and the motor shaft-to-frame voltage were measured with an oscilloscope simultaneously at the grey motor, to correlate the voltage steps at the phase voltages with the corresponding voltage steps at V_{MSF} (Fig. 7-4).

Fig. 7-3:   Time dependence of the star point-to-frame voltage V_{YF} (pink curve) and the motor shaft-to-frame voltage V_{MSF} (sky-blue curve) measured during normal operation of the grey motor. In addition to the voltage steps at V_{MSF} caused by the transients of V_{YF}, an EDM-event (marked with a yellow arrow) was observed.
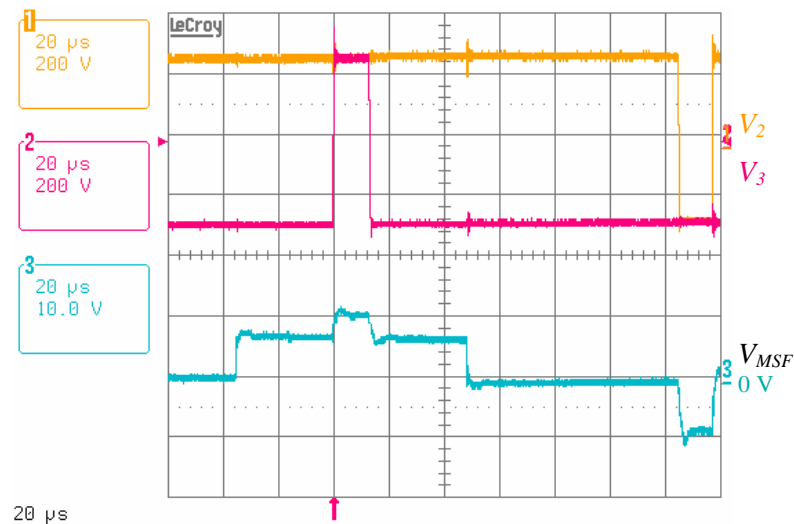
Fig. 7-4:   Two phase voltages, V_2 (yellow curve) and V_3 (pink curve), and the motor shaft-to-frame voltage V_{MSF} (sky-blue curve) measured at the grey motor. In addition to the voltage steps at V_{MSF} caused by the transients of the phase voltages, an EDM-event (marked with a yellow arrow) was observed.

The highest voltage steps were generated by the phase voltage V_2 and the corresponding stray capacitance (chapter 6.4.2) between the stator winding W_2 and the rotor, for the motor considered here. Hence, the smaller voltage step heights produced by V_1 and V_3,

respectively, could be adjusted individually by means of the tunable capacitors C_{U1} and C_{U3} in series with the cylindrical air capacitor C_A (Fig. 7-1) to achieve a uniform step height at V_{MSF} (Fig. 7-5). During this procedure, the inverted voltage $V_{Y'F}$ was not connected to the air capacitor. Subsequently, the voltages, V_{MSF} and V_{YF} were measured with an oscilloscope for verification (Fig. 7-6).
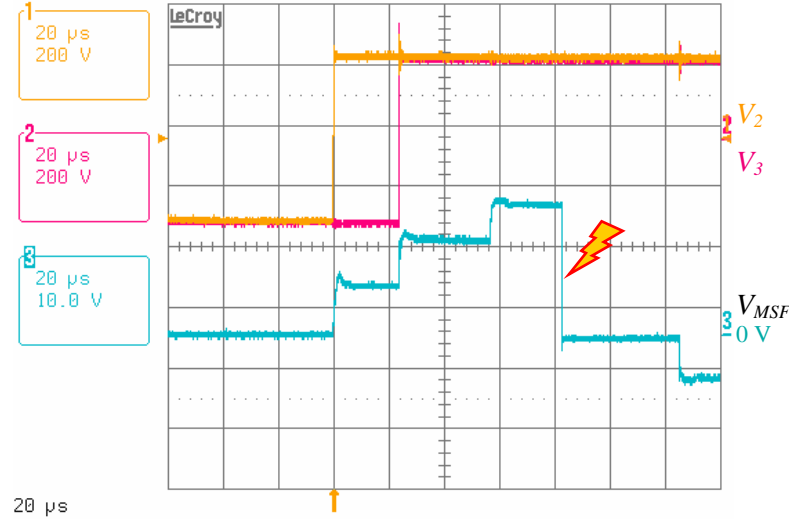
Fig. 7-5: Two phase voltages, V_2 (yellow curve) and V_3 (pink curve), and the motor shaft-to-frame voltage V_{MSF} (sky-blue curve) measured at the grey motor. In addition to the voltage steps at V_{MSF} caused by the transients of the phase voltages, an EDM-event (marked with a yellow arrow) was observed.
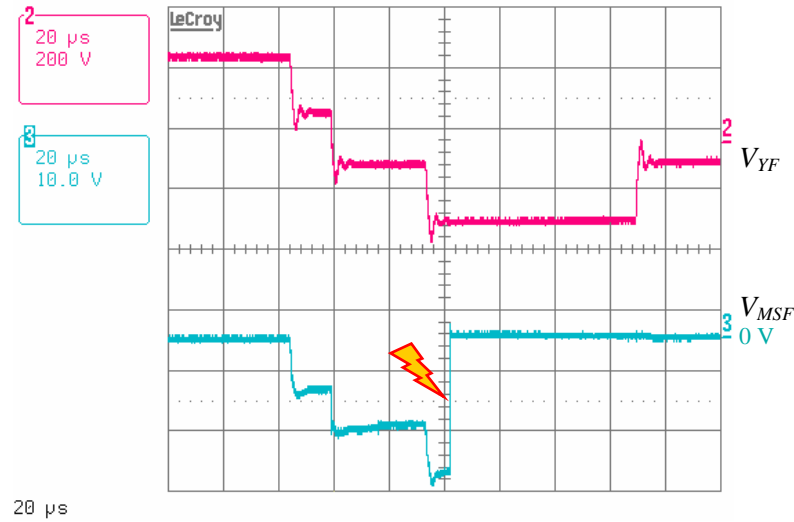
Fig. 7-6: Star point-to-frame voltage V_{YF} (pink curve) and motor shaft-to-frame voltage V_{MSF} (sky-blue curve) measured at the grey motor after equalising the voltage steps at V_{MSF} caused by the transients of the phase voltages. In addition to these steps, an EDM-event (marked with a yellow arrow) was observed.

Finally, the inverted voltage supplied by the transformer was connected to the air capacitor C_A via the tunable capacitor C_{AY}, and further, the compensation signal applied to the motor shaft was adjusted by means of C_{AY}. In this way, the motor shaft-to-frame

voltage could be compensated almost entirely (Fig. 7-7). The remaining voltage at the motor shaft was less than 1 V (except for short spikes at the transients of V_{YF}). Thus, a considerable reduction of V_{MSF} was achieved in contrast to normal operation of the motor (Fig. 7-3). By means of a more compact design in order to reduce stray capacitances and inductances of the circuit, the effectiveness of this compensation set-up could be further enhanced. In such a drive system, full compensation of the motor shaft-to-frame voltage is not achievable without equalising the voltage steps at V_{MSF}, because under these conditions V_{MSF} can be compensated only during certain periods (Fig. 7-8).
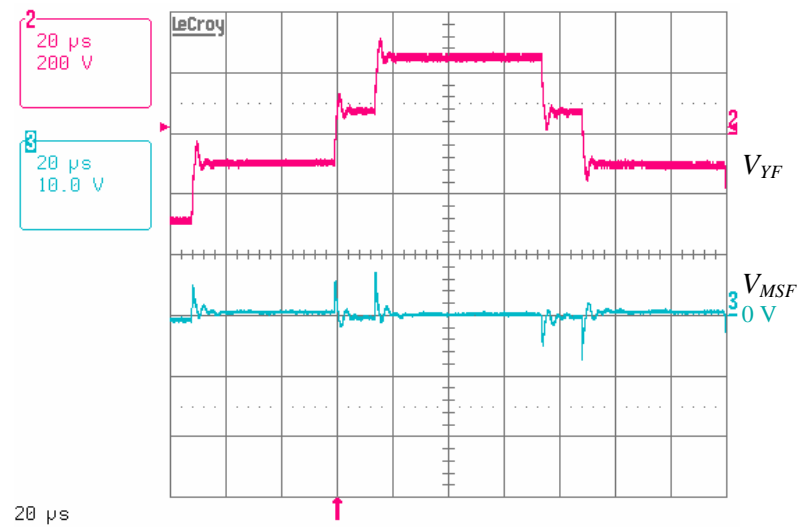
Fig. 7-7: Star point-to-frame voltage V_{YF} (pink curve) and motor shaft-to-frame voltage V_{MSF} (sky-blue curve) measured at the grey motor after equalising the voltage steps at V_{MSF} and adjusting the compensation signal.
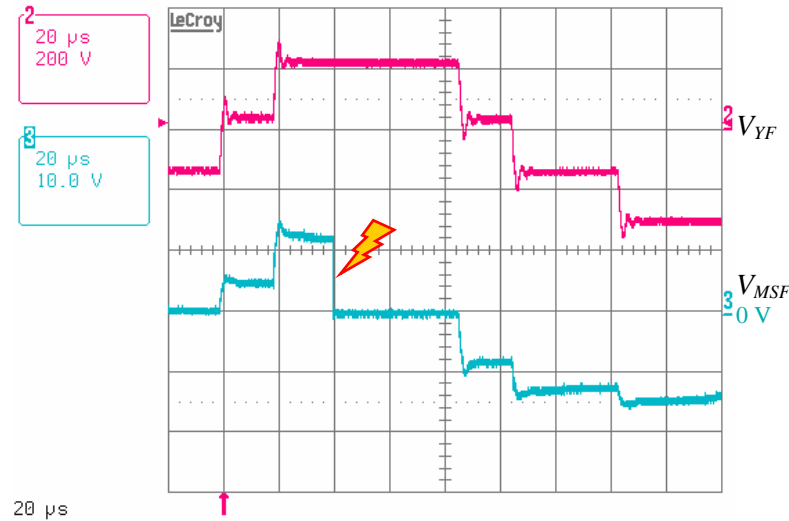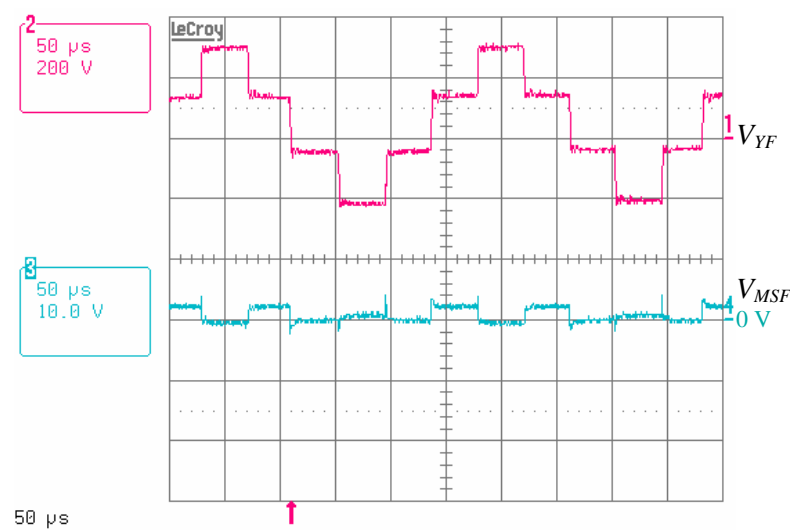

Fig. 7-8: Star point-to-frame voltage V_{YF} (pink curve) and motor shaft-to-frame voltage V_{MSF} (sky-blue curve) measured at the grey motor after applying a compensation signal but without equalising the voltage steps at V_{MSF}.

The capacitance values of C_{U1} (29 pF), C_{U3} (23 pF) and C_A (300 pF) were measured with a usual handhold LCR-meter. The total capacitance added in the compensation circuit between the stator winding W_1 or W_3 and the rotor is composed of the air capacitor C_A in series with the corresponding capacitor C_{U1} and C_{U3}, respectively, and yields approximately 26 pF and 21 pF. These values match well with the differences between the measured stray capacitances C_{SR1U}, C_{SR2U} and C_{SR3U} in the grey motor (Tab. 6-2, chapter 6.4.2):

$$C_{SR2U} - C_{SR1U} = 29 \text{ pF} - 2 \text{ pF} = 27 \text{ pF}$$
$$C_{SR2U} - C_{SR3U} = 29 \text{ pF} - 11 \text{ pF} = 18 \text{ pF}$$

The differences in the capacitive coupling between the stator windings and the rotor are mainly determined by the different capacitances C_{SR1U}, C_{SR2U} and C_{SR3U} (Fig. 7-1), which couple voltages to the motor shaft during voltage steps at the corresponding phase voltages. In contrast, the stray capacitances C_{SR1Y}, C_{SR2Y} and C_{SR3Y} (Fig. 6-19) are all effective between the motor star point and the motor shaft, therefore they are in parallel and couple, depending on the sum of their capacitances (equation (6.4)), a voltage to the motor shaft at each switching operation that occurs at any phase voltage. Hence, they contribute equal quantities to all voltage steps at V_{MSF}.

7.2   Earth-balanced motor drive

In common motor drives, the stator windings (W_1, W_2 and W_3) of a three-phase induction motor are each connected with one end to the corresponding output phase (U_1, U_2 or U_3) of the frequency converter and the other ends are interconnected to the motor star point. This common wiring for one stator winding is depicted in blue in Fig. 7-9. Because of the voltage steps that occur during the switching operations of the frequency converter and the stray capacitances between the stator and the rotor (C_{SR1U}, C_{SR1Y}, C_{SR2U}, C_{SR2Y}, C_{SR3U}, C_{SR3Y}) and the rotor and the frame (C_{RF}), the motor shaft-to-frame voltage is generated at the motor shaft. The concept of an earth-balanced motor drive as introduced here requires the frequency converter to supply each stator winding with two phase voltages being symmetric with respect to ground. For clarity, in the schematic diagram (Fig. 7-9) such wiring of an earth-balanced motor drive is illustrated only for the stator winding W_1. One end of the stator winding is connected to the phase voltage U_1 (depicted in green), in the same way as in common drives, but the other end is connected to the inverted phase voltage $-U_1$ (depicted in red).

Hence, under the assumption of equal stray capacitances ($C_{SR1U} = C_{SR1Y}$ and $C_{SF1U} = C_{SF1Y}$) between both ends of the stator winding W_1 and the rotor and motor frame, respectively, the voltage steps coupled from each end of the stator winding to the

rotor and the motor frame, respectively, compensate each other, because they have equal magnitudes but opposite polarities. That means that neither a motor shaft-to frame voltage nor a motor frame-to-ground voltage will be generated under these conditions, as the rotor is always at zero potential. If the rotor and the motor frame are at the same potential, no voltage exists across the bearings. But circulating currents caused by asymmetries of the magnetic field are still possible.
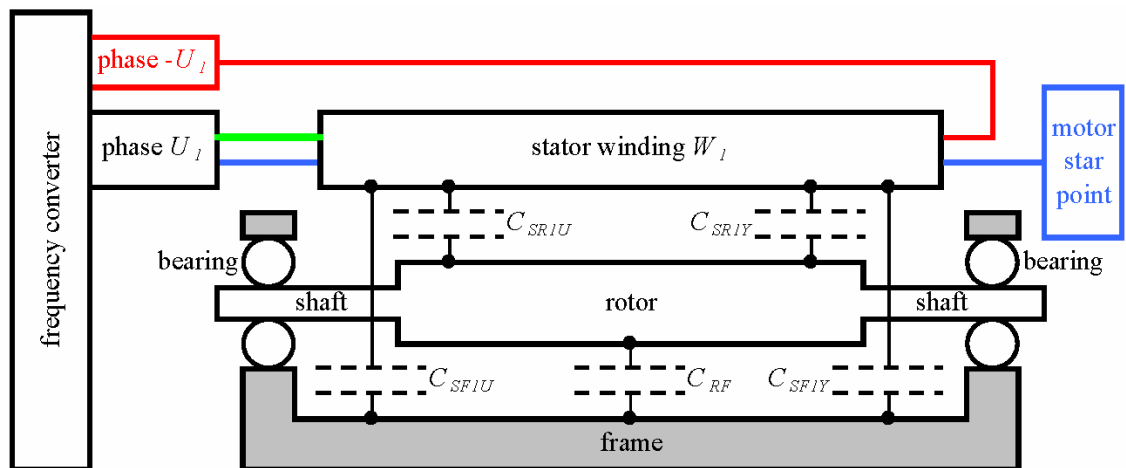
Fig. 7-9:   Schematic diagram for comparison of a common power supply by frequency converters and the earth-balanced motor drive. Only one stator winding is drawn in this diagram for clarity. The stray capacitances C_{SF1U} and C_{SF1Y}, and C_{SR1U} and C_{SR1Y} are effective between the ends of the stator winding W_1 and the motor frame and the rotor, respectively. The stray capacitance C_{RF} is effective between the rotor and the frame. The blue coloured lines symbolise the common wiring of a stator winding, whereby one end is connected to an output phase of the frequency converter and the other end to the motor star point. In the earth-balanced drive the stator winding is connected with one end to an output phase (green line) and with the other end to the corresponding inverted output phase (red line).

Nearly symmetrically distributed stray capacitances with respect to the ends of the corresponding stator windings were measured for the grey motor (Tab. 6-2, chapter 6.4.2).

By means of a special control circuit, each stator winding can be supplied with two phase voltages being symmetric with respect to ground. Representatively, the equivalent electric circuit of such an earth-balanced power supply is shown for one stator winding (W_1) in Fig. 7-10. The circuit is supplied by the voltages $V_{(+)}$ and $V_{(-)}$, which are provided by usual DC-links of frequency converters. By means of computer-controlled electronic power switches (S_1, S_2, S_3 and S_4) the voltages $V_{(+)}$ and $V_{(-)}$ each are switched to one end of the stator winding. If the switches S_1 and S_4 are closed and S_2 and S_3 are opened, the voltages $V_{(+)}$ and $V_{(-)}$ are connected to the ends E_1 and E_2 of the stator winding, respectively. Three states are allowed for this circuit, the before described state, the inverted state (S_1 and S_4 are opened and S_2 and S_3 are closed) and a third state

where all switches are opened. To ground the system during the third state and prevent the system from remaining charges, the stator winding is connected to ground via the resistors R (Fig. 7-10).
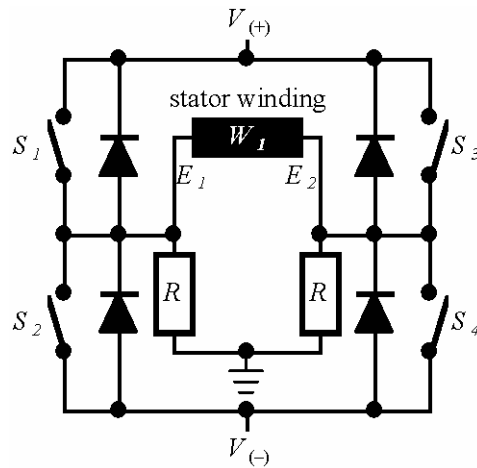
Fig. 7-10: Equivalent electric circuit of the earth-balanced power supply connected to the ends E_1 and E_2 of the stator winding W_1. The circuit is supplied by the voltages $V_{(+)}$ and $V_{(-)}$ provided by a usual DC-link of a frequency converter. The computer-controlled electronic power switches are symbolised by the switches S_1, S_2, S_3 and S_4. The system is grounded via the resistors R, if all switches are open.

Realisation of such an earth-balanced motor drive will require the cooperation between manufacturers of motors and electric drive systems (frequency converters).

8   Recommendations for analysis and optimisation of the electrical regime of frequency converter driven systems

Today, electrical current passage through bearings in frequency converter driven motors is in many cases the main reason for bearing damages (chapter 2.3). Therefore, various electrical drive systems, comprising a frequency converter, a three-phase induction motor and a driven machine, have been investigated and different counter measures against current passage through bearings have been developed (chapter 2.4). The effectiveness of these measures is often limited, and some particular action may reduce only specified types of bearing currents. Therefore, drive systems should be analysed before actions against bearing currents are implemented, because at worst case the installation of the wrong tool may even increase electric current passage through bearings. Hence, drive systems in combination with counter measures should be analysed again, to check the influence of the installed means on bearing currents. Manipulations at drive systems should be undertaken with care, in order not to cause damages on the frequency converter, the controlled motor or the driven machine.

8.1   System analysis

It should be emphasised, that not only the frequency converter, the electric motor and the driven machine, but also the cabling (including the grounding) is an essential component of a drive system. As described in chapter 3, circulating currents, high-frequency dv/dt-currents and EDM-currents under certain conditions may flow to ground via the bearings of the driven machine. Especially, sufficient high-frequency grounding (low inductance of the ground wiring) is necessary to avoid the build-up of the motor frame-to-ground voltage V_{FG} (chapter 3.6) due to high-frequency dv/dt-currents (chapter 3.5). The analysis of drive systems requires the knowledge of all available current paths. Therefore, it is necessary to study the cabling and grounding scheme of a given drive system as well as its mechanical configuration. Furthermore, the cabling of any sensors, such as tachometers, installed in a drive system for monitoring or control of system parameters, may provide additional paths for bearing currents. Moreover, it is important to know the types of the bearings (standard, coated or hybrid bearings) mounted in the motors and the driven machines, because coated bearings, in general, may break only circulating currents whereas hybrid bearings are able to avoid circulating currents, high-frequency dv/dt-currents and EDM-currents (chapters 2.4 and 3). However, hybrid bearings will not affect the motor shaft-to-frame voltage (V_{MSF}), which will still exist and may damage the bearings of the driven machine (Fig. 3-5), if neither the driven machine is also provided with hybrid bearings,

nor an insulating coupling is installed on the motor shaft. Under these conditions, i.e., hybrid bearings are mounted only in the electric motor, also high-frequency *dv/dt*-currents may flow along the motor shaft to the driven machine, through the bearings of the driven machine and via ground back to the frequency converter (Fig. 3-4), and, hence, may cause bearing damage.

8.2   Measurement of electrical parameters

The electrical regime of a frequency converter driven system is characterised by different electrical parameters, such as the inherent stray capacitances (chapter 3.1) in the driven motor and the star point-to-frame voltage V_{YF} (chapter 3.2) caused by the phase voltages and typical switching characteristics of the frequency converter. In combination, these parameters are responsible for the generation of the motor shaft-to-frame voltage V_{MSF} (chapter 2.3), if the motor shaft is electrically insulated from the motor frame, that is, the bearings are in the full-film lubrication regime and the motor shaft is not electrically contacted with the frame by any other means (e.g. brushes or slip rings). Consequently, EDM-processes may be initiated, as soon as the electric field strength reaches in any bearing the breakdown threshold of the lubricant, and, hence, bearing damages may be caused (chapter 3.7).

The star point-to-frame voltage and the motor shaft-to-frame voltage are available for measurement only at operating motors. It is evident that measurements at operating motors require special attention to avoid physical injuries of persons and damages of devices and measuring instruments. On the one hand, persons, instruments and probes must be protected from contact with the rotating motor shaft, and, on the other hand, it must be taken into account that high voltages (typically a few hundred volts) are present at motor phase terminals (V_1, V_2 and V_3) and the star point (V_{YF}), and under certain conditions (chapter 3.6) high voltage peaks may also appear at the frame with respect to ground (V_{FG}). Thus, it is necessary to use high-voltage probes for the measurement of V_1, V_2, V_3 and V_{YF} and measuring set-ups must be installed in a way to prevent electric shocks of persons and instruments. The motor shaft-to-frame voltage V_{MSF} is usually more than ten times smaller than V_{YF}, depending on the stray capacitances (C_{SR}, C_{RF}) and the bearing capacitances (C_{B1} and C_{B2}) in the motor (equation (3.2)).

The occurrence of EDM-currents can be observed by simultaneously measuring the star point-to-frame voltage and the motor shaft-to-frame voltage at the motor, as described in chapter 5.5.1. A precondition for EDM-processes in bearings is the build-up of V_{MSF}, which requires the motor shaft to be electrically insulated from the motor frame.

Representative wave forms of this voltage are shown in Fig. 6-18 (chapter 6.5.1) and typical breakdowns of V_{MSF} during EDM-events are presented in Fig. 6-20 (chapter 6.5.2). High-frequency dv/dt-currents appear only during the switching operations of the frequency converter, i.e., they flow during a voltage step at V_{YF}. During each voltage step at V_{MSF}, occurring simultaneously with a voltage step at V_{YF}, high-frequency dv/dt-currents cause charging or discharging of the capacitances C_{RF}, C_{B1} and C_{B2}. In contrast, EDM-processes do *not* necessarily coincide with the switching operations of the frequency converter. They may occur at any instant, when the electric field strength in one bearing of the motor reaches the breakdown threshold of the lubricant (chapter 3.7).

A good approximation of a bearing current, caused by an EDM-process, is achieved by the multiplication of the stray capacitance C_{RF} with the corresponding slew rate of the motor shaft-to-frame voltage (dV_{MSF}/dt) during the EDM-event, according to equation (6.10). This method requires the preceding measurement of C_{RF} (chapter 5.4.1). A more sophisticated method to measure the EDM-current (I_{EDM}) is described in chapter 5.5.4. This method requires the stray capacitance C_{RF} and the loop resistance R_{LE} of the EDM-loop in the motor to be measured in advance (chapters 5.4.1 and 5.5.3) and allows to determine the time dependence of currents (I_{EDM}) during EDM-processes. Hence, with additional knowledge of the time dependence of the motor shaft-to-frame voltage one can calculate the power P_{EDM}^* and the energy E_{EDM}^* transferred to the contact area in the bearing during the studied EDM-event (chapter 6.5.4, equations (6.6) and (6.7)). Further, this energy E_{EDM}^* transferred to the bearing can be compared with the total electric energy E_{EDM} (equation (6.8)) stored in the stray capacitance C_{RF} just before the onset of the investigated EDM-process.

The measuring set-up described in chapter 5.5.5 offers the possibility to study the effects of different grounding conditions on currents in the PE-wire and the shield of power cables, and on the build-up of the motor frame-to-ground voltage V_{FG} (chapter 6.5.5), which is caused by high-frequency dv/dt-currents and the inductance of the ground wiring. To obtain correct measurement results, the motor must be installed insulated from ground, the frames of the motor and the frequency converter may be connected only via the PE-wire and the shield, and the oscilloscope should be grounded only via the earth connection of the frequency converter.

The capacitive coupling between the stator windings and the rotor depends on the physical arrangement of the windings in the motor. The corresponding stray capacitances for each winding may differ from each other, as shown by the results listed

in Tab. 6-2 and Tab. 6-3 (chapter 6.4.2). The actual values of these stray capacitances, which must be known, e.g., for the adjustment of the set-up for the compensation of the motor shaft-to-frame voltage (chapter 7.1), can be determined by the measuring technique described in chapter 5.4.2.

8.3   System optimisation

The installation of protective earth (PE) wires at electric machines is obligatory. To avoid high-frequency dv/dt-currents and EMI (electromagnetic interference) in drive systems controlled by frequency converters, additional demands are raised to the cabling and grounding [2, 8, 9, 12, 17, 21]. It is recommended to use shielded power cables containing the wires for the phase voltages as well as the PE-wire. The cables should be as short as possible and their shields should offer sufficient high-frequency grounding (low inductance), so that high-frequency dv/dt-currents flow back to the frequency converter mainly along the shields (branch d in Fig. 3-4) and the currents flowing through bearings of the electric motor or the driven machine (branches $b1$, $b3$ and f) are reduced. Further, except for the PE-wire and the shield, there should not be any other electrical connection between a frequency converter, a controlled motor and a driven machine, which may offer an additional path to high-frequency dv/dt-currents. By means of hybrid (ceramic rolling element) bearings, high-frequency dv/dt-currents can be broken, if such bearings are installed not only in the motor but also in the driven machine, or if an insulated coupling on the motor shaft electrically disconnects the driven machine from the motor.

Circulating currents (flowing along the motor shaft, across one bearing to the motor frame and across the other bearing from the frame back to the shaft) can be broken by means of a coated or hybrid bearing installed at the non-drive end of the motor [2, 12, 13, 16, 18, 19]. However, the reduction or elimination of EDM-currents is more difficult. The equipment of a motor with hybrid bearings avoids EDM-currents in the motor, but the motor shaft-to-frame voltage is still existing and may cause bearing damage in the driven machine (Fig. 3-5). Therefore, the driven machine either must be equipped with hybrid bearings too, or an insulating coupling must be installed on the motor shaft, to protect the bearings.

Bearing damage caused by EDM-processes can be reduced considerably by the reduction of the motor shaft-to-frame voltage, which is the reason for EDM-events. The energy E_{EDM}^{*} (chapter 6.5.4, equation (6.7)) transferred to the contact area in a bearing during an EDM-event can never exceed the total electric energy E_{EDM} (equation (6.8))

stored in the capacitance C_{RF} before the initiation of the EDM-process. The magnitude of the maximal available EDM-energy is proportional to the square of the instantaneous value of the motor shaft-to-frame voltage (equation (6.8)). Thus, a reduction of V_{MSF}, as reached by the novel compensation set-up described in chapter 7.1, results in a great decrease of the total energy E_{EDM} stored in C_{RF}, and hence, of the energy fraction E_{EDM}^{*} transferred to the bearing during EDM-events. Therefore, it is assumed that bearing damages will also be reduced noticeably, if such compensation setup is installed.

9   Summary

Bearing damages due to electric current passage, such as circulating currents and electrostatic discharges, through rolling bearings in induction motors and driven machines are known for a long time. But the use of frequency converters for the control of the rotational speed has additionally given rise to bearing failures. Depending on the electrical set-up of a system comprising a frequency converter and a driven induction motor, additional effects, such as high-frequency *dv/dt*-currents, currents in the protective earth (PE) wire and electric discharge machining (EDM) may also be responsible for bearing damages. Electric current passage through rolling bearings happens in the contact areas between the rolling elements (e.g., bearing balls or cylindrical rolling elements) and the inner rings and outer rings, respectively, where it may damage the surfaces of the metallic components of the bearings as well as the lubricants. Although the study of these phenomena is of great interest, they have not always been distinguished clearly in the literature. An overview of parasitic currents, especially those generated in frequency converter driven motors and machines, and their sources according to recent literature and own research work is given in this work. To avoid machinery breakdown due to bearing failure, several counter measures against electric current passage through bearings have been developed, but most of them often allow to suppress, avoid or interrupt only a part of the existing processes, which may cause electric current passage through bearings. Therefore, the investigation of electric current passage through bearings and the effects causing these currents, especially those in frequency converter driven motors, were within the scope of these work.

In this work, special set-ups for measuring of stray capacitances, the motor shaft-to-frame voltage, bearing currents during EDM-processes, parasitic currents in the PE-wire and the motor frame-to-ground voltage at a test motor driven by a frequency converter were developed. By using these measurement results, the energy stored electrically in the corresponding stray capacitances just before the beginning of an EDM-event and the energy fraction transferred to the contact area in the bearings of the test motor during the EDM-process were calculated.

A static test rig was designed and constructed on the basis of obtained results. The static test rig was equipped with an EDM-circuit, which was designed to reproduce the EDM-loop of a typical three-phase induction motor. The test rig allows to initiate series of EDM-processes with defined energies at certain regions on the surfaces of test specimens (standard bearing balls and cylindrical rolling elements). The test rig allowed investigation of effects of different oils on EDM-processes and on damages generated at

the surfaces of the test specimens, and to study possible deterioration of the oils used in the test series. The voltage across the gap between the test specimens and the EDM-current were measured simultaneously during EDM-test series. Thus, the energy stored electrically in the capacitor of the test rig just before the onset of an EDM-event and the energy fraction transferred to a certain region between the test specimens during the EDM-process were calculated for test series carried out with the static test rig. To study the generated damages at the test specimens, the structures of certain regions on their surfaces affected by EDM-processes in the static rig were analysed with a contactless optical profile meter.

Further, the feasibility of applying infrared transmission spectroscopy for monitoring of deterioration of the reference oils due to EDM-processes initiated in the static test rig was checked. Although the stressed oils showed a distinct change in their colours, no significant differences in the infrared transmission spectra of fresh reference oils and of reference oils stressed by EDM-processes were observed. Moreover, physical properties, such as the relative permittivity, the kinematic viscosity and the mass density, of the oil samples were measured at selected temperatures, to investigate possible correlations between these properties and damages generated in the static test rig.

Using the results of preliminary measurements, damages generated at the surfaces of bearing balls were compared among each other with respect to their sizes, and then correlated to the kinematic viscosity, the mass density and the relative permittivity of the oil samples used in the test series. The greatest damages at the bearing balls were generated when oils with the highest mass densities were used, whereby no distinct influences of the kinematic viscosity and the relative permittivity were observed. To verify these tendencies, further test series and also a higher number of EDM-events should be carried out with the static test rig.

A monochrome high speed digital camera was used to photograph spark generation in the static test rig during EDM-events. The detected sparks did not appear at the smallest distance between test specimens, but were distributed within a certain region of the gap. This observation correlates with the detected local distribution of cavities and elevations on the surfaces of EDM-affected bearing balls, indicating that EDM-processes could be distributed also over the contact area in bearings under operating conditions.

Besides the development and employment of the special measuring set-ups for frequency converter driven motors and a static test rig for the investigation of damages

generated by EDM-processes, a prototype of the set-up for the compensation of the motor shaft-to-frame voltage, applied for a patent [39], was constructed and improved substantially. The function of the prototype as well as the increase of the effectiveness of the improved set-up was verified by measurements on the test motor equipped with this prototype. Preliminary investigations of bearing currents and their generation in frequency converter driven motors enabled the development of a novel counter measure preventing the generation of the motor shaft-to-frame voltage by means of an earth-balanced power supply of the motor (filed for a patent by AB SKF, Göteborg, Sweden).

Successful counter measures against current passages through bearings in drive systems require the knowledge of the electrical set-up and the mechanical configuration of drive systems. Using literature and results obtained during this work, recommendations for the analysis and the optimisation of the electrical set-up of frequency converter controlled drives were summarized.

10 Outlook

In order to calculate of the breakdown threshold of oil samples used in the static test rig the absolute distance of the test specimens and the voltage across this gap should be detected. However, this distance and, hence, the thickness of the material (air or oil) within the gap during test series can not be measured with the present set-up of the static test rig. Therefore, in future works, this test rig should be equipped with a system for measurements of the absolute distance between the test specimens.

Besides the static test rig, a dynamic test rig should be designed and constructed, which would enable test series with real rolling element bearings. To be able to create damages in test bearings using EDM-processes of defined energy, as performed with the static test rig at test specimens, in the dynamic test rig it should be possible to apply a voltage across the test bearing and to measure simultaneously this voltage and currents flowing through the bearing during test series. To avoid parasitic currents along the shaft and supporting bearings, the installed test bearing should be electrically insulated from the other components of the test rig.

In future studies, special test series should be carried out, to investigate the correlation between the size of damages generated by EDM-processes and the EDM-energy transferred to the damaged regions, because bearing damages in drive systems are assumed to depend mainly on the EDM-energy. Another task for future investigations should be to determine, if there was a threshold for the EDM-energy, below which bearing elements would not be damaged.

An EDM-process is initiated as soon as the field strength in the bearing reaches the breakdown threshold of the lubricant. The field strength depends on the voltage across the bearing and the thickness of the lubricant in the contact area. Therefore, EDM-processes would start at lower voltages and, hence, less energy, would be transferred to the contact area in the bearing, if the lubricant used in a bearing would have a lower breakdown threshold. Thus, a future aim for oil producers could be the creation of lubricants having lower breakdown voltage.

Engineering drawings of the static test rig

Grundplatte

SKF

Isolierplatte unten

SKF

BEDA

Plättchenhalter

SKF

BEDA

Steher 5

SKF

BEDA

Querbalken

6

SKF

BEDA

Schnitt A-A

Kantenbruch ca. 0.5 x 45°

1	Isolierplatte	8	-	System d	8
Stück	Benennung	Bezeichnung	Bemerkung	Material	

Edition / Year Month	1/	2/	3/	4/	5/	6/	7/	8/

Drawn	Checked	Approved			WU 23	Date	14-Jan-03

Isolierplatte
oben

Product Designation

8

CAD model no	Gewicht [kg]	Freimaßtoleranz	Maßstab
ISOLIERPLATTE_OBEN_8		DIN 7168-т	M=1:1

Product Code

SKF

Schnitt A-A

Kantenbruch ca. 0.5x45°

1	Zwischenplatte	-	-	C 35 o. ä.	9
Stück	Benennung	Bezeichnung	Bemerkung	Material	k.

Edition / Year Month	1/	2/	3/	4/	5/	6/	7/	8/

Drawn	Checked	Approved			WU 23	Date	13-Jan-03

SKF

Zwischenplatte

Product Designation

9

CAD model no	Gewicht [kg]	Freimaßtoleranz	Maßstab	Product Code
ZWISCHENPLATTE_9		DIN 7168-m	M=3:2	

Halterplatte

SKF

10

BEDA

Kugelhalter Oberteil

Kugelhalter Unterteil

SKF

12

List of instruments and devices

instrument / device	producer	owner
network analyser, HP8753	Hewlett Packard	TU Wien, ISAS (366)
viscosity meter, SVM 3000	Anton Paar GmbH	AC^{2}T
FTIR spectrometer	Bruker Optik GmbH	AC^{2}T
ATR accessory	SensIR Technologies	AC^{2}T
three-phase induction motor, ÖVE-M10/80, 7.5 kW, (green motor)	Elin	SKF Österreich AG, Development Centre Steyr
three-phase induction motor, DU160M2/TF/EV1S, 11 kW, (grey motor)	SEW-Eurodrive	SKF Österreich AG, Development Centre Steyr
LCR-meter, 9063	Voltcraft	Dr. Frank Buschbeck
high-frequency multi-channel digital storage oscilloscope, WavePro 940	LeCroy	SKF Österreich AG, Development Centre Steyr
frequency synthesiser, HP33120A	Hewlett Packard	TU Wien, IAP (134)
frequency converter, Movidrive MCV40A0110-5A3-4-00	SEW-Eurodrive	SKF Österreich AG, Development Centre Steyr
current probe, AP015, DC - 50 MHz	LeCroy	SKF Österreich AG, Development Centre Steyr
X-Y-translational stage	SKF Österreich AG	SKF Österreich AG, Development Centre Steyr
Z-stage, TB 80-25	Linos Photonics	SKF Österreich AG, Development Centre Steyr
piezo actuator, PV-10/80	Linos Photonics	AC^{2}T
control unit for the piezo actuator, Torque-Drive TD 1-200	Linos Photonics	AC^{2}T
pneumatic shock absorber system		TU Wien, IAP (134)
DC voltage source, DC-Konstanter 11	Siemens	TU Wien, IAP (134)
temperature sensor, PT 100	Crabtree	AC^{2}T
K-ring heating unit, KKR40018001A	Thermoprozess	AC^{2}T
temperature controller, PXZ4	Coulton Instrumentation LTD	AC^{2}T

instrument / device	producer	owner
contactless optical profile meter, µScan	NanoFocus	AC^2T
monochrome high speed digital camera, i-speed camera	Olympus	AC^2T
broadband inverting transformer	Nejdl & Pold Mechatronic OEG	SKF Österreich AG, Development Centre Steyr

Nomenclature

a .... branch of the *dv/dt*-current loop in a drive system

A .... connection between the electronic and the mechanical part of the static test rig

ATR .... attenuated total reflection

b, b1, b2, b3 .... branches of the *dv/dt*-current loop in a drive system

B .... connection between the electronic and the mechanical part of the static test rig

BB .... bearing ball

BVR .... bearing voltage ratio

c .... velocity of light

CRE .... cylindrical rolling element

C_A .... cylindrical air capacitor at the motor shaft

C_{AY} .... tuneable capacitor in the compensation setup for the adjustment of the compensation voltage

C_{B1}, C_{B2} .... bearing capacitances (between outer and inner ring) in the full-film lubrication regime

C_C .... capacitance of the coaxial hollow cylinders filled with air

C_D .... damping capacitance

C_E .... capacitance of the equivalent electric circuit for the EDM-loop

C_M .... capacitance of the measuring circuit

C_P .... parasitic capacitance of the measuring system for the permittivity

C_{REF} .... reference capacitance

C_{RF} .... total stray capacitance between the rotor and the frame of an induction motor

C_S .... capacitance of the EDM-circuit in the static test rig

C_{SF} .... total stray capacitance between the stator windings and the frame of an induction motor

C_{SR} .... total stray capacitance between the stator windings and the rotor of an induction motor

C_{SRE} .... stray capacitance between one end of a stator winding or one stator winding and the rotor

C_{SRF} .... sum of all stray capacitances between the rotor and that ends of stator windings, which were connected to the motor frame

C_{SR1}, C_{SR2}, C_{SR3} .... stray capacitance between the rotor and the stator winding W_1, W_2 and W_3, respectively

C_{SR1U}, C_{SR2U}, C_{SR3U}.... stray capacitance between that end of the stator winding (W_1, W_2 and W_3), which is connected to the corresponding phase (U_1, U_2 and U_3) of a frequency converter, and the rotor of an induction motor

C_{SR1Y}, C_{SR2Y}, C_{SR3Y} ..... stray capacitance between that end of the stator winding (W_1, W_2 and W_3), which is connected to the motor star point, and the rotor of an induction motor

C_{U1}, C_{U2}, C_{U3} .... tuneable capacitors in the compensation setup for the equalisation of the coupling between the stator windings (W_1, W_2 and W_3) and the rotor in the motor

d .... branch of the dv/dt-current loop in a drive system

dv/dt .... change of voltage in relation to time

DE .... drive-end (bearing)

ΔV_{MSF} .... voltage steps at V_{MSF}

ΔV_{YF} .... voltage steps at V_{YF}

e .... branch of the dv/dt-current loop in a drive system

E .... earth connection of the oscilloscope

EDM.......................... electric discharge machining

EMI .... electromagnetic interference

E_{CS} .... electric energy stored in the capacitor C_S

E_{EDM} .... electric energy stored in the capacitances C_{RF} and C_B (EDM-energy)

E_{EDM}^{*} .... electric energy transferred to the bearing during an EDM-process (EDM-energy)

E_G .... electric energy transferred to the gap between test specimens in the EDM static test rig

E_1, E_2 .... both ends of a stator winding

ε_r .... relative permittivity

$\varepsilon_{r,A}$ .... relative permittivity of air ($\simeq 1$)

$\varepsilon_{r,CH}$ .... relative permittivity of cyclohexane

$\varepsilon_{r,OS}$ .... relative permittivity of an oil sample

η .... dynamic viscosity

f .... branch of the dv/dt-current loop in a drive system

f_{IR} .... frequency of the infrared wave

f_M .... measuring frequency

F .... fictive point in the EDM-loop of an induction motor

F^* .... available point in the measuring circuit, which corresponds to F

FTIR.......................... Fourier transformed infrared

F_R .... region at the frame, where different branches of the *dv/dt*-current loops reunite

g1, g2 .... branches of the EDM current loop in a drive system

G .... electrical ground, earth potential (ground)

G_{OS} .... conductance (real part of the admittance) of the coaxial hollow cylinders filled with an oil sample

IGBT .... Insulated Gate Bipolar Transistor

IRTS .... infrared transmission spectum/a

I_{dV} .... current caused due to voltage steps ΔV_{MSF} across C_{RF}

I_{EDM} .... current in the EDM-loop during an EDM-process (EDM-current)

I_{PE} .... current in the protective earth wire between the motor and the frequency converter

I_S .... current in the shield between the motor and the frequency converter

I_{SE} .... current between both ends of the motor shaft (shaft end-to-end current)

I_{SEDM} .... current in the EDM-circuit of the static test rig during an EDM-process

j .... imaginary unit

L_E .... inductance of the equivalent electric circuit for the EDM-loop

L_{LE} .... intrinsic inductance in the EDM-loop of induction motors

λ_{IR} .... wave length of the infrared wave

M .... mid-point of the DC-link of a frequency converter

MC .... mercury contact

MOV .... metal oxide varistor

NDE .... non-drive-end (bearing)

v .... kinematic viscosity

v_{40} .... kinematic viscosity at 40 °C

v_{80} .... kinematic viscosity at 80 °C

PE .... protective earth

PWM .... pulse width modulation

P_{EDM}^{*} .... electric power transferred to the bearing during an EDM-process

P_G .... electric power transferred to the gap between test specimens in the EDM static test rig

Q .... total charge in the measuring set-up for the determination of C_{RF}

R .... resistors in the earth-balanced power supply

R_C .... contact resistance

R_D .... damping resistance

R_E .... resistance of the equivalent electric circuit for the EDM-loop

R_I .... limiting resistance for the current from the DC voltage source to the EDM-circuit

R_{LE} .... loop resistance in the EDM-loop of induction motors

R_M .... resistance of the measuring circuit

R_S .... resistance of the EDM-circuit in the static test rig

ρ .... mass density

S_C .... switch for the simulation of electrical contact in a bearing

S_E .... switch in the equivalent electric circuit for the EDM-loop

S_1, S_2, S_3, S_4 .... switches in the earth-balanced power supply

σ_{IR} .... wave number of the infrared wave

t_A, t_B .... time after and before the closing of the reed relay contact

t_0 .... time just before the onset of an EDM-process

τ .... time constant

τ_C .... time constant for the charging of C_S

τ_D .... time constant for the discharging of C_S

τ_S .... smallest time constant of EDM-processes in a motor

U .... index denoting that end of the stator winding, which is connected to the power supply

U_1, U_2, U_3 .... frequency converter output phases

$V_{(+)}$ .... voltage between the positive voltage rail and ground

$V_{(-)}$ .... voltage between the negative voltage rail and ground

V_{BD} .... breakdown voltage of a lubricant film in a bearing

V_{CREF} .... voltage across the capacitor C_{REF}

V_E .... voltage across the capacitor C_E in the equivalent electric circuit

V_{F*} .... voltage picked up at the point $F*$ (across R_M)

V_{FG} .... voltage between the motor frame and the ground (motor frame-to-ground voltage)

V_{MSF} .... voltage between the motor shaft and the motor frame, and hence, also across the bearings (motor shaft-to-frame voltage)

V_{RF} .... voltage across the stray capacitance C_{RF}

V_{RS} .... voltage across the resistor R_S in the static test rig

V_{SE} .... voltage between both ends of the motor shaft (shaft end-to-end voltage)

V_{SW} .... square wave signal applied by the frequency synthesiser between one (both) end(s) of a stator winding and the motor frame

V_{TS} .... voltage across the gap between test specimens in the static test rig

V_{YF} .... voltage between the motor star point and the motor frame (star point-to-frame voltage)

$V_{Y'F}$ .... voltage generated with a special broadband transformer by inverting the star point-to frame voltage (inverted voltage)

V_{YG} .... voltage between the motor star point and ground (star point-to-ground voltage)

V_1, V_2, V_3 .... voltage between the frequency converter output phases U_1, U_2 and U_3, respectively, referred to ground (phase voltages)

W_1, W_2, W_3 .... windings of the stator each connected with one end to the phases U_1, U_2 and U_3, respectively, of the frequency converter

ω .... angular frequency ($\omega = 2\pi f_M$)

ω_E .... angular frequency used for the simulation of an EDM-event

X (= 1,2 or 3) .... variable indicating the phase voltage (U_1, U_2 or U_3), which is switched over by the frequency converter

Y .... star point of a wye connected three-phase induction motor

Y .... index denoting that end of the stator winding, which is connected to the motor star point

Y_A .... admittance of the coaxial hollow cylinders filled with air

Y_{CH} .... admittance of the coaxial hollow cylinders filled with cyclohexane (C_6H_{12})

Y_{OS} .... admittance of the coaxial hollow cylinders filled with an oil sample

References

[1]   P. F. Brosch, *Moderne Stromrichterantriebe,* 4. überarbeitet Auflage, Kamprath-Reihe, Vogel Buchverlag, Würzburg 2002, ISBN 3-8023-1887-0

[2]   G. Preisinger, *Cause and effect of bearing currents in frequency converter driven electrical motors – investigations of electrical properties of rolling bearings*, Dissertation, TU Wien, 2002

[3]   A. Kempski, *Capacitively coupled discharging currents in bearings of induction motor fed from PWM (pulsewidth modulation) inverters*, Journal of Electrostatics 51-52, p. 416-423, 2001

[4]   D. Hyypio, *Mitigation of Bearing Electro-erosion of Inverter-fed Motors through Passive Common Mode Voltage Suppression*, Proceedings of 38th Conference on Industry Applications, Vol. 2, p. 875-882, 2003

[5]   O. Schenk, *Stromdurchgang durch Wälzlager*, Der Maschinenschaden, Heft 11/12, S. 131-135, 1953

[6]   A. Kohaut, *Riffelbildung in Wälzlagern infolge elektrischer Korrosion*, Zeitschrift f. angewandte Physik, Band 1, Heft 5, S. 197-211, 1948

[7]   A. Mütze, *Bearing Currents in Inverter-Fed AC-Motors*, Dissertation, TU Darmstadt, Shaker Verlag, Aachen, 2004

[8]   R. F. Schiferl, M. J. Melfi, *Bearing current remediation options*, IEEE Industry applications magazine, Vol. 10, No. 4, p. 40-50, July-August 2004

[9]   D. Macdonald, W. Gray, *A practical guide to understanding bearing damage related to PWM drives*, Conf. Record of IEEE Pulp and Paper Industry Technical Conf., p. 159-165, 21-26 June 1998

[10]   IEEE Power Engineering Society, *IEEE Standard Test Procedure for Polyphase Induction Motors and Generators*, IEEE Std 112[TM]-2004

[11]   D. Busse,   J. Erdman,   R. J. Kerkman,   D. Schlegel,   G. Skibinski,   *Bearing Currents and Their Relationship to PWM Drives*, IEEE Transactions on Power Electronics, Vol. 12, No. 2, p. 243- 252, 1997

[12]   International Electrotechnical Commission, *Technical Specification, Rotating electrical machines – Part 25: Guide for the design and performance of cage induction motors specifically designed for converter supply*, IEC/TS 60034-25, 2004

[13]   S. Bell, T. J. Cookson, S. A. Cope, R. A. Epperly, A. Fischer, D. W. Schlegel, G. L. Skibinski, *Experience With Variable-Frequency Drives and Motor Bearing Reliability*, IEEE Transactions on Industry Applications, Vol. 37, No. 5, p. 1438-1446, 2001

[14]   V. Hausberg, H. O. Seinsch, *Kapazitive Lagerspannungen und –ströme bei umrichtergespeisten Induktionsmaschinen*, Electrical Engineering 82, S. 153-162, 2000

[15]   V. Hausberg, H. O. Seinsch, *Wellenspannungen und zirkulierende Lagerströme bei umrichtergespeisten Induktionsmaschinen*, Electrical Engineering 82, S. 313-326, 2000

[16]   D. Busse, J. Erdman, R. J. Kerkman, D. Schlegel, G. Skibinski, *An Evaluation of the Electrostatic Shielded Motor: A Solution for Rotor Shaft Voltage Buildup and Bearing Current*, IEEE Industry Application Society, Conference Record, Vol. 1, p. 610-617, 1996

[17]   P. J. Link, *Minimizing Electric Bearing Currents in Adjustable Speed Drive Systems*, IEEE Record of Pulp and Paper Industry Technical Conference, p. 181-195, 1998

[18]   V. Hausberg,   H. O. Seinsch,   *Schutzmaßnahmen   gegen   Lagerschäden umrichtergespeister Motoren*, Electrical Engineering 82, p. 339-345, 2000

[19]   A. von Jouanne, H. Zhang, A. K. Wallace, *An Evaluation of Mitigation Techniques for Bearing Currents, EMI and Overvoltages in ASD Applications*, IEEE Transactions on Industry Applications, Vol. 34, No. 5, p. 1113-1122, 1998

[20]   K. B. Klaassen, J. C. L. van Peppen, *Charge Generation and Bleed-Off in Spindle Motors With Ceramic Ball Bearings*, IEEE Transactions on Magnetics, Vol. 39, No 5, p. 2435-2437, 2003

[21]   E. J. Bulington, S. Abney, G. L. Skibinski, *Cable Alternatives for PWM AC Drive Applications*, Industry Application Society, 46th Petroleum and Chemical Industry Conference. p. 247-259, 1999

[22]   M. M. Swamy, K. Yamada, T. J. Kume, *Common Mode Current Attenuation Techniques for Use with PWM Drives*, IEEE Transactions on Power Electronics, Vol. 16, No. 2, p. 248-255, 2001

[23]   S. Ogasawara, H. Ayano, H. Akagi, *An Active Circuit for Cancellation of Common-Mode Voltage Generation by a PWM Inverter*, IEEE Transactions on Power Electronics, Vol. 13, No. 5, p. 835-841, 1998

[24]   A. L. Julian, G. Oriti, T. A. Lipo, *Elimination of Common-Mode Voltage in Three-Phase Sinusoidal Power Converter*, IEEE Transactions on Power Electronics, Vol. 14, No. 5, p. 982- 989, 1999

[25]   A. von Jouanne, H. Zhang, *A Dual-Bridge Inverter Approach to Eliminating Common-Mode Voltages and Bearing and Leakage Currents*, IEEE Transactions on Power Electronics, Vol. 14, No. 1, p. 43-48, 1999

[26]   H. Zhang, A. von Jouanne, S. Dai, *A Reduced Dual-Bridge Inverter Topology for the Mitigation of Bearing Currents, EMI, and DC-Link Voltage Variations*, IEEE Transactions on Industry Applications, Vol. 37, No. 5, p. 1365-1372, 2001

[27]   R. A. Guyer Jr., *Rolling Bearings Handbook and Troubleshooting Guide*, Chilton Book Company, Radnor, Pennsylvania, 1996, ISBN 0-8019-8871-3

[28]   A. Jagenbrein, F. Buschbeck, M. Gröschl, G. Preisinger, *Investigations of the Physical Mechanisms in Rolling Bearings During Electrical Current Passage*, 14th Int. Colloquium Tribology – Tribology and Lubrication Engineering, 13.-15. Jan., Hrsg. W. J. Barts, Technische Akademie Esslingen, Ostfildern, Vol. 2, p. 995-997, 2004, ISBN 3-924813-54-X

[29] A. Jagenbrein, F. Buschbeck, M. Gröschl, G. Preisinger, *Untersuchung elektrisch bedingter Schädigungsmechanismen von Wälzlagern*, Innovationen der SKF Österreich AG aus wissenschaftlichen Kooperationen mit Universitäten und Fachhochschulen, Development Centre Steyr, SKF Science Days, 18.-19. Mai, p. 91-95, 2004

[30] A. Jagenbrein, F. Buschbeck, M. Gröschl, G. Preisinger, *Investigations of the Physical Mechanisms in Rolling Bearings During Electrical Current Passage*, Tribotest 11-4, *in print*, Leaf Coppin, 2005

[31] H. W. Hayt, *Engineering Electromagnetics*, 5th ed. New York, McGraw-Hill, 1989

[32] H. Prashad, *Theoretical evaluation of capacitance, capacitive reactance, resistance and their effects on performance of hydrodynamic journal bearings*, Transactions ASME, Vol. 113, p. 762-767, 1991

[33] J. L. Melsa, D. G. Schultz, *Linear Control Systems*, New York, McGraw-Hill, 1989

[34] J. Erdman, R. J. Kerkman, D. Schlegel, G. Skibinski, *Effect of PWM Inverters on AC Motor Bearing Currents and Shaft Voltages*, IEEE Transactions on Industry Applications, Vol. 32, No. 2, p. 250-259, 1996

[35] SKF General Catalogue 5000

[36] *CRC Handbook of Chemistry and Physics*, Editor: D. R. Lide, 76th Edition, CRC Press, Boca Raton, New York, London, Tokyo, 1995-1996

[37] A. Agoston, C. Ötsch, F. Novotny-Farkas, H. Eisenschmid, B. Jakoby, *Sensors for a Lubrication-Monitoring-System*, 14th Int. Colloquium Tribology – Tribology and Lubrication Engineering, 13.-15. Jan., Hrsg. W. J. Barts, Technische Akademie Esslingen, Ostfildern, Vol. 3, p. 1883-1889, 2004, ISBN 3-924813-54-X

[38] Gerätebeschreibung, *SVM 3000, Stabinger Viskosimeter*, Anton Paar GmbH, 8054 Graz, Austria

[39]   ASTM D7042 "*Standard Test Method for Dynamic Viscosity and Density of Liquids by Stabinger Viscometer (and the Calculation of Kinematic Viscosity)*" ASTM International, For referenced ASTM standards, visit the ASTM website, www.astm.org, or contact ASTM Customer Service at service@astm.org. For Annual Book of ASTM Standards volume information, refer to the standard's Document Summary page on the ASTM website.

[40]   EP 1 445 850 A1, *Vorrichtung zum Schutz eines Lagers einer Elektromaschine vor einem schädigenden Stromdurchgang*, Anmelder: AB SKF, Göteborg, Sweden, Erfinder: F. Buschbeck, M. Gröschl, G. Preisinger

Danksagung

Lebenslauf

Persönliche Daten

Name: Andreas Jagenbrein

geboren am: 10. 03. 1970 in Wien

Familienstand: ledig

wohnhaft in: 2443 Leithaprodersdorf, Unt. Hauptstr. 2

Schulausbildung

09/1976 – 06/1980	Volksschule in Leithaprodersdorf
09/1980 – 05/1988	Aufbaugymnasium in Unterwaltersdorf
31.05.1988	Matura

Bundesheer

10/1988 – 09/1989

Studium

10/1989 – 01/2002	Technische Physik an der TU Wien
	Schwerpunkt: Methoden und Technologie
	Diplomarbeitsthema: „Magnetische Untersuchung an einkristallinem $Tb_{41,5}Y_{58,5}$ und Dy_3Co"
16.01.2002	Diplomprüfung

Studienbegleitende Tätigkeiten

1992 – 1997	Ferialpraxis im Österreichischen Forschungszentrum Seibersdorf
03/2001 – 06/2001	Studienassistent an der TU Wien, Institut für angewandte Physik

seit 03/2002 Doktoratstudium an der TU Wien

04/2002 – 12/2002	wissenschaftlicher Mitarbeiter am Institut für allgemeine Physik der TU Wien im Rahmen des Dissertationsprojekts: „Untersuchung elektrisch bedingter Schädigungsmechanismen in Wälzlagern"
01/2003 – 06/2005	Junior researcher bei der AC^2T research GmbH in Wr. Neustadt im Rahmen des Dissertationsprojekts: „Investigation of the mechanisms causing bearing damage due to electric current passage"